國立臺灣大學工學院材料科學與工程學研究所

碩士論文

Department of Materials Science and Engineering
College of Engineering
National Taiwan University

Master Thesis

以二次離子質譜縱深分析研究藥物分子於有機金屬框架內的擴散行為

Diffusion of Drug Molecules in Metal-Organic Framework: Direct Probing by Secondary Ion Mass Spectroscopy Depth Profiling

謝博鈞
Pochun Hsieh

指導教授：薛景中 博士
Advisor: Jing-Jong Shyue, Ph.D.

中華民國 112 年 7 月
July, 2023

doi:10.6342/NTU202303887

誌謝

兩年半的研究生生活即將畫下尾聲，在這段時間中遇到了太多我生命中的貴人，如聖經中羅馬書八章二十八節：『萬事都互相效力，叫愛神的人得益處。』我是受到了這麼多的愛以及照顧，才能完成這篇論文。

首先要感謝我的指導教授—薛景中教授。薛老師是我求學中遇過最博學、最熱心、辛勤又完全沒有架子的老師。感謝老師兩年半間傳授的知識以及在研究上的支援，每次我闖禍了老師都是二話不說幫我收拾殘局。過年還在實驗室維修 C_{60} 的薛老師永遠是我心中的英雄。

再來我要感謝兩位口試委員 賴育英教授以及 林煒淳教授的指導。感謝兩位老師細心審閱我的論文並提出諸多寶貴意見，使我的論文更臻完備，在此致上無盡的感謝。

感謝實驗室夥伴的支持與包容：感謝一直陪在我們身邊、幫助我們處理大小事務的 Myra；感謝巴比帶我操作 SIMS，與我討論實驗並且提供給我轉換到 ZIF-8 材料的重要建議；感謝玟儀是我這兩年半最好的夥伴，不論修課與實驗都在與妳的討論中大有獲益；感謝芃萱學姊在研究上前置性的探討；感謝林煒淳老師實驗室的夥伴：俊賢、翊愷、伯芝、珮禎，在數據量測的協助。

感謝我的家人對我經濟以及精神的支持：感謝我的阿嬤每天為我準備便當、為我打掃洗衣，是我生活最大的支柱；感謝我的媽咪，每次我回新竹都煮超級豐盛的東西給我吃，陪我聊天給我建議；感謝我的爸爸每每陪我吃飯，跟我聊天時總是提供我不同的眼界；感謝我的姑姑們、我的表哥表弟，一直陪在我身邊，也都是我最重要的家人。

感謝這段期間我喜歡過的所有偶像，礙於篇幅僅列出部分：木苺 Fructose 的甘崎紗音、存在証明的雪薇 Yukibi、Primulav 的 KANA-KANA 等。妳們是我生活的動力、快樂的來源，不論我遇到什麼樣的困難與挫折，只要想到妳們我就能重拾笑容。也感謝這段期間陪伴我的朋友，特別是なつき、友勳、毛球，這段時間受了你們特別多的照顧。

最重要的，感謝天主一直以來對我的看顧以及陪伴，保守我免於兇惡、身心平安，在生活及研究上賜下一切的幫助。雖然我的論文稱不上什麼偉大成就，但我樂在研究及撰寫的過程，也得到很大的成長。這篇論文確實是我這兩年半細心呵護長大的寶貝，我為它感到驕傲，也希望可以藉此獻給所有幫助我完成這篇論文的人。

doi:10.6342/NTU202303887

摘要

金屬有機框架（MOFs）因其高比表面積、可調孔徑和官能基團等獨特性質，其作為各種應用的材料已被廣泛的討論。然而，MOFs 開發中的一個挑戰是瞭解客體分子在其中的擴散。不幸的是，至今只有極少數的研究能夠直接瞭解客體分子在 MOFs 中的分佈情況，這對 MOFs 的開發和應用造成了重大障礙。然而，二次離子質譜(SIMS)由於其卓越的空間解析度，分別為小於 100 奈米的橫向解析度、及小至數奈米的深度解析度，以及其達到百萬分之一（ppm）的靈敏度，都顯示其成為研究 MOFs 中客體分子分佈的分析技術的潛力。

然而，儘管 SIMS 可以提供關於樣品組成和分佈的資訊，但是過往的研究指出，在縱深分析過程中的高能離子轟擊會對 MOF 的化學結構造成損害，尤其是會使有機訊號強度大幅下降。因此，為了瞭解客體分子在 MOF 中的擴散，不僅需要選擇適當的 MOF 和客體分子，還需要優化濺射條件以建構 MOF 的縱深分析。

在實驗之初，首先使用不同方法合成了多種不同形貌的 MOF，並在其中挑選適當的材料來進行後續客體分子分布之分析。其中，透過 Cathodic deposition 製備的 Zeolitic imidazolate framework (ZIF-8) 薄膜展現出均勻且緊密的結構，且容易進行縱深分析，因此被挑選為其中最理想的探究對象。另一方面，由於其他 MOF 在建構縱深分析方面存在困難，或其在縱深分析中未顯示出客體分子的擴散行為，因此不適合作為本實驗的分析平台。

在 SIMS 分析中，所有樣品都使用脈衝 C_{60}^+ 作為分析離子源，而濺射離子源則選用三種離子束，分別為 Ar^+、C_{60}^+ 和氬氣簇離子團 (Ar-GCIB)，並分析其建構的縱深分析，以從中挑選出最佳的濺射離子源。在這之中，Ar-GCIB 展現其作為最佳濺射離子源的優異性能：它提供了高有機訊號強度和高濺射率。這歸因於 Ar-GCIB 的能量密度相對較低，對樣品的破壞較小而保留了有機訊號強度；而簇離

doi:10.6342/NTU202303887

子團對聚合材料的非線性增強促進了其高剝蝕速率。

確定了合適的材料和最佳的分析條件後，常用鎮痛藥物乙醯氨酚和其輔劑咖啡因被用作於顯示 MOF 中客體分子的擴散行為，這是因為藥物傳遞是關於 MOF 擴散中最受關注的應用之一。透過研究藥物擴散進入 ZIF-8 薄膜的縱深分析可以得知，客體分子在 ZIF-8 中的擴散不僅取決於客體分子的大小，還取決於用於溶解客體分子的溶劑：乙醯氨酚較小的尺寸（~4.3 Å）使其能夠進入 ZIF-8，而咖啡因（~6.0 Å）則不能；此外，溶解在乙醇的乙醯氨酚擴散進入 ZIF-8 的速度比溶解在二甲基甲醯胺中溶解的乙醯氨酚更高。

最後，利用相同的方法，我們也獲得了雙金屬 ZIF 的縱深分析，使我們能夠偵測雙金屬 MOF 中每種金屬的濃度分佈。此實驗顯示了 SIMS 分析對於 MOF 材料的潛力，這對於了解這些材料的結構和性質至關重要。總體而言，本研究凸顯了 SIMS 分析在研究 MOF 中客體分子擴散以及其他潛在應用的潛力。

關鍵字：金屬有機框架、Zeolitic imidazolate framework (ZIF-8)、飛行時間式二次離子質譜儀、縱深分析、擴散

doi:10.6342/NTU202303887

Abstract

Metal-Organic frameworks (MOFs) have become a popular material for various applications due to their unique properties, such as high specific surface area, adjustable pore size, and functional groups. However, one of the challenges in the development of MOFs is to understand the diffusion of guest molecules in MOFs. Unfortunately, there have been limited researches that are capable of directly obtaining the distribution of guest molecules in MOFs. This presents a significant obstacle to the development and application of MOFs. Nonetheless, secondary ion mass spectrometry (SIMS) has shown its potential to be a highly effective analytical technique for investigating the distribution of guest molecules in MOFs due to its exceptional spatial resolution, with lateral resolution of less than 100 nm and depth resolution of several nanometers, as well as its remarkable detection sensitivity of parts per million (ppm).

However, although SIMS can provide detailed and comprehensive information regarding the composition and distribution of samples, the bombardment of high-energy ions has been reported to introduce damages to MOFs during depth profiling, especially for organic signals. Therefore, in order to understand diffusion of guest molecules in MOFs, it requires not only careful selection of appropriate MOF and guest molecules, but also optimization of sputtering parameters for constructing depth profiles of MOFs.

First of all, several MOFs were synthesized using various methods to identify the appropriate material for analyzing the distribution of guest molecules within its structure. Among them, the zeolitic imidazolate framework (ZIF-8) thin film prepared via cathodic deposition was shown to be the most ideal one due to its uniform and well-

doi:10.6342/NTU202303887

intergrown structure, as well as its accessibility to depth profiling. On the other hand, other MOFs presented challenges in constructing depth profiles or failed to show diffusion behavior in their depth profiles.

For SIMS analysis, a pulsed C_{60}^+ beam was used as the acquisition beam for all samples, while three ion beams, namely Ar^+, C_{60}^+, and argon gas cluster ion beam (Ar-GCIB), were employed as the sputtering sources. Remarkably, the Ar-GCIB exhibited superior performance as the optimal sputtering source, as it provided both a high intensity of organic signal and a high sputtering rate. This is attributed to the fact that Ar-GCIB has relatively low energy density, resulting in less damage to the sample, while the nonlinear enhancement of sputter yield from cluster beam for polymeric materials contributes to its high sputtering rate.

Having established both the appropriate material and optimal analysis conditions, depth profiles of ZIF-8 loaded with guest molecules were obtained using the common analgesic drug acetaminophen and its adjuvant caffeine as the model drugs since drug delivery is one of the crucial fields concerning diffusion in MOFs. The findings revealed that the diffusion of guest molecules in ZIF-8 not only depends on the size of the guest molecules, but also on the solvent used to dissolve them. Specifically, the smaller size of acetaminophen (~4.3 Å) enabled its entry into ZIF-8, while caffeine (~6.0 Å) could not. Additionally, acetaminophen dissolved in ethanol exhibited a higher diffusivity compared to acetaminophen dissolved in dimethylformamide (DMF).

Finally, using the same protocol, depth profiles of bimetallic ZIFs were also obtained to demonstrate the potential of SIMS analysis for MOFs. These depth profiles enabled the determination of the concentration profile of each metal in the bimetallic ZIFs, which is crucial for understanding the structure and properties of these materials.

doi:10.6342/NTU202303887

Overall, this study highlights the capabilities of SIMS analysis for investigating the diffusion of guest molecules in MOFs as well as other possible potentials.

Keywords: metal-organic framework (MOF), Zeolitic imidazolate framework (ZIF), time of flight secondary ion mass spectrometry (ToF-SIMS), depth profile, diffusion

doi:10.6342/NTU202303887

Table of Contents

doi:10.6342/NTU202303887

doi:10.6342/NTU202303887

List of Figures

doi:10.6342/NTU202303887

doi:10.6342/NTU202303887

doi:10.6342/NTU202303887

doi:10.6342/NTU202303887

doi:10.6342/NTU202303887

doi:10.6342/NTU202303887

List of Tables

doi:10.6342/NTU202303887

Chapter 1 Introduction

Metal-organic frameworks (MOFs) have emerged as a promising class of materials due to their high porosity, large surface area, and tunable properties. They are composed of metal ions linked by organic ligands to form a porous network with well-defined pores. Numerous attempts have been done to synthesize MOFs with controlled morphologies and sizes and some of the prospective methods were reviewed including liquid phase epitaxy, cathodic deposition and vapor-assisted conversion. MOFs have a wide range of potential applications, including gas storage and separation, catalysis, drug delivery, and sensing.[1–3] Understanding the behavior of guest molecules in MOFs is critical to the development of these applications.

The importance of probing guest molecules in MOFs lies in the fact that these molecules play a critical role in determining the properties and performance of MOFs. For example, the diffusion behavior of guest molecules can impact the storage and release of gases, while the interactions between guest molecules and the MOF framework can influence catalytic activity and selectivity.[5,6] Understanding the behavior of guest molecules is therefore essential for optimizing the performance of MOFs and developing new applications. However, probing guest molecules in MOFs directly has proven to be a challenge due to the lack of suitable techniques.[4]

In recent years, secondary ion mass spectrometry (SIMS) has emerged as a powerful technique for characterizing MOFs and guest molecules inside.[7] SIMS is a surface-sensitive technique that allows for the identification of compositional information from the surface of a sample. For MOFs, SIMS has the potential to directly probe guest

doi:10.6342/NTU202303887

molecules and investigate their diffusion behavior within the porous network due to its ability of detecting molecular signals and mapping.

Despite the potential of SIMS for probing guest molecules in MOFs, the technique is still relatively underutilized in this area of research. This is due in part to the complexity of the sputtering process, especially for materials composed of both metal and organic.[8] The different sputter rates between the organic and metallic parts could lead to significant preferential sputtering which has been reported in other organic-inorganic composite materials, e.g. organo-halide perovskite.[9] It was found that either monoatomic sputter beam Ar^+ or medium-sized polyatomic sputter beam C_{60}^+ was capable of mitigating the preferential sputtering, while the commonly used giant gas cluster beam Ar_n^+ resulted in ion mixing at interface. Moreover, UiO-66 (University of Oslo), one of the popular MOFs, showed loss of organic signal due to preferential sputtering when Ar^+ was used as the sputter beam in the previous work done by our lab.[10] In order to mitigate the artifact of UiO-66 caused by preferential sputtering, it has been worked out that cosputtering of Ar^+ and Ar_n^+ was able to construct a genuine depth profile of UiO-66.

Therefore, this research started by examining through a range of MOFs synthesized in our lab using different sputtering parameters to find a suitable material to establish a method for analyzing diffusion in MOFs. HKUST-1 and ZIF-8 were the two MOFs used in this research and both were prepared with high crystallinity using methods including spin coating and cathodic deposition. The structures of the obtained MOFs showed high agreement with the structures reported before, reinforcing the result that the MOFs were successfully prepared in our lab.

doi:10.6342/NTU202303887

Sputtering sources with different energy densities including Ar^+, C_{60}^+, Ar_{2500}^+ were utilized to construct depth profiles of the HKUST-1 thin films and ZIF-8 thin films. The sputtering sources were then evaluated using the relative intensities of organic signal at steady state, effective disappearance cross-sections and sputter yields in the depth profiles. It was found out that the organic signal suffered significant damages for HKUST-1 under all sputtering conditions and depth profiles of HKUST-1 could not be obtained without losing the organic signal by using the techniques available in our lab. Nonetheless, for ZIF-8, the organic signal could be preserved relatively well using Ar_{2500}^+ as the sputtering source. Ar_{2500}^+ also showed a low effective disappearance cross-section and a high sputter yield for ZIF-8, suggesting that depth profiles of ZIF-8 thin film could be constructed using Ar_{2500}^+ as the sputtering source with the organic signal preserved and a high sputter yield.

ZIF-8, a well-known MOF with potential applications in gas storage and separation was probed by SIMS to understand the diffusion behavior of guest molecules in MOFs in this study. Specifically, we compared the diffusion behavior of acetaminophen and caffeine, two commonly used drugs, to investigate factors affecting diffusion in ZIF-8. The concentration profiles were fitted according to Fick's second law with a fixed surface concentration and showed a high agreement, allowing quantitative discussion for the diffusion behavior.

First, it was found out that ZIF-8 thin films prepared by spin-coating and cathodic deposition showed different diffusion behaviors. Only ZIF-8 thin films prepared by cathodic deposition showed diffusion behavior through the pores of ZIF-8 in the concentration profiles of the guest molecules due to its well intergrown structure while

doi:10.6342/NTU202303887

guest molecules could enter ZIF-8 thin films prepared by spin coating through space between ZIF-8 nanoparticles.

Moreover, acetaminophen entered ZIF-8 more easily than caffeine due to its smaller molecular size, suggesting that the molecular size of the guest molecules played an important role in diffusion in ZIF-8.

Finally, it was also shown that the molecular size of the solvent also played an important role in diffusion in ZIF-8. Diffusion in a solvent with a larger molecular size turned out to be more difficult and showed a smaller diffusivity.

Compared to the previous work conducted by our lab using UiO-66, these results provide quantitative analysis to the diffusion behavior in MOFs and show new insights into the potential of SIMS for probing these systems.

doi:10.6342/NTU202303887

Chapter 2 Literature review

2.1 Metal-organic framework (MOF)

Metal-organic frameworks (MOFs), which are also known as coordination polymers (CPs), are a group of materials consisting of metal ions coordinated by organic ligands to extend to an infinite array, where CP refers to the bonding nature of the metal-ligand interaction and MOF emphasizes its high crystallinity and porous structure. Figure 2.1 shows the structure of MOF-5, one of the earliest MOF reported by H. Li et al.[15] MOF-5 is constructed by connecting $Zn_4O_{12}C_6$ clusters by terephthalic acid through metal-ligand interaction and shows a well-defined crystal structure with a pore enclosed inside the structure, which is one of the best examples of MOFs. It should not be confused with organic polymers which are macromolecules with monomers or oligomers bonded by covalent bond. MOFs are unambiguously nonmolecular in nature in the way that they are crystalline materials with well-defined crystal structures and cannot be dissolved in solvent like a molecule does.[16]

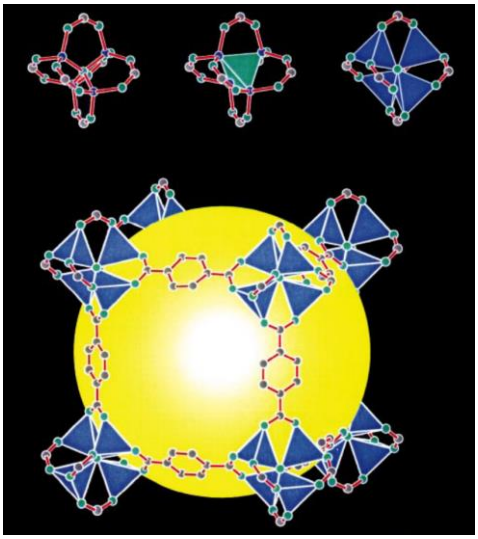

Figure 2.1 Structure of MOF-5, The structure of $Zn_4O_{12}C_6$ cluster is shown in the top of

doi:10.6342/NTU202303887

the figure and MOF-5 is constructed by connecting these clusters together with terephthalic acid (Zn: blue; O: green; C: gray). The yellow sphere depicts the pore enclosed by MOF-5.[15]

2.1.1 Development of MOF

One of the earliest prototypical MOF structures had been synthesized in 1991 by B. Abrahams, B. Hoskins and R. Robson,[17] which was the first time an extensive porous structure composed of organic ligands coordinated to metal ions was realized in a lab. Then in 1995, O. Yaghi and H. Li[18] synthesized a porous material by jointing Cu^{1+} with 4,4′-bipyridine with the XRD result showing a diamond structure where all carbon was replaced with Cu^{1+} and was bonded by 4,4′-bipyridine. In this paper, the term "metal-organic framework" was introduced to the world for the first time and has obtained unprecedented popularity throughout the days.[18]

The nearly infinite combinations of metal ions and coordination organic molecules have given rise to the frequent findings of new MOF structures. However, the instability of these MOF structures had remained as a problem and the collapsing of the porous structures had been unavoidable. In 1999, HKUST-1 (Hong Kong University of Science and Technology)[19] and MOF-5 (Metal-Organic Framework)[15] were synthesized. The remarkable stabilities and the highly porous structures with the unprecedented surface areas have made both of them among the most studied MOF structures even up to today. At the meantime starting from 1998, G. Férey has continuously reported a series of MOF structures named after MIL-n[16–38] (Matériaux de l′Institut Lavoisier, n = 8, 9, 11,14, 16, 17, 18, 19, 23, 24, 25, 27, 32, 36, 37, 38, 41, 42, 43, 44, 45, 57, 58 and 65) but had not

doi:10.6342/NTU202303887

attained considerable attentions until the discovery of the stable Cr(III)-based MIL-53 in 2002.[43] Following the synthesis of the MIL-53 structure, in 2005 G. Férey et al.[44] reported the synthesis of MIL-101 which has drawn even more interests than the report of MIL-53. Combined with computational prediction, the realization of the MIL-101 structure has achieved a material with extremely high pore sizes and surface area. Later in 2006, the ZIF-n (Zeolitic Imidazolate Framework, n = 1-12) series was reported by K. park et al.[45] with exceptional chemical and thermal stabilities. Different from most MOF structures which are composed of transitional metal oxo complex, ZIF-n are composed of transitional metal ion and imidazolate link. ZIFs have gradually become more and more popular since reported, especially for ZIF-8 which has become the most reported MOFs with over 2000 entries containing "ZIF-8" in their titles on Web of Science (searched at 9th Jun. 2023). Another high-profile MOF structure consisting of zirconium oxo complex was reported in 2008 as UiO-66 (University of Oslo).[46] These MOF structures are among the most reported MOF structures today for their outstanding stabilities and unique pore structures.

In the following years, more and more MOFs have been reported and have shown their distinguishing behaviors and applications, including drug delivery[47–50], gas storage[51,52], catalysis[53–55] and separation.[56,57] Figure 2.2 (a) shows the growing popularity of MOFs and figure 2.2 (b) shows a selection of popular MOF each with a large amount of publications. Among them, the microporous structure stands out to be the most prominent feature of MOFs, so it is in great need to understand how molecules transport between these pores.

doi:10.6342/NTU202303887

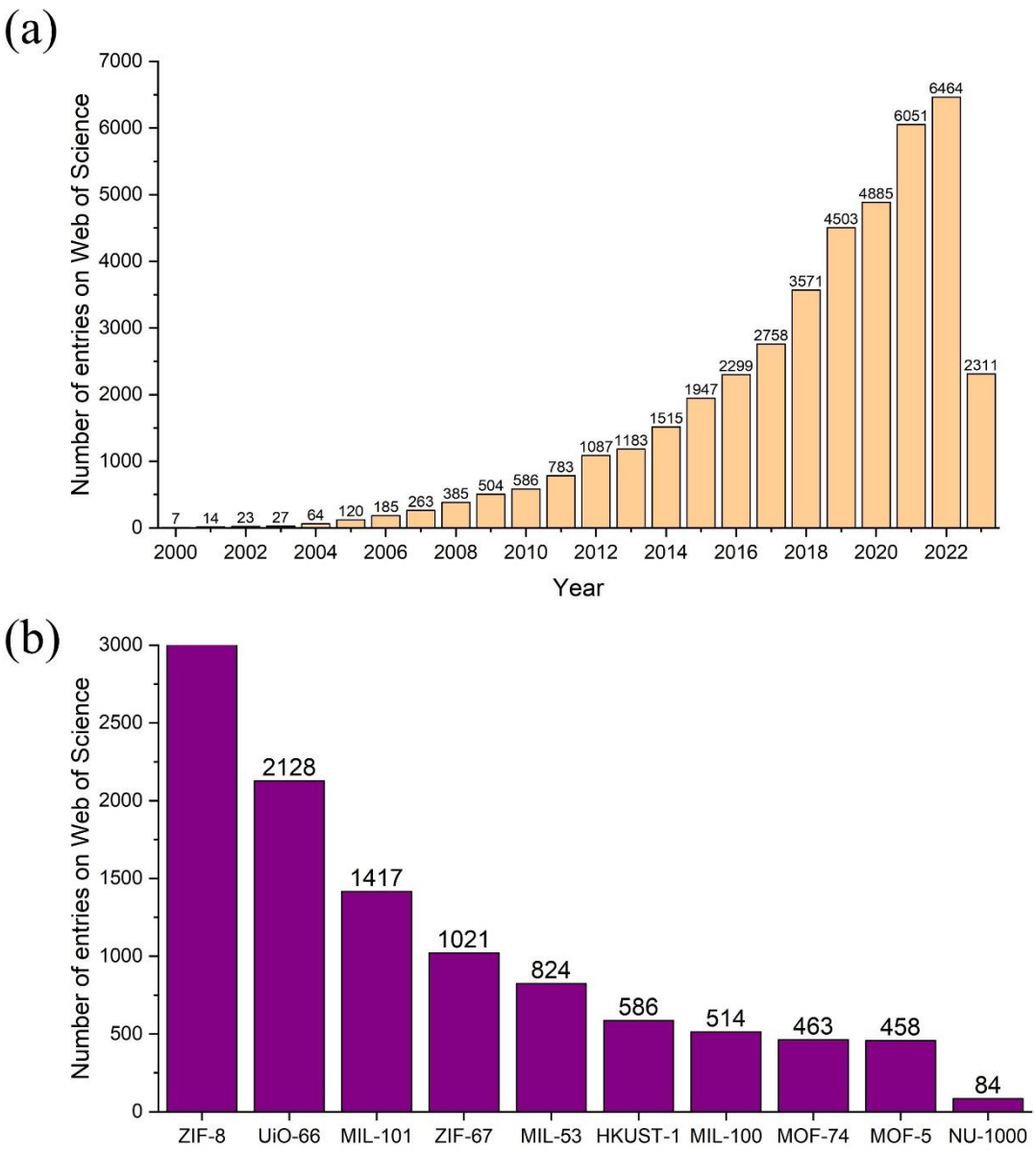

Figure 2.2 (a) The number of entries with "MOF" or "metal-organic framework" in the title on Web of Science. (b) Selection of popular MOF ranked by the number of entries with the name of each MOF in the title on Web of Science. (searched at 9th Jun. 2023)

doi:10.6342/NTU202303887

2.1.2 Synthesis of MOF

MOFs have been reported to be synthesized utilizing a wide range of methods, e.g. solvothermal method,[58–60] microwave-assisted synthesis[61–63] and mechanochemical synthesis.[64–66] However, most of these methods lack the ability to precisely control the morphologies of the obtained MOFs. Therefore, in order to obtain MOFs with the morphologies that could allow the observation of diffusion inside MOFs, which leads to the understanding of the behavior of molecules transport between micropores in MOFs, methods that could yield well crystalline and well intergrown MOFs will be reviewed.

2.1.2.1 Synthesis of large MOF single crystal

The research of the diffusion behavior in MOF microporous structures benefits a lot from the preparation of large single MOF crystals because it could exclude the influence from crystal interfaces and inter-particle diffusion.[67] MOFs have been largely carried out with distinct crystal structures since it was synthesized for the first time by a slow crystallization process where the solution dissolved with both the organic ligand and the metal ion was set in an open vessel for evaporation under ambient environment for 4 days. One of the obtained MOF crystals was then mounted for single crystal XRD and its infinitely extended 3D polymeric network structure was determined.[17]

S. Han et al.[68] has demonstrated the experiment with millimeter-sized MOF-5 crystals which the diffusion of selected dye molecule, namely pyronin B, into the millimeter-sized MOF-5 crystals could be probed by confocal laser scanning microscopy directly and one of the MOF-5 crystals is shown in figure2.3 (a). It has proven the value of large single MOF crystals in exploring the diffusion behavior in MOF structures rather than MOF nanoparticles where the adsorbed locations of the guest molecules are hard to

doi:10.6342/NTU202303887

determine and the diffusion in the MOF structure is difficult to differentiate from the interparticle diffusion. In this paper, the millimeter-sized MOF-5 crystals were prepared by dissolving $Zn(NO_3)_2 \cdot 6H_2O$ and terephthalic acid in diethylformamide (DEF) and heating the solution in an closed vial at 85°C. After heated for 3 days, MOF-5 crystals up to 3×3×2 mm^3 were obtained. It was found out that instead of the commonly described simple Fickian diffusion, reaction-diffusion model describes the diffusion behavior in MOF microporous structures better.[68]

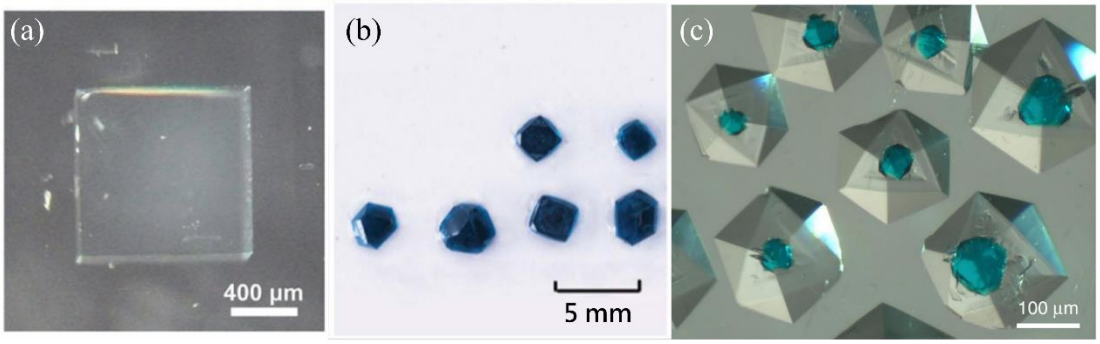

Figure 2.3 Photos of large MOF crystals reported, specifically (a) MOF-5,[68] (b) HKUST-1[69] and (c) HKUST-1@MOF-5 core-shell crystals.[70]

In addition, millimeter-sized HKUST-1 crystals were prepared by L. Li et al.[69] by heating the solution of $Cu(NO_3)_2 \cdot 6H_2O$ and trimesic acid (BTC) at 85°C for 7 days with concentrated nitric acid as the modulator and shown in figure 2.3 (b). Nitric acid could inhibit the deprotonation of BTC and thus limit the rate of the coordination between the BTC and copper (II), yielding HKUST-1 crystals up to a diameter of 5 mm. The HKUST-1 crystals were then employed for the subsequent experiment to determine its ability to separate different organic dyes. It was found out that pyronin B molecules could diffuse

doi:10.6342/NTU202303887

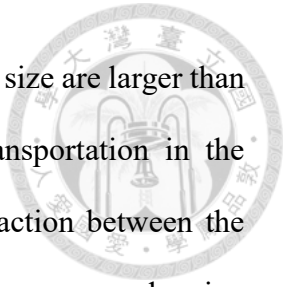

further than thionine molecules in the HKUST-1 crystals despite their size are larger than thionine molecules. The author had suggested that the slower transportation in the HKUST-1 crystals of thionine molecules might be due to the interaction between the unsaturated copper ion sites in HKUST-1 and electron pairs on the more exposed amino groups on the thionine molecules.

Furthermore, computer was employed to calculate if two MOF lattices match each other and MOF-5 crystal was predicted to be able to be grown on the HKUST-1 lattice by O. Kwon et al.[70] Going along the prediction, the experiment was conducted to achieve the predicted result, which carried out HKUST-1@MOF-5 core-shell crystals by preparing HKUST-1 crystals first and then immersing them into the MOF-5 precursor solution for 36 hours at 85°C. The synthesized HKUST-1@MOF-5 core-shell crystals are shown in figure 2.3 (c). This paper not only showcased the capability of computational assistance in the research of MOF crystallography, but also realized large MOF crystals with heterointerface which might be prospective in further research of diffusion behavior in MOF microporous structures with heterointerface.[70]

2.1.2.2 Synthesis of MOF thin films

It has been pointed out by O. Shekhah et al.[71] at 2011 that regardless of the usually obtained powder form of MOF crystals, MOF thin films are vital for probing phenomenon like interaction of guest molecules and the inner pores of the porous MOF structures because of the obscurity to determine if the guest molecules are adsorbed in the inner pores or at the outer surface of the MOF nanoparticles. Besides, some analytical technique

doi:10.6342/NTU202303887

like XPS could not probe the powder form of MOF particles without further processing, which has again shown the necessity of preparing a homogeneous MOF thin film.

Although polymer thin film has been frequently fabricated by spin-coating with high uniformity and reproducibility,[72] MOF thin film fabricated by spin-coating shows obvious gaps between crystals.[73] In order to fabricate a MOF thin film free of gaps, methods like liquid phase epitaxy (LPE), cathodic deposition and vapor-assisted conversion (VAC) have been applied.

2.1.2.2.1 Liquid phase epitaxy (LPE)

LPE is an approach to fabricate a thin film in a stepwise manner, which could be further described as an alternating deposition of the metallic nodes and the organic linkers of a MOF structure onto a functionalized substrate by exposing the substrate to the solutions of the node and the linker alternatively.[74] This stepwise approach provides excellent control over the thickness and the growth orientation of the MOF thin film due to its layer-by-layer growing nature as well as an exceptional technique to probe the growth mechanism of MOF structures when combined with other instruments like surface plasmon resonance (SPR) spectroscopy[75], atomic force microscopy (AFM),[76,77] and quartz crystal microbalance (QCM).[78]

The first LPE of MOF thin film was carried out by O. Shekhah et al.[79] at 2007 by subsequently exposed copper(II) acetate, ethanol, 1,3,5-benzenereicarboxylic acid (BTC) and ethanol to a functionalized Au substrate with COOH-terminated self-assembly monolayer (SAM). The scheme is illustrated in figure 2.4. As a result, layers of highly crystalline HKUST-1 films were obtained and their structures were confirmed with XRD analysis.

doi:10.6342/NTU202303887

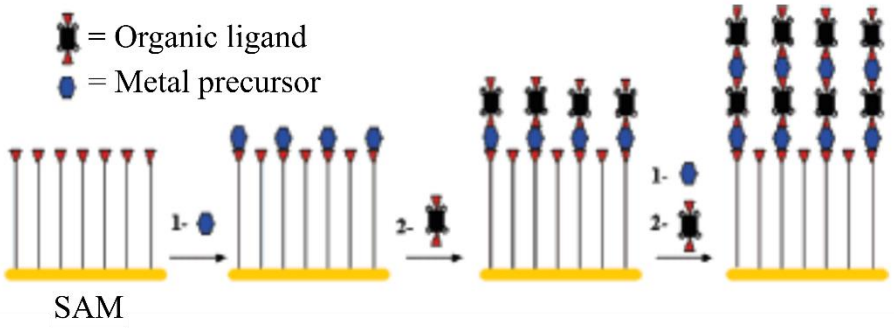

Figure 2.4 Scheme of LPE process on a substrate modified with SAM.[79]

Since then there has been a growing number of works utilizing the LPE technique to prepare a highly crystalline MOF thin film. The realization of LPE fabricated ZIF-8 thin film was brought to feasible by O. Shekhah and M. Eddaoudi in 2013[80] by exposing a Au substrate with OH-terminated SAM to zinc nitrate methanolic solution and 2-methylimidazole (2-mIm) methanolic solution alternatively with methanol used for rinsing between the processes of exposures to the two solutions mentioned above. The XRD data showed two sharp peaks which could correspond to the (110) and (220) planes of a ZIF-8 crystal, indicating a highly orientated ZIF-8 thin film was fabricated. Afterwards, more works have utilized LPE technique to fabricate uniform and homogeneous ZIF-8 thin films[81–84] and showed good performances on gas separation.[82–84] Moreover, highly oriented HKUST-1 thin films were also reported to be fabricated by LPE technique with an exceptional uniformity.[78,85] Figure 2.5 shows one of the MOF thin film prepared by LPE, exhibiting exceptional uniformity.

In 2019, A. Semrau et al.[86] fabricated an UiO-66 thin film, which is a 12-connected MOF structure and is notoriously hard to be deposited in stepwise manner, with a

doi:10.6342/NTU202303887

coordination modulator-assisted LPE technique. In this work, a precursor known as methacrylate protected zirconium-oxo cluster ($Zr_6O_4(OH)_4(OMc)_{12}$) was prepared first by mixing zirconium propoxide with methacrylic acid under inert gas atmosphere. After that, a functionalized silicon dioxide substrate with OH-terminated surface was exposed to $Zr_6O_4(OH)_4(OMc)_{12}$ ethanolic solution and terephthalic acid (BDC) ethanolic solution alternatively to grow a highly crystalline and homogeneous UiO-66 thin film and the methanol uptake of the prepared UiO-66 thin film was tested with a result that has the same performance as conventional UiO-66 powder did.

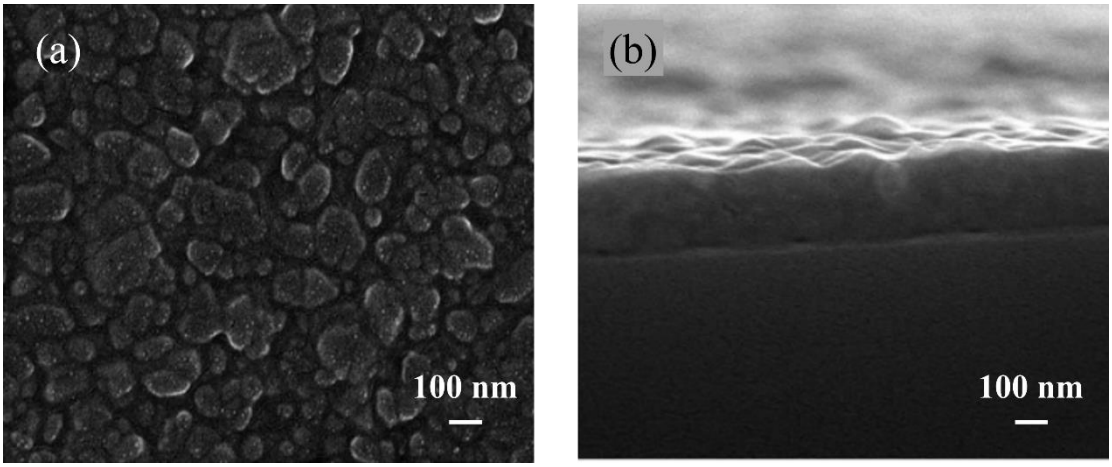

Figure 2.5 SEM images of (a) top-view and (b) cross-section of ZIF-8 thin film prepared by LPE.[81]

2.1.2.2.2 Cathodic deposition

Cathodic deposition of MOF was first realized by M. Li and M. Dincă at 2011[87] where MOF-5 thin film was deposited on an fluorine-doped tin oxide (FTO) glass with a constant voltage of −1.6 V. It was attained by reducing NO_3^- which leads to the generation

doi:10.6342/NTU202303887

of $[OH]^-$ anions around the cathode, resulting in deprotonation of the carboxylic acid molecules which were then coordinated to the metallic cations in the electrolyte to grow into MOF crystals. The crystallization of MOF crystals was confined on the surface of the cathode owing to the accumulation of $[OH]^-$ anion around the cathode, so a homogeneous thin film of MOF could be attained by cathodic deposition. The scheme is illustrated in figure 2.6.

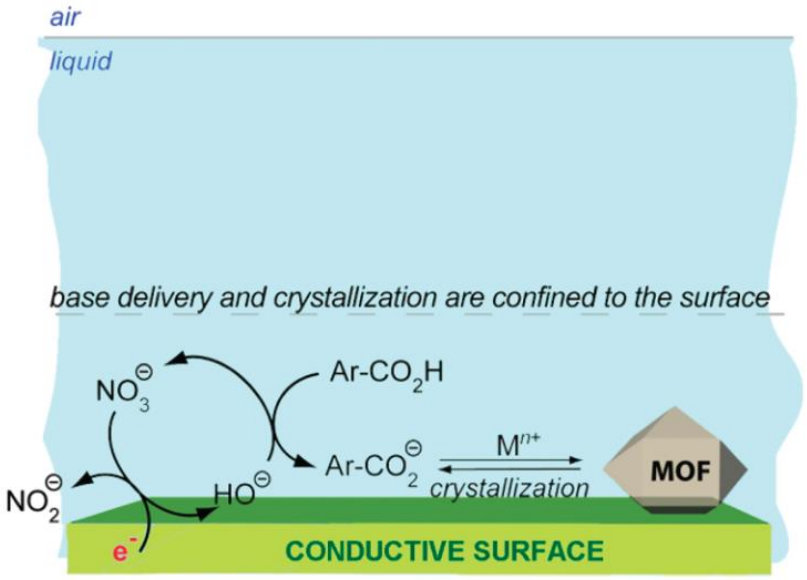

Figure 2.6 Scheme showing the mechanism of cathodic deposition of MOF crystals onto the surface of cathode.[87]

In addition, cathodic deposition of MOF thin films of ZIF-8[14,88,89] and HKUST-1[90] had been realized. ZIF-8 thin films prepared by cathodic deposition usually appear to be well-intergrown and smooth and one on the ZIF-8 thin films is shown in figure 2.7.[14,88,89] The well-intergrown ZIF-8 thin film deposited on an anodic aluminum oxide (AAO)

doi:10.6342/NTU202303887

substrate has shown remarkable permeance and selectivity for propylene/propane separation which is highly prominent for industry combined with the high thermal stability of the ZIF-8 thin film.[14] In addition to cathodic deposition of ZIF-8 thin films on AAO substrates, G. He et al. also showed the accessibility to deposit ZIF-8 thin films across a board range of materials including indium tin oxide (ITO) substrate, polyacrylonitrile (PAN) support, Cu foil and nanoporous carbon film.[88] Moreover, applying current-controlled cathodic deposition of ZIF-8 thin films could yield a ZIF-8 thin film with the ZIF-8_Cm polymorph, which is stiffer than the common ZIF-8 structure with the ZIF-8_$I\bar{4}3m$ polymorph. Therefore a superior propene/propane separation performance had been expected because of the pores with less flexibility restricting propene molecules to pass through.[89]

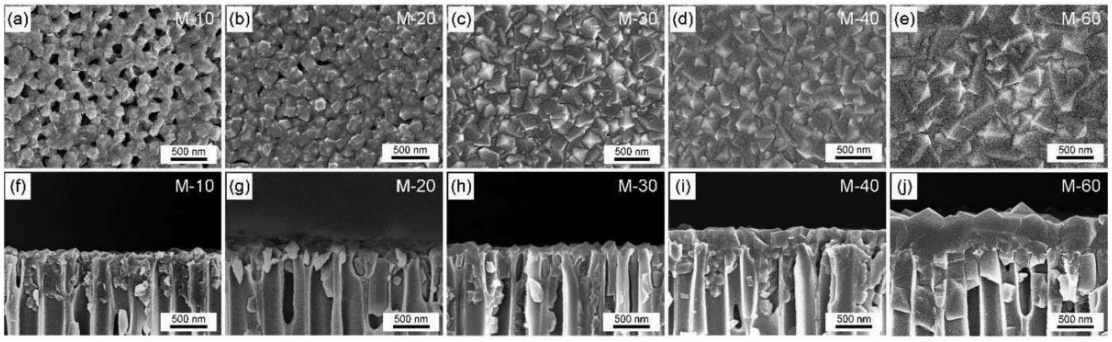

Figure 2.7 SEM images of the ZIF-8 thin film prepared with cathodic deposition from (a-e) top-view and (f-j) cross-section at 10 minutes, 20 minutes, 30 minutes, 40 minutes and 60 minutes respectively.[14]

doi:10.6342/NTU202303887

2.1.2.2.3 Vapor-assisted conversion (VAC)

Vapor-assisted conversion (VAC), which is a method adapted from steam-assisted conversion (SAC), employs solvent vapor, sometimes containing modulators like Lewis acids as well, to aid the reaction taking place on a support mounting with precursor. The precursor could either be solid or solution. VAC makes the most of preparing a thin film with controlled growth on a wide variety of supports in a reaction time which is usually shorter than LPE method.[91] Figure 2.8 shows a schematic illustration of a VAC reaction.

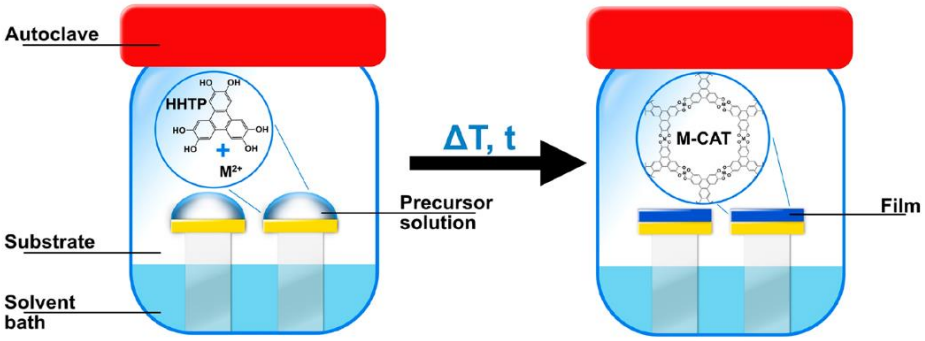

Figure 2.8 Scheme of the process and the reaction cell for VAC. [92]

Following the work by Q. Shi et al.[93] which had fabricated ZIF-8 and ZIF-67 structures using SAC, the VAC of a MOF structure was first carried out by H. Zhang et al.[94] with nonpolar n-heptane as the solvent, although the result was only prototypical and showed distinct ZIF-8 crystals with apparent gaps between each crystal.

Nonetheless, MOF thin films have been fabricated by VAC with high uniformity and controlled orientation in numerous works afterwards.[91,92,95,96] UiO-66 thin film was fabricated on a Au substrate without modification using $ZrOCl_2$ and BDC as the precursor

doi:10.6342/NTU202303887

and DMF vapor and acetic acid as the modulator. The resulted thin film gave sharp peaks in XRD pattern indicating the growth along (111) orientation of the UiO-66 thin film and a smooth and homogeneous morphology was observed under SEM and AFM. The SEM images are shown in figure 2.9. The accessibility of the porous structure was also tested employing the ethanol adsorption isotherm, showing that guest molecules could be accommodated in the pores of the obtained UiO-66 thin film.[95]

Besides, MOF thin films including the two-dimensional triphenylene-based metal-catecholate (M-Cat-1, M = Ni^{2+} or Co^{2+}) series and the MOF-74 series (M = Zn^{2+}, Mg^{2+}, Ni^{2+} or Co^{2+}) were fabricated by VAC across a wide range of substrate ranging from gold, quartz, ITO to silicon.[92,96,97] The fabrication of the MIL-53 (Al) thin film has also been reported to be carried out on a collection of non-modified substrates including glass, silicon or alumina.[91]

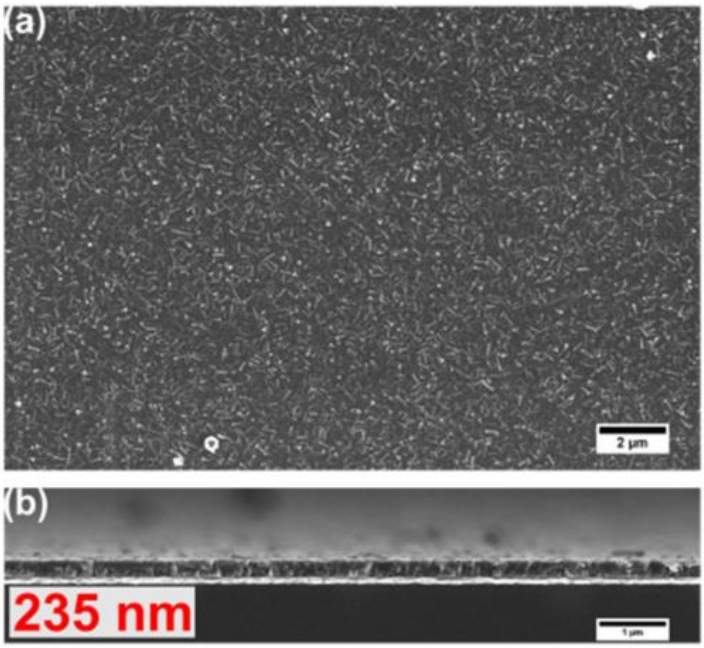

Figure 2.9 SEM images of UiO-66(NH_2) thin film prepared by VAC from (a) top-view and (b) cross-section. It shows a thin film with a thickness of 235 nm.[95]

doi:10.6342/NTU202303887

2.1.3 Drugs delivery systems (DDSs) based on MOFs

Drug delivery systems (DDSs) are technologies designed for controlled drug release to improve therapeutic efficacy or alleviate side effects. It is achieved by maintaining a desired concentration of active pharmaceutical ingredients at the targeted biological site.[98] Nanomaterials have attracted more and more interests as drug delivery systems, including MOFs,[99] liposomes,[100] micelles,[101] dendrimers,[102] polypeptides[103] and zeolites.[104] Among them, MOFs stand out for their highly porous structures with unprecedented surface areas and high tunability for their functionalities, pore sizes and topologies.[105]

MOF was first studied as a DDS in 2006.[106] In this work, MIL-100 and MIL-101 were used for ibuprofen delivery and the release profile was measured by high performance liquid chromatography (HPLC). The release profile is shown in figure 2.10 and MIL-101 showed a much higher loading capacity which was four times higher than MCM-41, a conventional zeolite material with a similar cage size as MIL-101, and a longer delivery time, which were both desired features for a DDS. The great potential of MOFs as DDSs was illustrated in this work and the number of studies about MOFs as DDSs has grown throughout these years.

doi:10.6342/NTU202303887

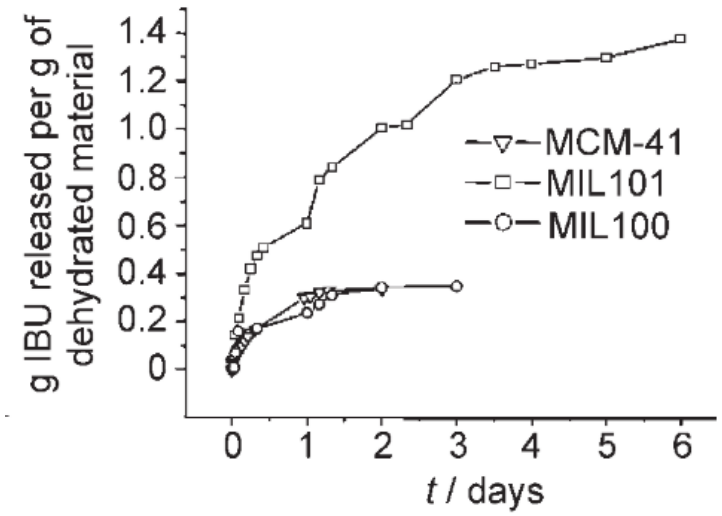

Figure 2.10 The amounts of ibuprofen released from MCM-41, MIL-101 and MIL-100 measured by HPLC.[106]

P. Horcajada et al.[107] explored the drug delivery potentials of a range of iron-centered MOFs with different pore sizes and topologies, namely MIL-89, MIL-88A, MIL-100, MIL-101_NH2 and MIL-53. Iron-centered MOFs stood out as a favorable DDS because they not only possess a less toxic metallic node but also show paramagnetism which makes targeted delivery more feasible. In addition, a variety of drugs including hydrophilic, hydrophobic and amphiphilic with different particle sizes was studied as active pharmaceutical ingredients (APIs) in this work, including the antitumoral drug busulfan which had only been loaded in DDSs like liposomes or polymers for less than 6 wt%. Nonetheless, the loading capacity of busulfan in MIL-100 was determined to be 25 wt% which greatly exceeded the loading capacity in all DDSs reported before, showing the value of MOFs for delivery of some of the challenging drugs. It was suggested that the loading capacity was determined by the pore sizes of MOFs due to the fact that very

doi:10.6342/NTU202303887

low loading capacities were observed for cases where the drug has a larger dimension than the pore size of the MOF. Moreover, progressive release without burst effect was demonstrated in this work and the release profiles are shown in figure 2.11. The delivery processes were achieved through the diffusion from MOFs matrixes rather than degradation of MOFs. Finally, toxicity of the MOF nanocarriers was tested *in vivo* on rats and showed only temporary accumulation of the nanoparticles in organs for less than three months.

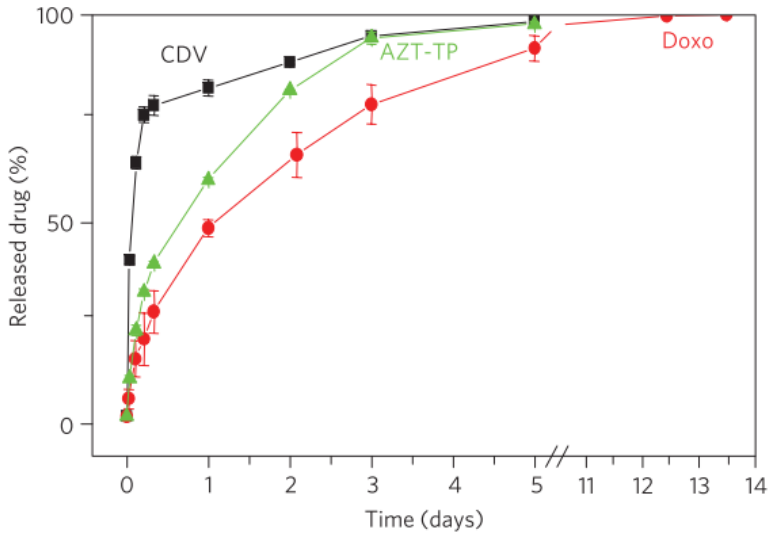

Figure 2.11 Delivery of cidofovir (CDV, black), doxorubicin (doxo, red) and azidothymidine triphosphate (AZT-TP, green) in PBS at 37°C from MIL-100 nanoparticles.[107]

Nevertheless, large molecules were also shown to be capable of being encapsulated into MOFs structure. Zheng et al. showed that the anticancer drug doxorubicin (DOX) could be encapsulated into the ZIF-8 crystal by a one-pot synthesis method while the size of the DOX molecule is larger than the pore size of the ZIF-8 structure. It was found out

doi:10.6342/NTU202303887

that DOX was encapsulated into the mesopores of the ZIF-8 crystals as the ZIF-8 crystals forming. The TEM images of the encapsulated DOX are shown in figure 2.12.[108]

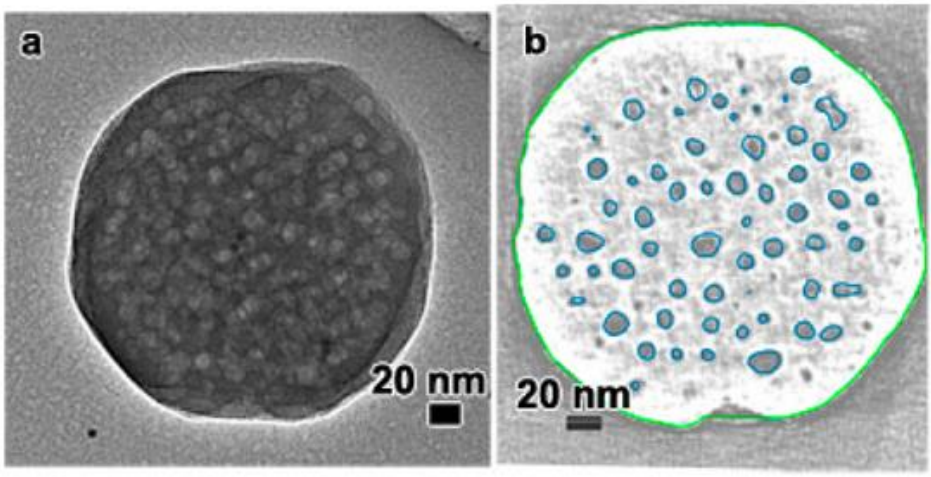

Figure 2.12 DOX distribution in the mesopores in a DOX@ZIF-8 particle illustrated by electron tomography. (a) TEM image of a DOX@ZIF-8 single crystal. (b) Cross-section of the electron tomogram with the mesopores marked by blue lines.[108]

HKUST-1 nanoparticles were demonstrated by S. Gautam et al.[109] to be capable of adsorbing molecular drug, acetaminophen, with an extraordinary amount. The loading of acetaminophen was determined by UV-vis spectra in this work, where the amount of UV light adsorbed by acetaminophen molecules in the solution before and after addition of HKUST-1 nanoparticles was used as the indication of the acetaminophen molecules loaded into the HKUST-1 nanoparticles. The UV-vis spectrum is shown in figure 2.13 and the result revealed the exceptional ability of adsorbing acetaminophen for HKUST-1 nanoparticles. Nonetheless, this method lacks the ability to probe the molecules loaded in the MOF structure directly, resulting in the fact that we do not know where the drug

doi:10.6342/NTU202303887

molecules had been loaded in the MOF structure.

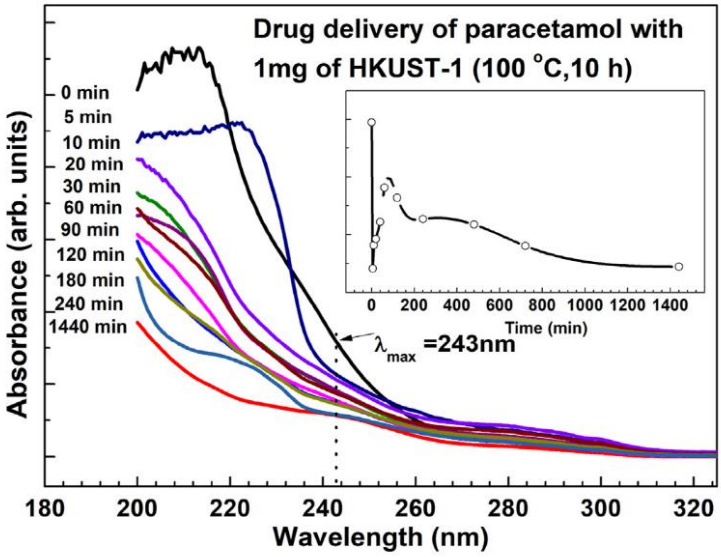

Figure 2.13 The UV-vis spectrum of the acetaminophen aqueous solution measured at different time after the addition of HKUST-1 nanoparticles.[109]

There have been various kinetic models proposed trying to describe the drug delivery process mathematically, but there is no general agreement across different MOFs or different experiment.[110–112] However, it was suggested recently that the real drug delivery process of MOFs lies between zero-order, first-order and Higuchi models due to the complex manner of the process which depends on diffusion, dissolution and decomposition of the carriers.[113]

2.1.4 Mass transfer in MOFs

The mass transfer behavior of metal-organic frameworks (MOFs) has been a subject of serious investigation for decades. The diffusion process in MOFs is affected by various

doi:10.6342/NTU202303887

factors such as pore size, pore topology, framework flexibility, defects, guest-MOF interactions, and guest-guest interactions.[114]

The first experimental study for diffusion in MOF was conducted in 2006 by F. Stallmach et al.[115] In this work, the diffusivities of hydrocarbon gases in MOF-5 crystals were measured to be $D = 2.0 \times 10^{-6}$, 2.0×10^{-7}, 1.8×10^{-9} and 1.3×10^{-9} m^2 s^{-1} for methane, ethane, n-hexane and benzene respectively using pulsed field gradient nuclear magnetic resonance (PFG NMR). The diffusivities were extraordinarily high compared with conventional porous materials including zeolites, metal oxides, resin or carbons and were attributed to the high porosity, high surface area and continuous nanoporous structure of MOF-5.

However, diffusion in MOFs is more complex than Fickian diffusion, as demonstrated by S. Han et al. in a study where they measured the concentration profiles of pyronin B (PB), a common dye molecule, migrating into a single MOF-5 crystal using confocal microscopy. The concentration profiles are shown in figure 2.14. They found that the equilibrium concentration of PB inside MOF-5 crystals was higher than the concentration of PB in the solution around the MOF-5 crystals. It was suggested that a reaction-diffusion model, rather than a pure diffusion model, may better describe diffusion in MOFs.[68] Additionally, a more recent study showed that the diffusivities of molecules in MOF-5 are dependent on the thickness of MOF-5 and the interaction between molecules and MOF-5, indicating the need for further investigation to fully understand diffusion in MOFs.[116]

doi:10.6342/NTU202303887

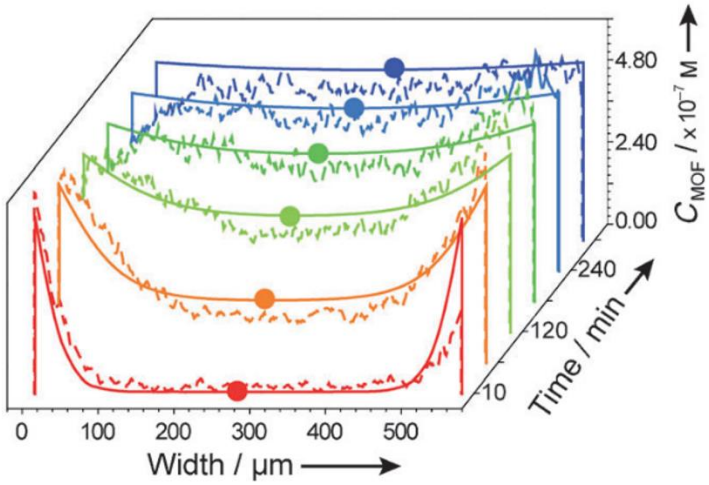

Figure 2.14 Concentration profiles of PB measured throughout a duration of time.[68]

In addition to MOF-5, diffusivities for other MOFs have also been reported. The diffusivity of HKUST-1 was measured by O. Zybaylo et al.[117] using a HKUST-1 thin film prepared by LPE on an Au-coated QCM crystal. Pyridine was chosen as the analyte, and the apparent change in the mass of the HKUST-1 thin film after exposure to pyridine vapor was measured using QCM. The uptake of pyridine is shown in Figure 2.15, and the dashed line represents the fitting result according to Fickian diffusion. Although the diffusion coefficient of HKUST-1 was calculated to be $D = 0.7 \times 10^{-19}$ m^2 s^{-1}, it was also noted that this experiment did not satisfy all the requirements of Fickian diffusion, and further discussion is needed to fully describe the diffusion behavior in MOFs.

doi:10.6342/NTU202303887

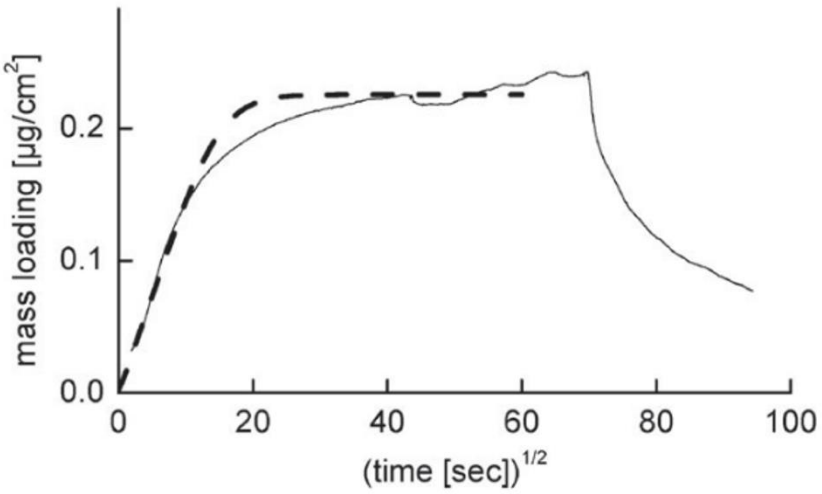

Figure 2.15 Mass loading of pyridine into HKUST-1obtained by QCM plotted against square root of adsorption time.[117]

Moreover, diffusivity of ZIF-8 thin film was measured by J. Tuninetti et al.[118] using the electroactive species $Fe(CN)_6^{3-}$ as the probe and collecting the cyclic voltammetry with different scan rates. Given the diffusion-controlled electron transfer could be described by:

$$j_p = 0.4463nFC(\frac{nF}{RT})^{1/2}v^{1/2}D^{1/2} \qquad \text{Eq 2.1}$$

where j_p is the voltammetric peak current, v is the scan rate, D is the diffusivity of $Fe(CN)_6^{3-}$, F is Faraday's constant, C is the concentration of $Fe(CN)_6^{3-}$, n in the number of electrons transferred, R is the molar gas constant, and T is temperature. Thus, the diffusivity D could be obtained by the slope of j_p v.s. $v^{1/2}$. The plot is shown in figure 2.16. The obtained D showed decrease with increasing MOF deposition cycles, which was

doi:10.6342/NTU202303887

suggested to be due to the increase of the tortuosity of the diffusional path in ZIF-8 thin film after introduction of additional ZIF-8 layers.

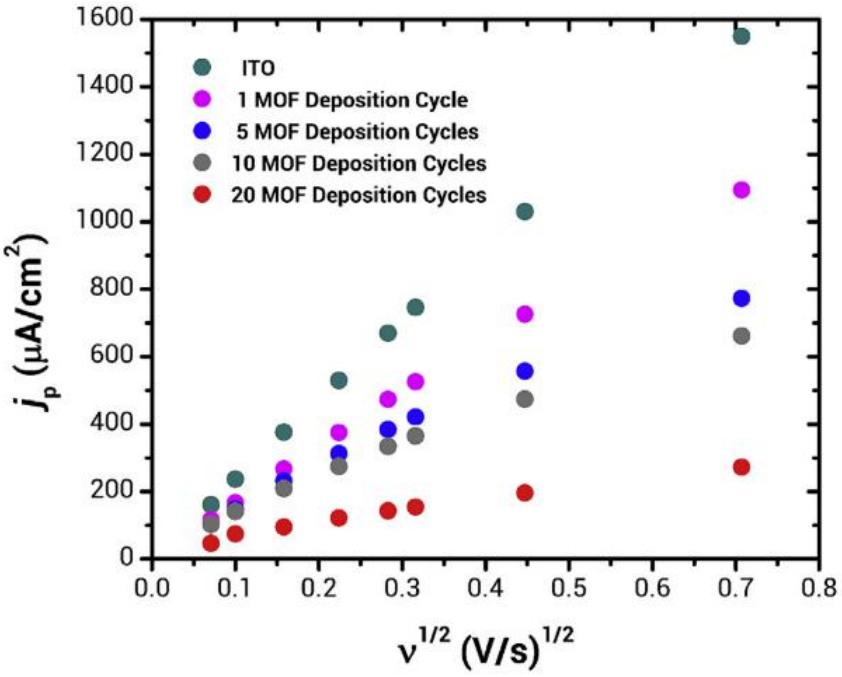

Figure 2.16 Plots of j_p v.s. $v^{1/2}$. D could be obtained by the slopes and showed a decrease with increasing deposition cycles.[118]

To sum up, there have been numerous approaches trying to understand the diffusion behavior in MOFs and each of them were proven to provide information from different aspect of sight.

2.1.5 Depth profile of MOF

To determine the porous structure of MOF thin films has been a challenging work for a long time. Nonetheless, advances in instrumentation and the theory of physisorption have proven to be helpful for providing information about the porous structure of the

doi:10.6342/NTU202303887

MOF thin films. Among them, Positron annihilation lifetime spectroscopy (PALS) can probe the pore size of the thin films of MOFs by measuring the lifetime of the incident positron and the depth of it by altering the incident energy of the positron, providing a method of direct depth profiling. Figure 2.17 shows the obtained PALS of a ZIF-8 thin film on a Si substrate, and a measured pore diameter throughout the specimen of 11.5 Å agrees with the theological pore size of the ZIF-8 crystal structure (11.6 Å). Besides, the intensity of the detected positron annihilation is strong in the depth of ZIF-8 thin film and quickly decays in the depth of Si substrate because the micropores only exist in ZIF-8 thin film but not in Si substrate.[119]

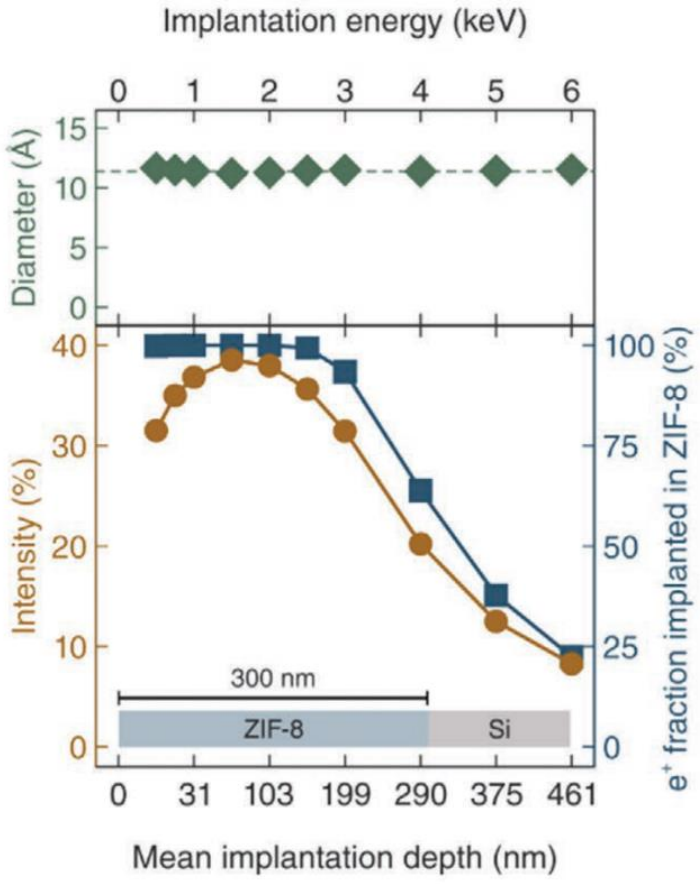

Figure 2.17 PALS of a ZIF-8 thin film on a Si substrate.[119]

doi:10.6342/NTU202303887

Ion beams were proven to be valuable in depth-profiling of MOFs by Wagner et al.,[120] where the depth-profiling of [FeFe](mcbdt)$(CO)_6$ (mcbdt = 2,3-dithiolato-benzoic acid) in UiO-66 thin films have been conducted using Time-of-Flight Elastic Recoil Detection Analysis (TOF-ERDA), Rutherford Backscattering Spectrometry (RBS) and Time-of-Flight Medium Energy Ion Scattering (TOF-MEIS). The results are shown in figure 2.18. However, there are restrictions for all three analysis methods mentioned above. TOF-ERDA cannot reveal the depth of the elemental distribution if the surface of the sample is rough; RBS has limited depth resolution due to its limited energy resolution; TOF-MEIS cannot determine the accurate depth of the element implanted in the MOFs because the energy loss of organic materials, like MOFs, remains not well established. Nonetheless, all three techniques revealed that [FeFe](mcbdt)$(CO)_6$ is only rich near or at the surface of the UiO-66 thin film.

doi:10.6342/NTU202303887

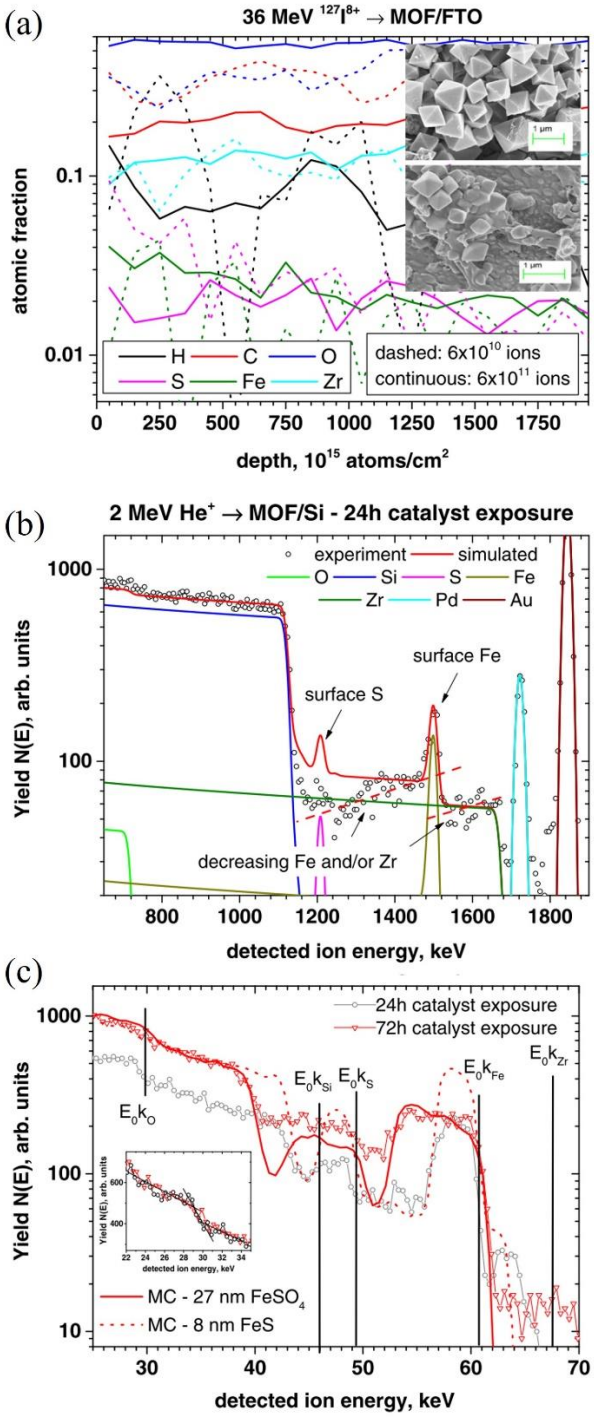

Figure 2.18 Depth profile constructed by (a) TOF-EDRA, (b)RBS and (c) TOF-MEIS. The inset in (a) exhibits the SEM images of the UiO-66 crystals before (top) and after (bottom) the incident of the ion beam.[120]

doi:10.6342/NTU202303887

Depth profile of molecules adsorbed onto the MOF structure has also been constructed by angle-resolved XPS and Ar^+ sputtering. The experiment conducted by Yan et al.[121] utilized ABMOF-1 crystals as the adsorbents and 2,6-dinitro-4-trifluoromethyl phenol (2,6-DNP-4-CF_3) as the adsorbate. Figure 2.19 shows the XPS spectra of (a) Zn $2p_{3/2}$ and (b) F 1s of ABMOF-1 exposed to 2,6-DNP-4-CF_3. The red curves which was collected at a higher take-off angle and contained more information about the surface of the specimen than the blue curves show a higher ratio of the intensity of F 1s to Zn $2p_{3/2}$. As the result of the extraordinary surface sensitivity of XPS, it could be concluded that the distribution of the adsorbates was limited to the outermost layer of the ABMOF-1 crystals, which is a reasonable result considering the fact that the size of the 2,6-DNP-4-CF_3 molecule is larger than the size of the pore of ABMOF-1 crystals. The signals collected after irradiation of Ar^+ show an even lower ratio of the intensity of F 1s to Zn $2p_{3/2}$, suggesting that 2,6-DNP-4-CF_3 barely appears under the surface of the specimen.

doi:10.6342/NTU202303887

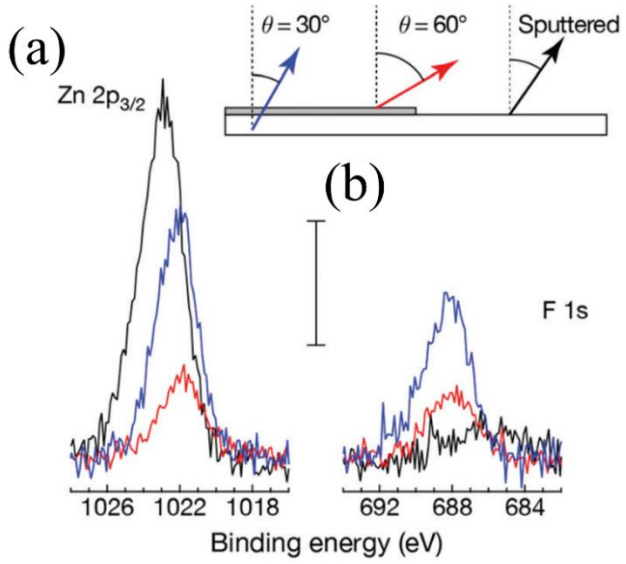

Figure 2.19 XPS spectra of (a) Zn $2p_{3/2}$ and (b) F 1s of ABMOF-1 exposed to 2,6-DNP-4-CF_3. (blue: take-off angle 30°; red: take-off angle 60°; black: after Ar^+ sputtering) [121]

However, the depth profile constructed by the Ar^+ sputtering may not reveal the distribution of the adsorbates truthfully due to the strong preferential sputtering caused by Ar^+ which has been reported before.[122] Moreover, owing to the organic-inorganic hybrid structure in the MOF structure, it has been reported by our lab that MOF structure is more prone to the preferential sputtering effect when a monoatomic ion beam is used as the sole sputtering source.[10]

Furthermore, the techniques mentioned above all lack the ability to provide information about molecular structure, limiting these techniques only suitable for differentiating different elements but organic molecules composed of only C, H, O and N. Especially for drug delivery, where most drugs are organic molecules, this limitation may hinder the understanding of transportation of drug molecules in MOFs. To overcome this

doi:10.6342/NTU202303887

limitation, time of flight secondary ion mass spectrometry (ToF-SIMS) stands out for its ability to provide not only elemental information but also information about molecular structure of nearly all solid sample. Thus, ToF-SIMS will be reviewed in the following section.

2.2 Secondary ion mass spectrometry (SIMS)

2.2.1 Mass Spectrometry (MS)

Mass spectrometry is a technique that has been widely employed across various fields of study, including geology, biology, pharmacology and material science.[123–125]. MS measures the mass-to-charge (m/z) ratio of a gas phase ion which is generated from an analyte by an ionization process and a mass spectrum shows the counts of ions verses m/z. The simplified working principle of MS is demonstrated in figure 2.20 showing that an analyte is first ionized in an ion source, and then these ions enter an analyzer where the m/z of these ions are determined. Finally, these ions enter a detector and the counts of the ions with different m/z are calculated. Although MS only provides information about m/z and its counts, the true value of MS lies behind the structure information which could be deducted from these data.[126]

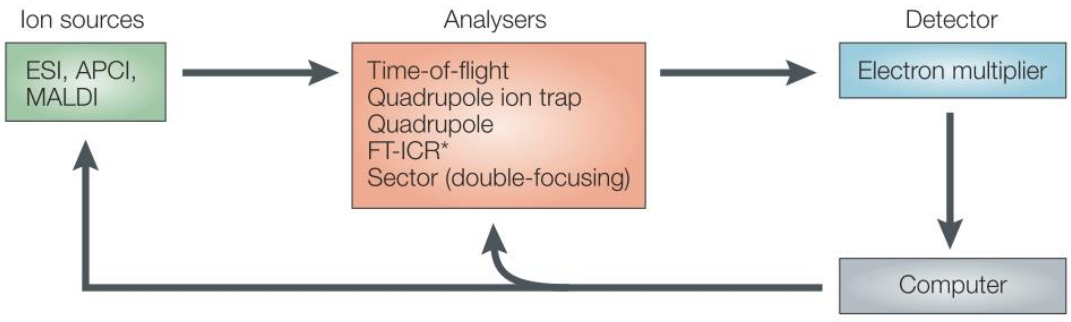

Figure 2.20 A scheme for the basic working flow of a mass spectrometry. Electrospray

doi:10.6342/NTU202303887

ionization (ESI); atmospheric-pressure chemical ionization (APCI); matrix-assisted laser desorption/ionization (MALDI); Fourier-transformation ion-cyclotron resonance (FT-ICR). *FT-ICR does not use electron multiplier.[126]

In order to collect a MS spectrum, we need to ionize the analyte with an appropriate ion source first. Common ion source includes electron impact (EI), chemical ionization (CI), electrospray ionization (ESI), fast atom bombardment ionization, field desorption ionization, and matrix-assisted laser desorption/ionization (MALDI).[127]

Among them, ESI and MALDI appear to be the most dominant method when it comes to ionizing macromolecule, which have brought the MS technique to the field of biology.[128] The earliest concept of ESI was first brought to be feasible by M. Dole et al. where polystyrene molecules with the mass of 411000 Da were ionized and detected in a Faraday cup. The polystyrene was first dissolved in a slightly conductive solvent (7.4×10^{-9} $cm^{-1} \cdot \Omega^{-1}$) and then formed charged droplets by being sprayed through a hypodermic needle where ESI has gotten its name from. Then the solvent of these charged droplets evaporated while traveling. When the solvent evaporated, charges remained on the polystyrene molecules and thus ionized them into macroions without strong impact that might cause fragmentation of the molecules.[129] ESI has been proven to be valuable in determining the structure of large molecules, e.g., fucoidan,[130] pyrethroid[131] and polyphenol.[132]

On the other hand, the prove of concept of MALDI was first realized by M. Karas, D. Bachmann and F. Hillenkamp by demonstrating that the ion yield of alanine had been enhanced and, at the same time, the irradiance of the laser needed to desorb alanine had

doi:10.6342/NTU202303887

been reduced significantly by the assistance of the tryptophan as the matrix. Because tryptophan could adsorb the irradiated laser, it could transfer energy to the nonadsorbing molecules and also act as a proton donor at excited state to help ionizing other molecules. Thus a high ion yield with limited fragmentation could be obtained with the assistance of the matrix and this technique was further developed into MALDI.[133] Same as ESI, MALDI has demonstrated its value in determining the structure of large molecules, e.g., peptide,[134] lipid[135] and polyphenol.[136]

2.2.2 Working principle of secondary-ion mass spectrometry (SIMS)

As for SIMS, a focused primary ion beam is used as the ion source which is composed of high-energy ions typically at the range of 0.1-50 keV. The primary ion beam is focused onto the surface of the target material and the energy of the primary ion beam will be transferred to the target material by collision cascade. The atoms or molecules of the target material could be displaced from the surface if the energy is higher than the threshold displacement energy where there is a possibility that a displaced atom or molecule could lose or obtain one or more electron(s) to become an ion. The scheme is shown in figure 2.21.[137] These ions, which are referred as secondary ions, will be then extracted and focused through an electromagnetic system to enter a mass spectrometer to separate them by their mass to charge ratio for mass spectrometry analysis. Although SIMS could not compete with ESI nor MALDI in the high mass range, SIMS could provide information from a surface of a sample with only limited sample preparation which could preserve the information of the localization of the generated ions. Thus, SIMS is recognized as a technique that is capable of providing information of molecular

doi:10.6342/NTU202303887

composition from the real surface of a sample. This advantage also makes it accessible to depth profiling for SIMS rather than other techniques like ESI and MALDI.[138]

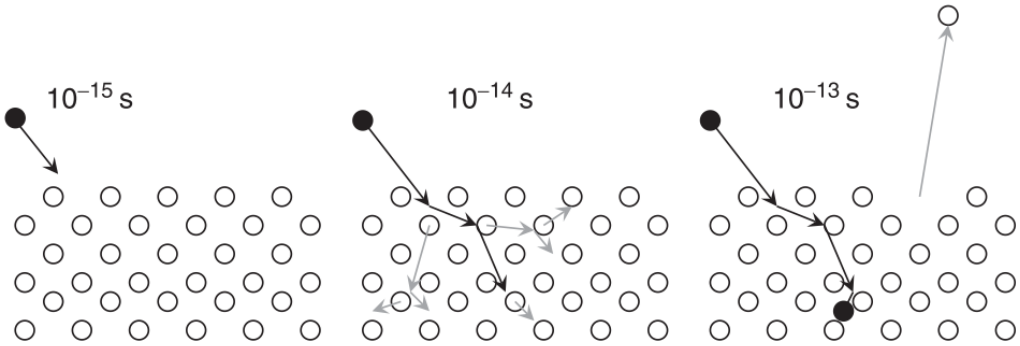

Figure 2.21 A schematic illustration of collision cascade and the formation of secondary ions.[139]

Although formation of secondary ions has been briefly described in collision cascade, there is still no comprehensive theory of it. The equation describing the relation between intensity of a secondary ion and other parameters is only empirical and shown below:[140]

$$i_A^S = I^p \cdot Y \cdot \alpha_A \cdot \eta_A \cdot \theta_A \cdot x_A \qquad \text{Eq. 2.2}$$

where i_A^S is the measured secondary ion intensity of A; I^p is the primary ion intensity; Y is the sputter yield; α_A is the ionization probability; η_A is the combined transmission efficiency of the extraction optics, the mass spectrometer and the detector; θ_A is the isotopic abundance; and x_A is the atomic fraction of element A. It could be concluded that the formation of secondary ions depends on a number of factors, including element of interest, matrix of the sample, pressure in the analysis chamber, crystal

doi:10.6342/NTU202303887

orientation, primary ions, incident angle and construction of the instrument. The significance of each factor varies from case to case which makes it more complicated and brings difficulty to quantitative analysis for SIMS. Formation of molecular ions which involves cleavage of a molecule is even more complicated and makes quantitative analysis of molecular ions more challenging than quantitative analysis of elements.

2.2.3 Development of SIMS

The development of SIMS could be dated back to 1931 where secondary ions were first produced by irradiating Li^+ on a range of filaments under a vacuum environment, and the detected negatively charged ions included OH^- and Cl^-.[141,142] Afterwards, in 1949 the first SIMS had been installed experimentally by R. Herzog and F. Viehböck and the sketch is shown in figure 2.22,[143] where secondary ions were generated, focused and collected for further mass spectrometry analysis despite in a low yield.

doi:10.6342/NTU202303887

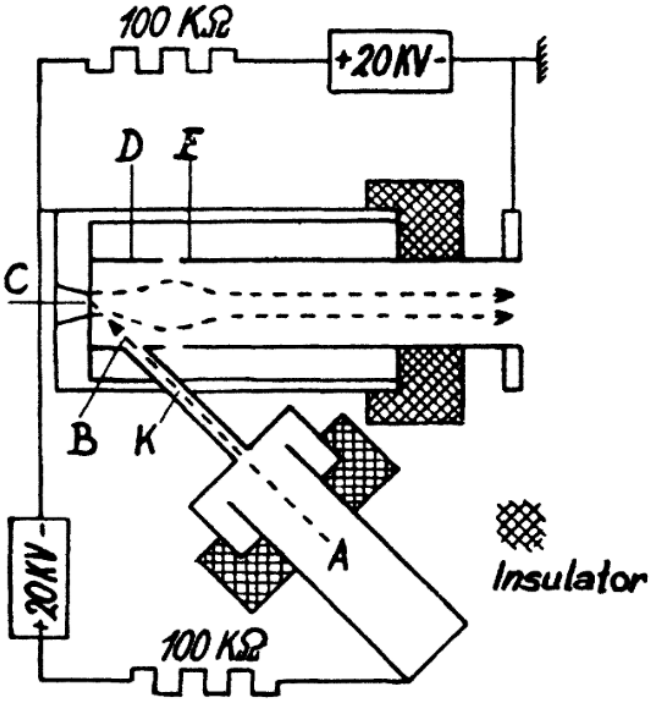

Figure 2.22 The sketch of the first SIMS installed.[143]

At first, SIMS was mainly used for analysis of geological and semiconductor samples due to its exceptional sensitivity for elements. In 1970, static SIMS was invented which utilized a considerably less intense primary ion (10^{-9} A cm^{-2}), leaving most of the outermost monolayer of the sample untouched from the primary beam.[144] The invention of static SIMS inspired many new fields in SIMS analysis including heterogeneous catalysis, nanotechnology, medicine, polymer and material science.[138]

Another great breakthrough for SIMS is the development of ToF analyzer. In 1981, the first application of ToF-SIMS was reported.[145] Advantages of ToF-SIMS include an unlimited mass range and a very high transmission compared with the most dominating magnetic sector instruments at that time. The high transmission was particularly

doi:10.6342/NTU202303887

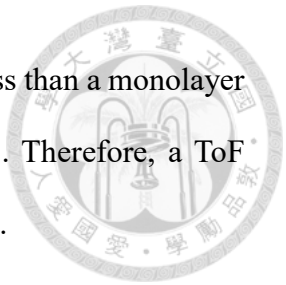

important for the development of static SIMS because there is only less than a monolayer of the sample sputtered and entering the analyzer in a static SIMS. Therefore, a ToF analyzer has nearly become the standard instrument for a static SIMS.

In 1989, the first application of a small-sized cluster ion beam (SF_6^-) as the primary beam for SIMS was reported. SF_6^- showed secondary ion yield for molecular ion peaks with 9 to 24 orders of magnitude higher than using other atomic ion beams, proving the potential of using cluster ion beams as the primary ion beam for SIMS, especially for the analysis of organic materials.[146] Following the use of SF_6^-, many other cluster ion beams were employed for SIMS including Au_3^+, C_{60}^+ and Ar_{100}^+ which all showed improved secondary ion yields for molecular ions.[147–149]

After years of effort, SIMS has been developed into a widely applied technique that is capable of detecting not only elemental information but also molecular composition from a surface of a solid sample. All elements within the periodic table and their combinations could be detected by SIMS with exceptional detection limit that is capable of detecting even trace of compounds in the samples as little as sub parts per billion level. Moreover, the focused primary ion gives rise to the imaging ability of SIMS, which has a spatial resolution of 1 μm or less and a depth resolution of about 1 nm. Additionally, most solid sample could be analyzed with SIMS without prior sample preparation process. These features have drawn wide interest from both industry and academic toward SIMS, making SIMS one of the most utilized surface analysis technique.[139]

2.2.4 Dynamic SIMS and static SIMS

SIMS was known as a destructive method that involved analyzing the ions emitted from the surface of the sample bombarded by an energetic ion beam. This process resulted

doi:10.6342/NTU202303887

in constant removal of the surface, and a mass spectrum throughout the depth of the sample was obtained.[150] On the other hand, if the incident beam's dose is less than 10^{12} ions/cm^2, less than 1 % of the sample's surface area is affected by the beam because the affected area of an incident ion is typically smaller than 10 nm^2. This dose is commonly referred to as the static limit, and the sample's surface is considered to retain its original state when the incident dose is below this limit. Static SIMS is referred to the technique utilizing a primary beam with a dose below the static limit and only analyzes the first monolayer of the sample. Static SIMS realizes a true surface analysis technique with an excellent sensitivity and the ability of resolving the chemical composition of the sample.[151]

Compared to static SIMS, dynamic SIMS is referred to the former technique utilizing a primary beam with a dose above the static limit which analyzes and removes the surface of the sample at the same time. Due to the higher sputtering rate of dynamic SIMS, it has a detection limit of ppb which is better than static SIMS. In addition, the spectra collected at different time could be interpreted as a function of depth in dynamic SIMS, resulting in a depth profile inherently. However, the high sputter rate also make it challenging to image using dynamic SIMS.

2.2.5 Uses of SIMS

Typically, data come in three formats for SIMS, i.e. mass spectra, spatial distributions of any signal of interest and depth profiles.[139]

doi:10.6342/NTU202303887

Due to its ability to detect all elements on the periodic table and differentiate between different isotopes of an element, as well as its high sensitivity, SIMS spectra have proven to be highly valuable in a range of fields, including material science,[152] biology,[153] and particularly geology,[154] where the ability to detect trace elements and differentiate between isotopes is crucial. In the study conducted by A. Kennedy, SIMS spectra provided information on the ratios between two sulfur isotopes, ^{33}S and ^{34}S, in apatite samples, which can be used to infer information about various geological events, such as magma crystallization, metamorphic processes, and the history of fluids and volatiles in terrestrial and extra-terrestrial environments. This finding demonstrate the usefulness of SIMS in providing valuable information especially for geological research.[154]

In addition to its ability to detect and differentiate between isotopes and elements, SIMS is also capable of providing spatial distributions of any signal of interest with a relatively high spatial resolution (up to 50 nm at optimized parameters) and a high sensitivity compared to most other mass spectrometry imaging methods. This capability makes it highly valuable for imaging a wide range of materials, particularly when label-free atomic or molecular signal imaging is required.[155] In a study conducted by M. Passarelli et al., SIMS was used to image the distribution of three neurotransmitters - gamma-aminobutyric acid (GABA), dopamine, and serotonin - in a mouse hippocampus and the images are shown in figure 2.23. By utilizing the high spatial resolution and the ability to detect label-free molecular signals of SIMS, this study demonstrated the potential for probing the effects of neuroactive substances on the functioning of the hippocampus. These findings illustrate the usefulness of SIMS in imaging and analyzing biological samples with high spatial resolution and sensitivity.[156]

doi:10.6342/NTU202303887

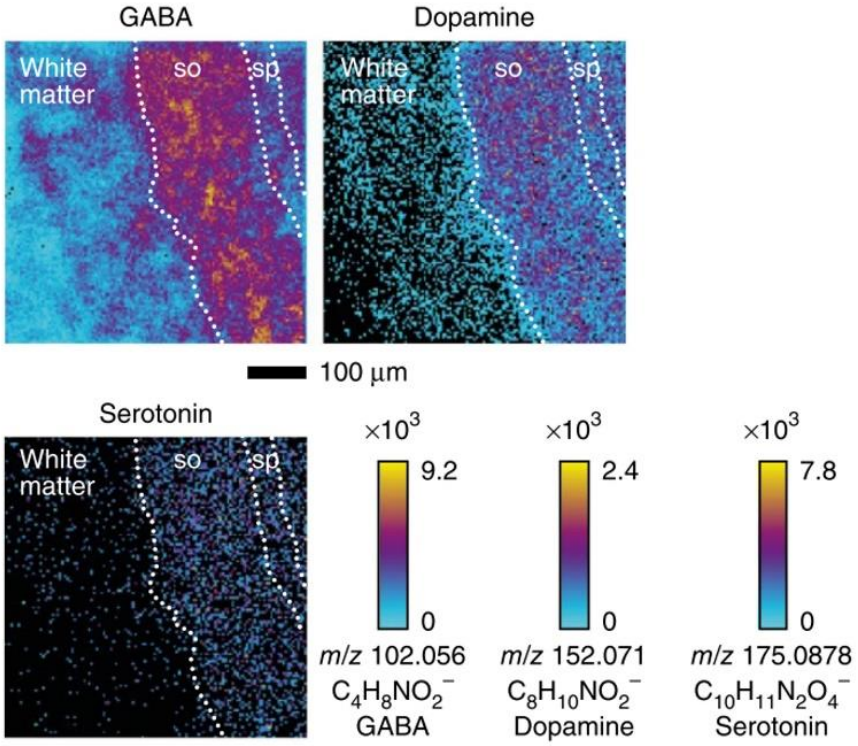

Figure 2.23 Mappings of GABA, dopamine, serotonin distribution in a mouse hippocampus.[156]

SIMS spectra can be collected at different sputtering times, which correspond to the composition information at a specific depth within the sample. Operating in this mode, SIMS can be used for depth profiling to illustrate the compositional changes along the depth of the sample. Figure 2.24 displays SIMS depth profiles of solid electrolyte interfaces (SEI) formed from $LiPF_6$-based carbonate electrolytes, with and without fluoroethylene carbonate (FEC). These profiles were used to analyze the effect of FEC on the formation of a SEI on the surface of the silicon anode of a lithium-ion electrode. The results demonstrate the capability of SIMS for in-depth analysis.[157]

doi:10.6342/NTU202303887

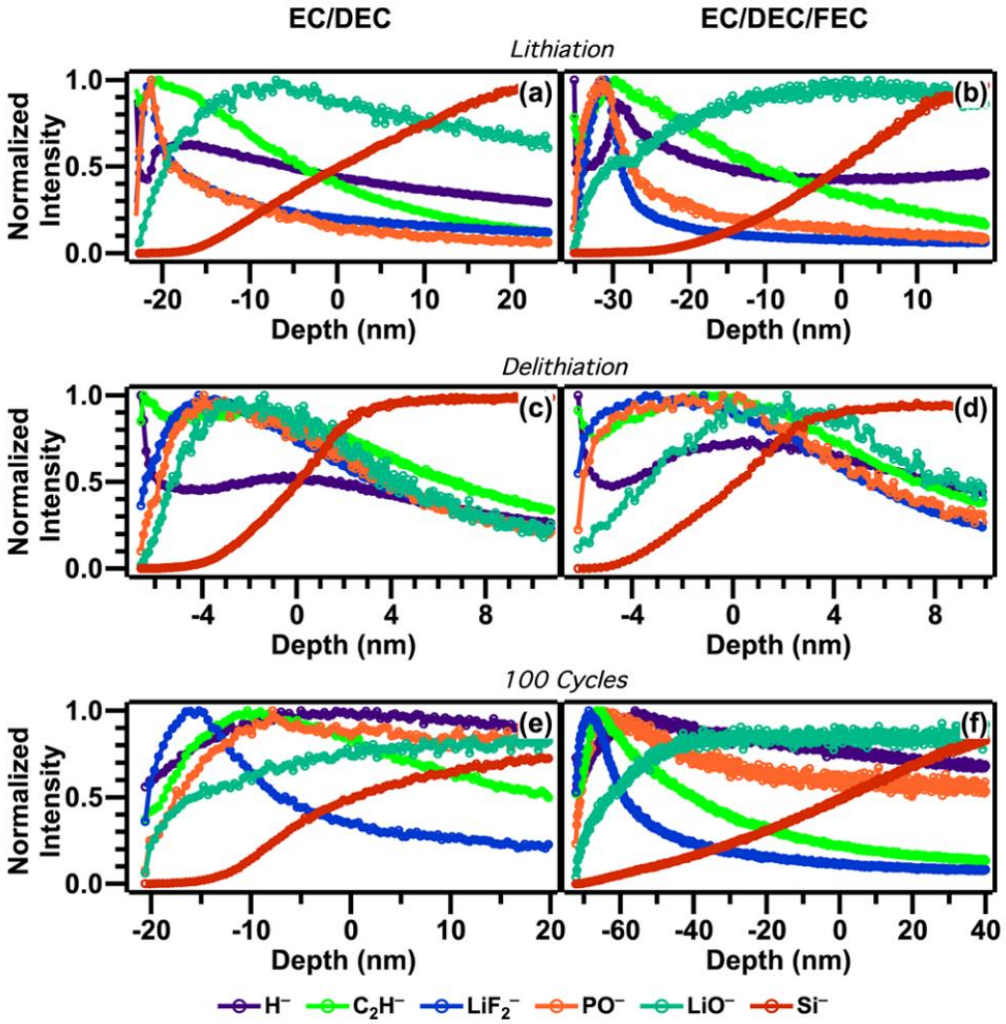

Figure 2.24 TOF-SIMS depth profiles of SEI formed from electrolytes consisting of ethylene carbonate (EC)/ diethyl carbonate (DEC) (left column) and EC/DEC/FEC (right column). The electrolytes underwent different treatments, including (a, b) galvanostatic lithiation, (c, d) one full cycle of galvanostatic lithiation and delithation, and (e, f) 100 galvanostatic cycles.[157]

doi:10.6342/NTU202303887

Chapter 3 Experimental and instruments

3.1 Materials

All the chemicals were used as obtained without further purification.

1,3,5-Benzenetricarboxylictrimesic acid (BTC) ($C_6H_3(CO_2H)_3$, 98%, Alfa Aeser, USA) and copper(II) nitrate trihydrate ($Cu(NO_3)_2 \cdot 3(H_2O)$, 77% as $Cu(NO_3)_2$, SHOWA, Japan) were used as the reactants for the synthesis of HKUST-1. Acetic acid (Glacial) (CH_3COOH, 99.7%, SHOWA, Japan) and triethylamine ($C_6H_{15}N$, 99%, Alfa Aeser, USA) were used as the modulator for the reaction.

2-Methylimidazole (2-mIm) ($C_4H_6N_2$, 99%, Acros Organics, Belgium) and zinc nitrate hexahydrate ($Zn(NO_3)_2 \cdot 6(H_2O)$, 99%, SHOWA, Japan) were used as the reactants for the synthesis of ZIF-8 nanoparticles and zinc acetate dihydrate ($Zn(CH_3COO)_2 \cdot 2(H_2O)$, 98%, Alfa Aeser, USA) was used instead of zinc nitrate hexahydrate in the cathodic deposition of ZIF-8 thin films. Cobalt(II) nitrate hexahydrate ($Co(NO_3)_2 \cdot 6(H_2O)$, 98%, SHOWA, Japan) was used instead of zinc acetate dihydrate in the synthesis of ZIF-67 and bimetallic ZIF thin films.

Acetaminophen ($C_8H_9NO_2$, 98%, Sigma-Aldrich, USA) and caffeine ($C_8H_{10}N_4O_2$, 98.5%, Acros Organics, Belgium) were used as the two model drugs in this research. 1-Butanol ($C_4H_{10}O$, 99%, Acros Organics, Belgium), ethanol (C_2H_5OH, 99.5%, ECHO, Taiwan), methanol (CH_3OH, 99.9%, AENCORE, Australia), N,N-dimethylformamide (DMF) (C_3H_7NO, 99.8%, Macron Fine Chemicals, USA), n-pentane (C_5H_{12}, 99%, Acros Organics, Belgium) and toluene ($C_6H_5CH_3$, 99.8%, ECHO, Taiwan) were used as the solvents in the drug loading processes.

doi:10.6342/NTU202303887

3.2 Instruments

3.2.1 Optical microscope (OM)

Optical microscope (OM) is a well-established technique that utilizes visible lights for observation of small objects. The design of OM is based on classical optics and is the oldest microscope. The OM images in this research were carried out by BX51 (Olympus, Japan).

3.2.2 Scanning electron microscope (SEM)

Scanning electron microscope (SEM) is a technique used to examine the surface morphology of a sample. It involves scanning the sample with an energetic electron beam. When the beam interacts with the sample, the sample is excited and various signals are emitted, including secondary electrons, backscattered electrons, and characteristic X-rays. In SEM, the detection usually focuses on secondary electrons, which have the lowest energy among the emitted electrons. Thus, only the secondary electrons emitted from the surface of the sample in a depth of 5-50 nm can be detected. The intensity contrast of these secondary electrons provides valuable information about the surface morphology of the sample. The characterization of the morphology and the microstructure of the synthesized MOFs were carried out by Nova 200 (FEI, USA) in this research.

3.2.3 X-ray diffractometer (XRD)

X-ray diffraction is a technique that utilize x-ray to analyze the crystal structure of materials. When x-ray enters a crystal and interacts with electrons of atoms in the crystal, elastic scattering occurs and each occurrence of elastic scattering produce a secondary spherical wave. These waves produced by elastic scattering could interfere constructively

doi:10.6342/NTU202303887

in some specific directions described by Bragg's law:

$$n\lambda = 2dsin\theta \qquad \text{Eq. 3.1}$$

where n is any integer indicating the order of diffraction; λ is the wavelength of the x-ray; d is the spacing between diffracting planes; and θ is the incident angle.

Because x-ray has a wavelength typically in the same order of spacing between planes in a crystal, it makes x-ray the ideal source for probing crystal structures. The crystal structures in this research were characterized by its X-ray diffraction (XRD) pattern obtained by the X-ray diffractometer Miniflex (Rigaku, Japan) which is worked at 40 kV and 15 mA utilizing CuKα radiation.

3.2.4 Time of flight secondary ion mass spectrometry (ToF-SIMS)

Secondary ion mass spectrometry (SIMS) is a powerful analytical technique used for surface characterization and depth profiling of materials. The working principle of SIMS could be described as employing a focused primary ion beam composed of high-energy ions in the range of 0.1—50 keV bombarding the surface of the target material. When the primary ion beam bombards the target material, energy is transferred to the surface atoms or molecules, leading to a collision cascade. If the energy exceeds the threshold displacement energy, atoms or molecules can be displaced from the surface, potentially becoming ions by gaining or losing one or more electrons. These ions, known as secondary ions, are then extracted and focused through an electrostatic lens system. They are subsequently directed into a mass spectrometer, where they are separated based on their m/z ratio for mass spectrometry analysis.

doi:10.6342/NTU202303887

SIMS analysis in this research was carried out by the PHI TRIFT V nanoTOF (ULVAC-PHI, Japan) using the dual-beam slice-and-view scheme. Each component of SIMS used in this research will be further described in the following sections.

3.2.4.1 Ion source

SIMS detects secondary ions produced by bombardment of primary ions and thus the generation of primary ions is one of the most important parts in SIMS. In this research, C_{60}^+ was the primary ion used for acquisition due to its ability to be pulsed (approximately 8200 Hz, 15 ns pulse length) in our instrument which is required for the ToF analyzer. In addition, a range of ion beams including Ar^+, C_{60}^+ and Ar_{2500}^+ was employed as the sputter beams.

In each acquisition phase, an acceleration voltage of 20 kV was applied to the C_{60}^+ beam and the current of C_{60}^+ was 0.15 nA-DC rastering across a 50 μm × 50 μm area with an incident angle of 42°, resultig in a current density of 0.74 nA/cm^2-DC. The acquisition time for each acquisition phase was 3 minutes between sputter phases and the ion dosage accumulated in 3 minutes was 1.02×10^8 ions/cm^2 which was below the static limit of 10^{12} ions/cm^2.

In sputter phases, different acceleration voltages and current densities were applied to different sputter ions. For C_{60}^+, the acceleration voltage was 20 kV with a direct current of 1 nA rastering across a 500 μm × 500 μm area, resulting in a current density of 400 nA/cm^2. The incident angle was 42°. For Ar^+, an acceleration of 1 kV was applied with a floating voltage of 0 V or 500 V, yielding beam energy of 1 keV and 500 eV respectively. The current of Ar^+ was 100 nA rastering across a 2000 μm × 2000 μm area with an incident angle of 45°, resulting in a current density of 500 nA/cm^2. For Ar_{2500}^+, four

doi:10.6342/NTU202303887

acceleration voltages, i.e. 5 V, 10 V, 15 V and 20 V, were applied to generate the Ar_{2500}^+ beam with respective beam energy. The current density was tuned for each Ar_{2500}^+ with different beam energy and the incident angle was 50°.

In this study, primary ions and sputter ions were generated using electron impact ionization, a well-established technique in mass spectrometry. Electron impact ionization (EI) involves the interaction of an energetic electron beam with the target particles in the vapor phase, which were Ar, C_{60}, and Ar_{2500} in this study. By heating a thin filament to induce thermionic emission, energetic electrons are emitted and accelerated to energies exceeding the ionization potential of the target particles. When the energetic electrons impact the target particles, the electrons excite the target particles and leads to their ionization, resulting in the generation of primary ions.[158]

Unlike Ar which exists in vapor phase naturally, C_{60} vapor was produced by heating to above 370 °C. Moreover, Ar_{2500} was produced by pressuring Ar (650 kPa provided by the manufacturer) through a nozzle into a vacuum chamber. When the Ar entered the vacuum chamber, adiabatic expansion occurred and the Ar condensed into cluster. Afterwards, these vapors could be ionized using EI and employed as the ion beams.

3.2.4.2 Mass analyzer

Mass analyzers separate the secondary ions by their m/z ratio to deduce information about the chemical structure of the analyte. In this research, a ToF analyzer was used. When the sample was bombarded by the pulsed C_{60}^+ beam, the secondary ions were accelerated by a 3 kV puled sample bias in positive ion mode (−3 kV in negative ion

doi:10.6342/NTU202303887

mode) into the ToF analyzer. The ToF analyzer separated ions with different m/z ratio by the time the ions traveling through a 2 m path. The velocity *v* of the secondary ions could be deduced by its kinetic energy and described as:

$$v = \sqrt{\frac{2qV}{m}} \qquad \text{Eq. 3.2}$$

where q is the charge of the secondary ion; V is the acceleration voltage; m is the mass of the secondary ion.

Thus, the time it takes for a secondary ion to travel to the detector could be described as :

$$t = \frac{L}{v} = L\sqrt{\frac{m}{2qV}} \qquad \text{Eq. 3.3}$$

where L is the length a secondary ion traveling. Since L and V were constant in this research, the $\frac{m}{q}$ could be deduced from t.[158]

In addition, a dual microchannel plate (DMCP) detector was employed in this research. The DMCP operates on the principle of secondary electron emission, where an array of microchannels coated with low work function materials is utilized. When a secondary ion enters the DMCP, it undergoes collisions with the microchannel walls, resulting in the emission of secondary electrons. Each emitted secondary electron then undergoes further collisions, leading to the generation of additional secondary electrons. Due to the design of the DMCP with two arrays of microchannels with different

doi:10.6342/NTU202303887

orientation, a secondary ion is guaranteed to collide with the detector. 50 % of the ions could be detected because only 50 % of the area is opened. At the end, the DMCP detector detects the amplified signal of electron current.

3.3 Experimental procedure

3.3.1 Substrate preparation

ITO glass (SCIKET, Taiwan) was used in all thin film fabrication in this work. It was cut into 2 sizes, i.e. 3 cm × 4 cm for cathodic deposition and 2 cm × 2 cm for spin coating. All ITO glass was cleaned by sonication subsequently in DI water, acetone and ethanol for 10 minutes each and finally dried with N_2 flow. The process is illustrated in figure 3.1.

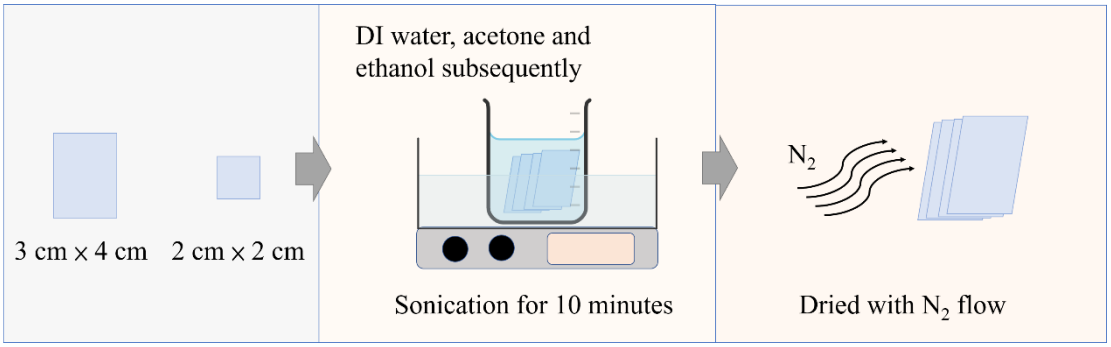

Figure 3.1 Scheme of substrate preparation.

3.3.2 MOF preparation

In this work, two different types of MOFs were prepared, i.e. HKUST-1 (Hong Kong University of Science and Technology) and ZIF-8 (zeolitic imidazolate framework), to assess the capabilities of ToF-SIMS analysis and depth profile across different MOF materials. Moreover, each type of MOF was prepared by two different procedures to

doi:10.6342/NTU202303887

generate materials with different morphologies for analytical utilities.

3.3.2.1 HKUST-1 preparation

HKUST-1 with two different morphologies were prepared for different purposes. Namely, large HKUST-1 crystals were prepared for analysis of drug loading since it had been stated that large MOF crystals benefit research of diffusion in MOFs due to the elimination of influences from crystal interfaces and inter-particle diffusion.[67] The other one is HKUST-1 thin film prepared by spin coating in order to determine the sputtering parameters because the dimension of the large HKUST-1 crystals is too large for the sputtering sources used in this work.

3.3.2.1.1 Synthesis of large HKUST-1 crystals

Large HKUST-1 crystals were synthesized adapting the method reported by T. Tover et al.[11] by heating a solution of 490 mg of $Cu(NO_3)_2 \cdot 3H_2O$ and 240 mg of BTC in 3 ml of DI water, 3 ml of ethanol, 3ml of DMF and 12 ml of acetic acid at 55 °C for 3 days. After 3 days, sapphire blue crystals with cubic shape were observable by naked eyes in an abundant amount. The crystals were then rinsed with ethanol to remove the residual solvent and unreacted reactant. The process is depicted in figure 3.2. The obtained HKUST-1 crystals were stored in ethanol for further utilization.

doi:10.6342/NTU202303887

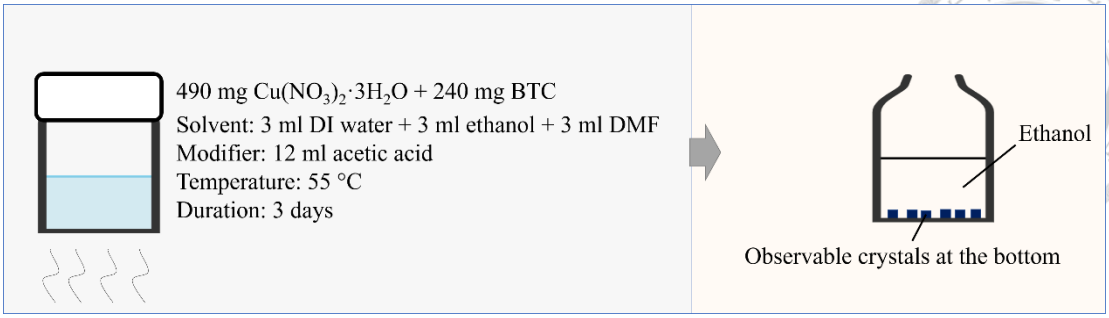

Figure 3.2 Scheme of the synthesis of large HKUST-1 crystals.

3.3.2.1.2 Spin-coating of HKUST-1 thin films

HKUST-1 thin films were prepared by first preparing HKUST-1 nanoparticles adapting the method reported by X. Mu et al.[12] 144.96 mg of $Cu(NO_3)_2 \cdot 3H_2O$ was dissolved in 5 ml of DI water to prepare solution 1 while 84.04 mg of BTC and 166.91 µl of triethylamine (TEA) were dissolved in 5 ml of ethanol to prepare solution 2. Both solution 1 and solution 2 were sonicated for 10 minutes to dissolve the solutes and clear solutions could be obtained. The two solutions were mixed at 85 °C under stirring and then stayed at heating and stirring for 3 hours. The HKUST-1 nanoparticles were collected using centrifugation at 9000 rpm for 15 minutes and rinsed with methanol to remove the residual solvent and unreacted reactant. The rinsing process was conducted for 3 times. The obtained HKUST-1 nanoparticles were dispersed in 12 ml of ethanol to form the colloid which would be used to fabricate HKUST-1 thin films by spin coating. The spin coating was performed by dropping 100 µl of the colloid onto a piece of cleaned 2 cm × 2 cm ITO glass at a spin rate of 1000 rpm for a minute. Spin coating was repeated for 5 times to obtain a uniform HKUST-1 thin film with a good coverage. The process is depicted in figure 3.3.

doi:10.6342/NTU202303887

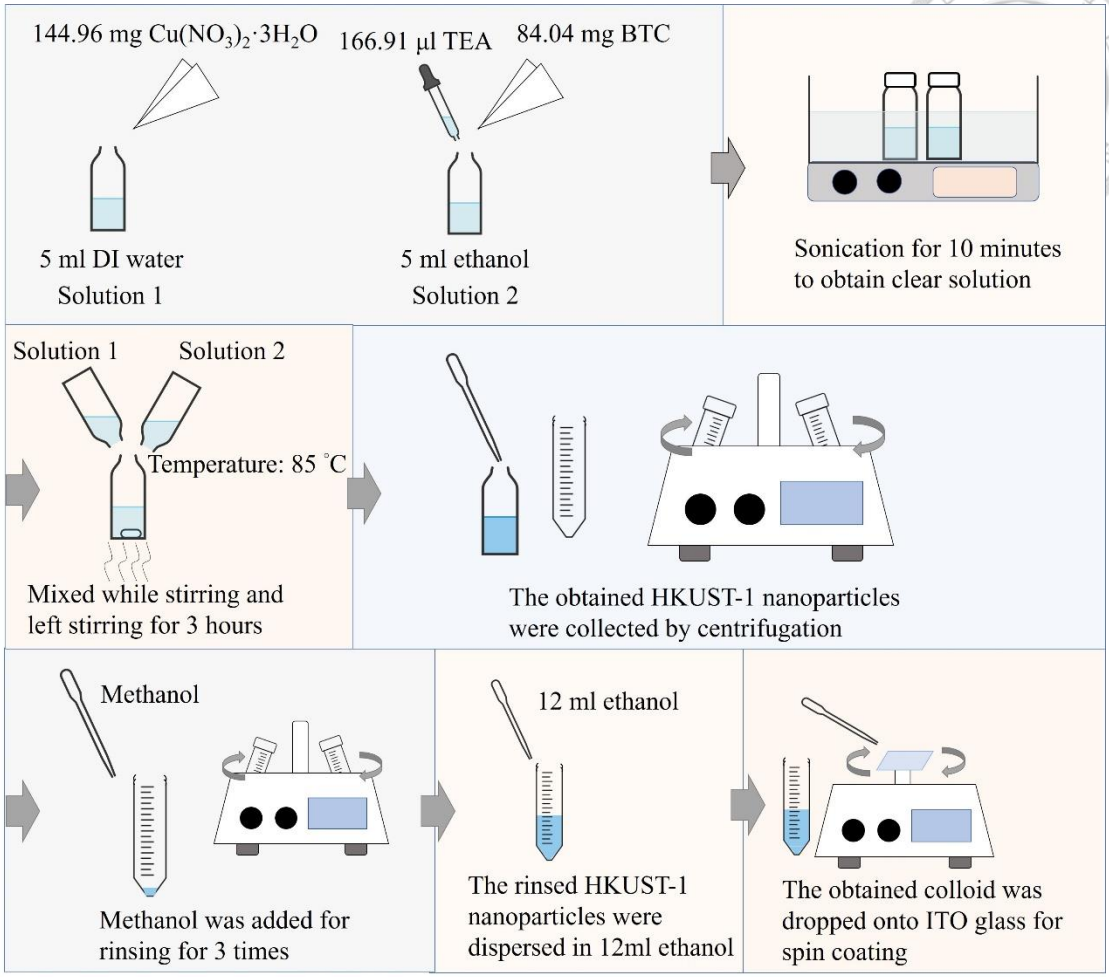

Figure 3.3 Scheme of HKUST-1 thin film prepared by spin coating.

3.3.2.2 ZIF-8 preparation

Two different methods were employed to fabricate ZIF-8 thin films with distinct morphology. One is spin coating and the other is cathodic deposition.

3.3.2.2.1 Spin coating of ZIF-8 thin film

In order to obtain a ZIF-8 thin film by spin-coating, ZIF-8 nanoparticles were synthesized first. The ZIF-8 nanoparticles were synthesized adapting from the process

doi:10.6342/NTU202303887

reported by N. Liédana et al.[13] Briefly, 190 mg of $Zn(NO_3)_2 \cdot 6H_2O$ and 2 ml of DI water was dissolved in 4 ml of methanol to form solution 3 and 618 mg of 2-mIm was dissolved in 4 ml of methanol to form solution 4. Both solution 3 and solution 4 were sonicated for 10 minutes to dissolve the solutes and clear solutions could be obtained. Then solution 1 and solution 2 were mixed in a 20 ml vial and kept at ambient temperature under stirring for two hours before ZIF-8 nanoparticles were formed and the solution turned into milky colloid. The synthesized ZIF-8 nanoparticles were collected by centrifugation at 9000 rpm for 10 minutes. Subsequently, 10 ml of methanol was added into the collected ZIF-8 nanoparticles for removing any residual reactant and the ZIF-8 nanoparticles were collected by centrifugation again. The rinsing process was performed for 3 times and the obtained ZIF-8 nanoparticles were dispersed in 2 ml of ethanol to form the colloid which would be then used for spin coating.

The spin coating was performed by dropping 100 μl of the colloid described above onto a piece of cleaned 2 cm × 2 cm ITO glass at a spin rate of 3000 rpm for a minute. The spin coating process was repeated for 5 times to obtain a ZIF-8 thin film with a uniform surface and a good coverage. The obtained ZIF-8 thin film would be denoted as ZIF-8_spin in the following discussion to differentiate it from ZIF-8 thin film prepared by cathodic deposition method. The process is illustrated in figure 3.4. The spin coating was carried out by the spin coater produced by Olink, Taiwan.

doi:10.6342/NTU202303887

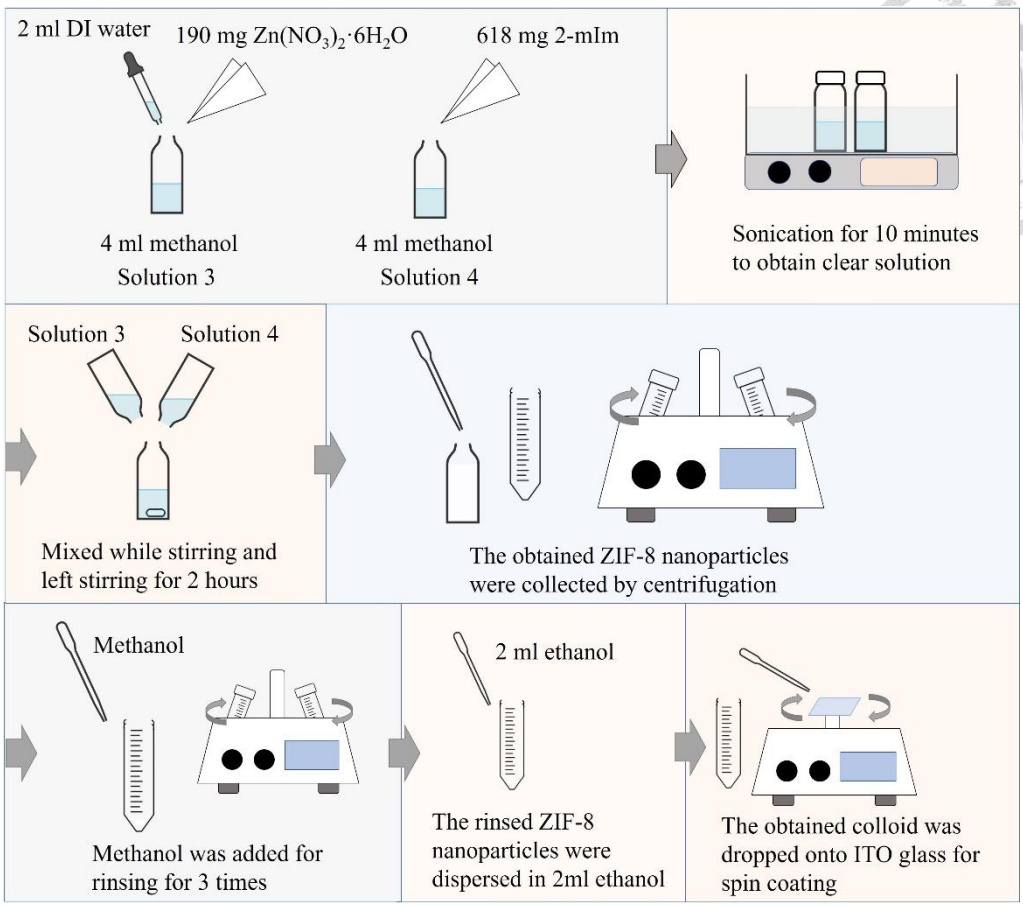

Figure 3.4 Scheme of ZIF-8 thin film prepared by spin coating.

3.3.2.2.2 Cathodic deposition of ZIF-8 thin film

Adapted from the method reported by R. Wei et al.,[14] 50 ml of 1 M 2-mIm aqueous solution and 10 ml of 0.083 M $Zn(CH_3COO)_2 \cdot 2H_2O$ aqueous solution were mixed in a 100 ml beaker and stirred for 10 seconds to form the precursor solution for cathodic deposition of a ZIF-8 thin film. A piece of cleaned 3 cm × 4 cm ITO glass was employed as the working electrode and a piece of Pt foil which worked as the counter electrode were hung with a separation of 1.5 cm. After the electrodes were immersed in the precursor, a voltage of −1.5 V was applied to the ITO glass for 80 minutes before the ITO

doi:10.6342/NTU202303887

glass was lifted from the electrolyte. The setup of the electrolytic cell is depicted in figure 3.5. A uniform and well-intergrown ZIF-8 thin film could be obtained on the surface of the ITO glass and was rinsed with DI water and dried with N_2. ZIF-8 thin film prepared by the cathodic deposition process described above was denoted as ZIF-8_elec in the following discussion due to the electrochemical nature of this process. The cathodic deposition was carried out by the programmable DC power supply PPS-1022 (MOTECH, Taiwan).

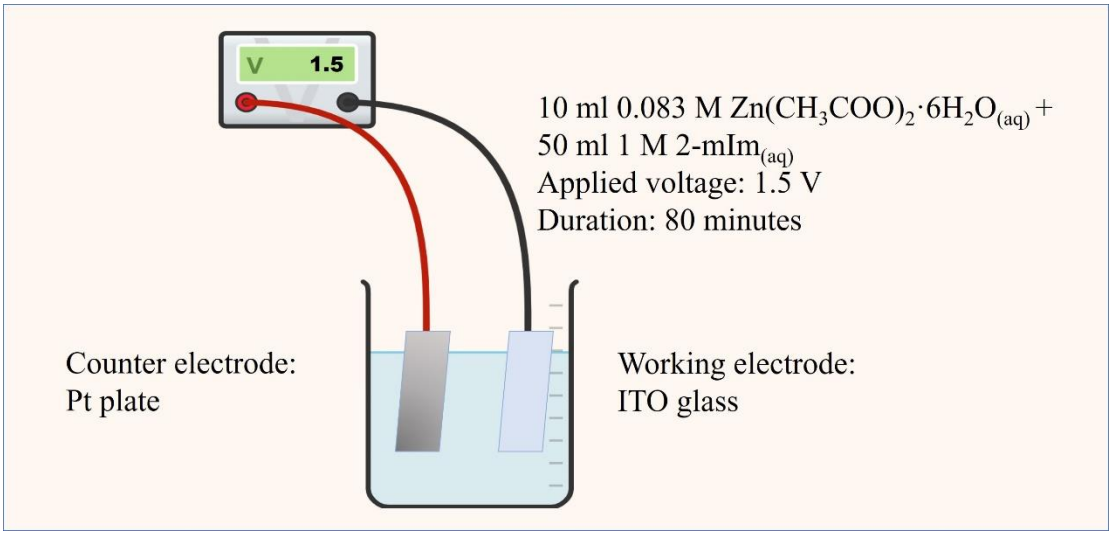

Figure 3.5 The setup of the electrolytic cell used for ZIF-8 cathodic deposition.

3.3.2.2.3 Cathodic deposition of bimetallic ZIF thin film

Bimetallic ZIF thin films were also prepared by the same cathodic deposition method except that $Co(NO_3)_2 \cdot 6(H_2O)$ was added into the $Zn(CH_3COO)_2 \cdot 2H_2O$ aqueous solution to adjust the molar ratio of Zn^{2+} : Co^{2+} to be 1:1 or 9:1 while the total molarity of metal ions in the solutions was maintained at 0.083 M.

doi:10.6342/NTU202303887

Chapter 4 Results and discussion

4.1 Materials characterization

4.1.1 Materials characterization of HKUST-1

Figure 4.1 shows the (a) SEM and (b) OM images of a synthesized large HKUST-1 crystal. The HKUST-1 crystal showed a cubic structure with a dimension of about 600 μm, indicating the seamless crystal growth along (100) direction. It indicted that large HKUST-1 crystals were prepared with a well-defined crystal structure.

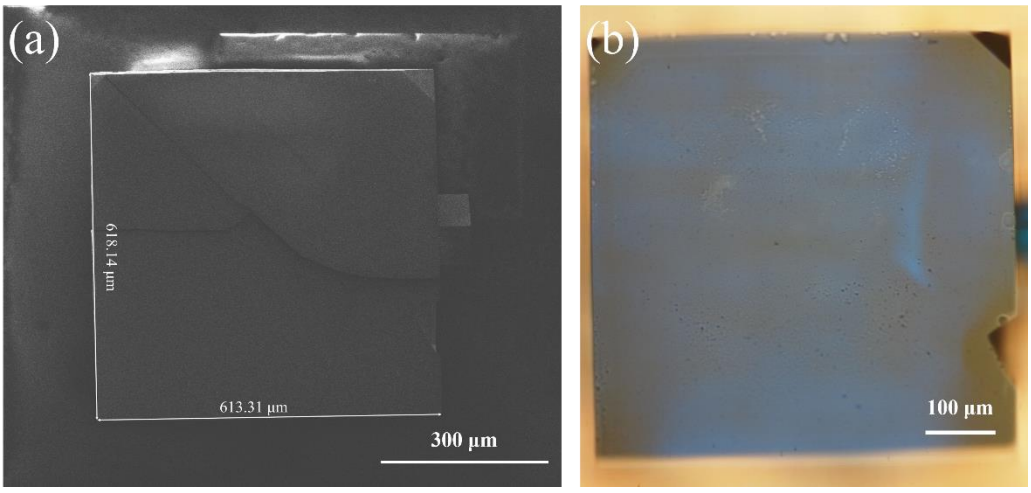

Figure 4.1 (a) SEM and (b) OM images of the synthesized large HKUST-1 single crystal.

On the other hand, HKUST-1 thin films were fabricated by spin coating utilizing the synthesized HKUST-1 nanoparticles and the morphology of the HKUST-1 thin film was characterized by SEM. Figure 4.2 (a) shows the top-view SEM image of the HKUST-1 thin film while figure 4.2 (b) shows the cross-section SEM image of the HKUST-1 thin film, indicating a uniform but porous thin film with a thickness of 805 ± 52 nm.

doi:10.6342/NTU202303887

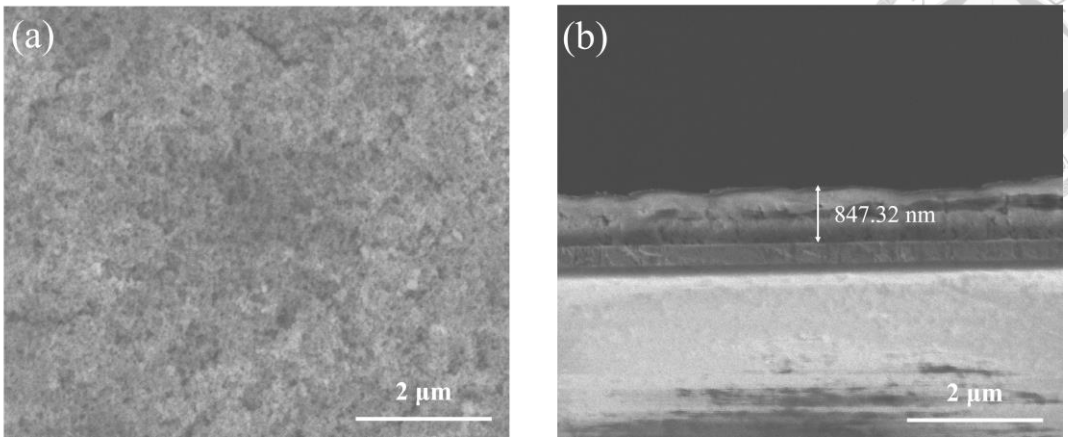

Figure 4.2 (a) Top-view and (b) cross-section SEM images of HKUST-1 thin film.

For crystal structure analysis, large HKUST-1 crystals were grinded into powder for powder X-ray diffraction (PXRD) while the HKUST-1 thin film was characterized by XRD as-prepared. Figure 4.3 shows the XRD patterns of (a) grinded large HKUST-1 crystals and (b) the HKUST-1 thin film and both match the pattern simulated according to the lattice constant of HKUST-1 reported before,[159] confirming that HKUST-1 was successfully prepared with different morphologies. Nonetheless, large HKUST-1 crystals show undoubtedly higher crystallinity while the HKUST-1 thin film shows not only a high background but also a prominent peak of ITO substrate.

Therefore, large HKUST-1 crystals appear to be a more promising material for analyzing diffusion in HKUST-1 because of the more uniform surface and higher crystallinity. Nonetheless, the HKUST-1 thin films were still used in experiments when a thinner thickness was required.

doi:10.6342/NTU202303887

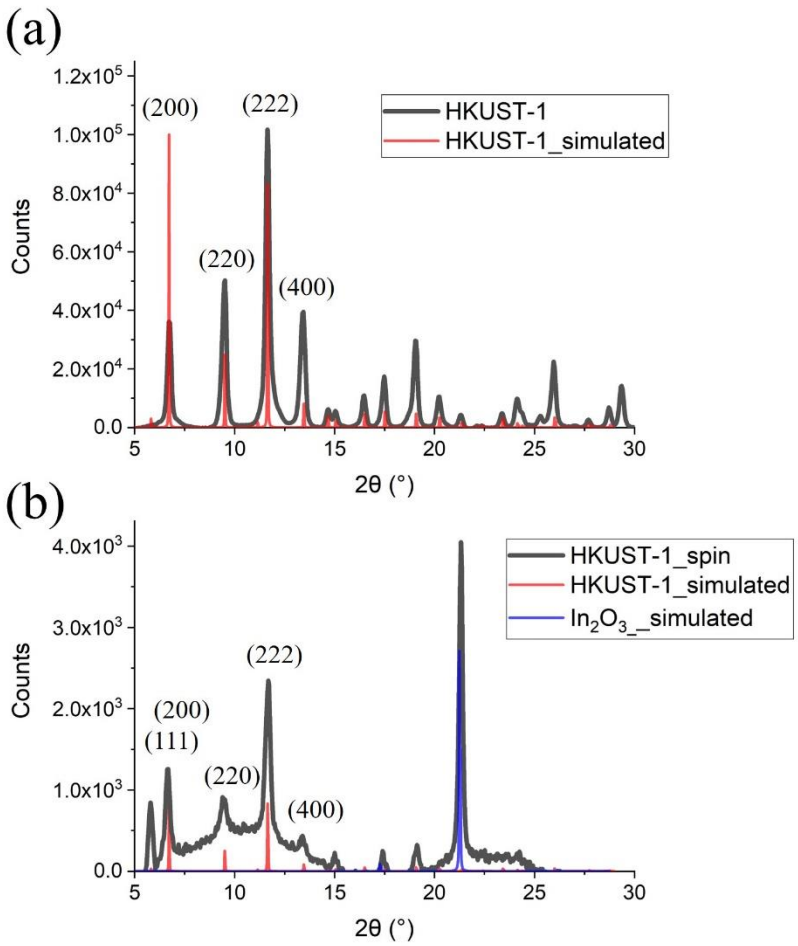

Figure 4.3 XRD patterns of (a) grinded large HKUST-1 crystals and (b) the HKUST-1 thin film.

4.1.2 Materials characterization of ZIF-8 thin film

Figure 4.4 (a) shows the SEM image of ZIF-8 thin film prepared by spin coating once exhibiting a poor coverage with exposed ITO substrate. In order to prepare a uniform ZIF-8 thin film with a good coverage, the spin coating process was repeated for 5 times and a uniform and evenly deposited surface could be seen in figure 4.4 (b). Therefore, ZIF-8 thin films prepared by spin coating repeated for 5 times were employed for further

doi:10.6342/NTU202303887

analysis and denoted as ZIF-8_spin in the following discussion. In addition, figure 4.5 shows the cross-section SEM image of ZIF-8_spin exhibiting a uniform and compact thin film of ZIF-8 nanoparticles with a thickness of 1045 ± 83 nm.

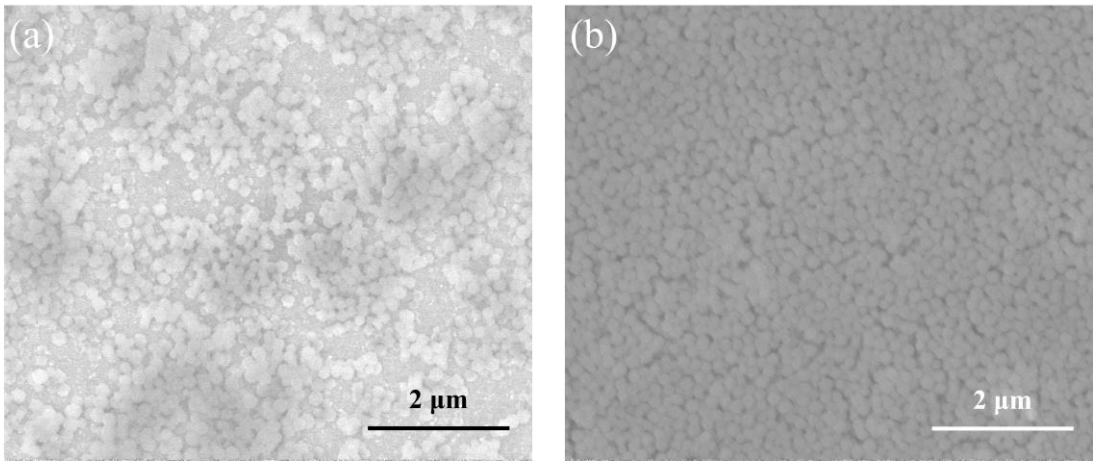

Figure 4.4 Top-view SEM images of ZIF-8 thin films prepared by spin coating (a) once and (b) repeated for 5 times.

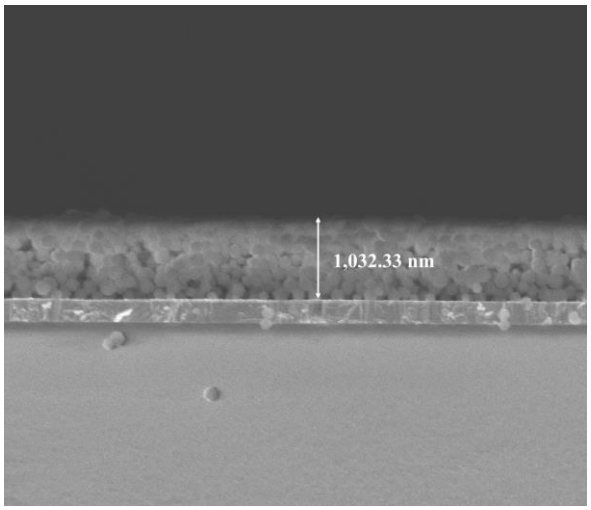

Figure 4.5 Cross-section SEM image of ZIF-8_spin.

Similarly, the morphology of ZIF-8_elec was investigated by SEM. Figure 4.6 (a)

doi:10.6342/NTU202303887

shows the top-view SEM image of ZIF-8_elec which exhibits a uniform surface with well intergrown crystals showing no spacing between them and figure 4.6(b) shows the cross-section SEM image of ZIF-8_elec which exhibits a uniform thin film without any crack with a thickness of 636 ± 60 nm. Unlike ZIF-8_spin where spacing between nanoparticles are visible under SEM images, ZIF-8_elec appears to be a more suitable material for analyzing diffusion in ZIF-8 because facet of the ZIF-8 crystals under the top surface are not exposed in ZIF-8_elec.

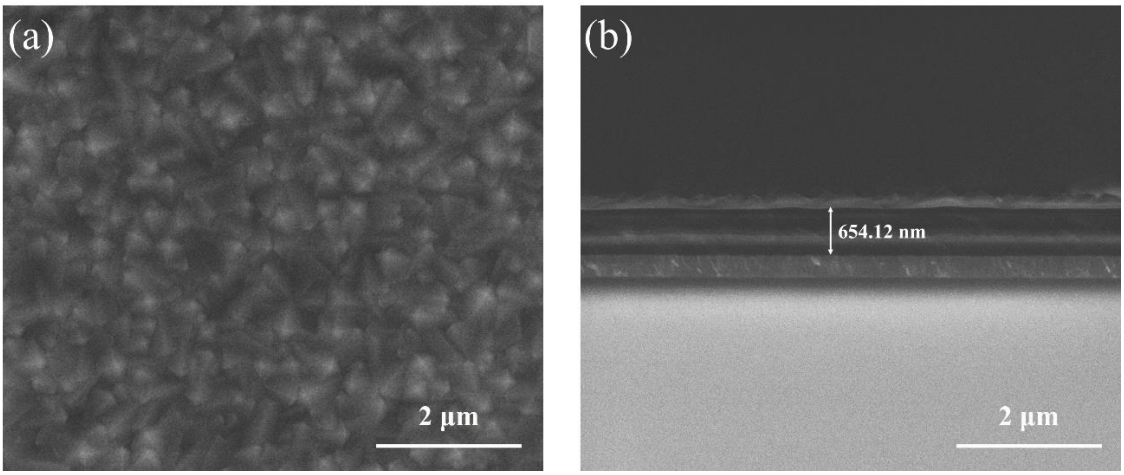

Figure 4.6 (a) Top-view and (b) cross-section SEM images of ZIF-8_elec

Both ZIF-8_spin and ZIF-8_elec were further characterized by XRD for structure characterization. Figure 4.7 shows the XRD pattern of (a) ZIF-8_spin and (b) ZIF-8_elec which both exhibit sodalite structure with a lattice constant that perfectly matches the pattern simulated according to the reported lattice constant of ZIF-8,[160] confirming the structures of the obtained materials. Besides, both thin films show sharp peaks implying that well-crystalized structures were grown in both cases. Nonetheless, ZIF-8_spin shows a peak that comes from ITO glass which suggests that ITO substrate was more exposed

doi:10.6342/NTU202303887

in ZIF-8_spin than that in ZIF-8_elec, adding another support which favors ZIF-8_elec over ZIF-8_spin other than SEM images.

Despite SEM images and XRD patterns both point out that ZIF-8_spin and ZIF-8_elec both possess uniform surfaces and highly crystalline structures, ZIF-8_elec is more favorable for analyzing diffusion of guest molecules in ZIF-8 due to the absence of spacing between nanoparticles and a better coverage. Therefore, ZIF-8_elec will be used in further analysis if no special indication is made.

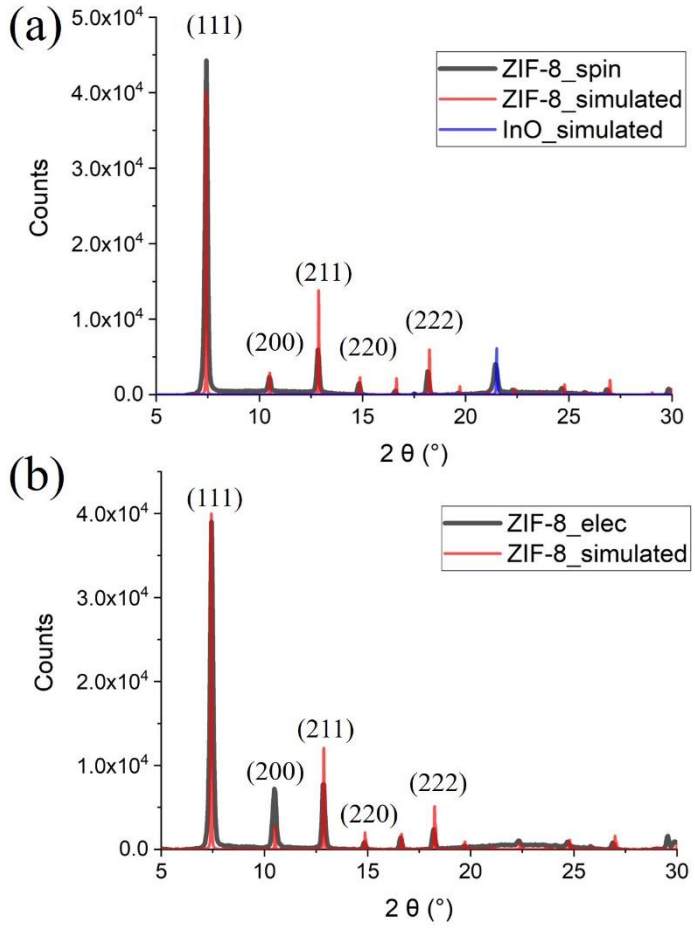

Figure 4.7 XRD patterns of (a) ZIF-8_spin and (b) ZIF-8_elec.

doi:10.6342/NTU202303887

4.2 Degradation of ZIF-8_elec in different solvent

We aim to assess the diffusion of model drugs into a ZIF-8 thin film. Therefore, a solvent which could not only dissolve the model drugs we have selected but also have no impact on the structure of a ZIF-8 thin film is desired. Figure 4.8 shows the SEM images of (a) ZIF-8_elec and ZIF-8_elec after being immersed in a range of common solvents including (b) DI water, (c) methanol, (d) ethanol, (e) DMF, (f) toluene and (g) pentane for 48 hours. Apparent degradation could be seen in the ZIF-8_elec immersed in water for 48 hours which shows deformed crystals and exposed ITO substrate. ZIF-8_elec immersed in methanol for 48 hours also shows degradation although in a less significant manner where deformed crystals and voids on the thin film could be seen. Nonetheless, there is no indication of degradation of ZIF-8_elec could be seen in the SEM images after being immersed in the other four solvents for 48 hours.

It could be explained by the degradation mechanism of ZIF-8 that has been reported to be due to the formation of a ligand vacancy and a protonated 2-mIm by acid-induced Zn-N cleavage. A Brønsted acid (HX) could donate a proton to an imidazolate linker and the conjugated base (X^-) could bond to the Zn^{2+}, forming a dangling linker which could further evolve into a ligand vacancy if protonated by another Brønsted acid.[161,162] Among the 6 solvents used, DI water, methanol, and ethanol are protic solvents and their pK_a is 14.0, 15.3 and 15.9 respectively, while the other 3 solvents are aprotic solvents.[163] Since pK_a indicates the tendency of a solvent to deprotonate, a solvent with a lower pK_a shows a higher tendency to protonate 2-mIm in ZIF-8 crystals which causes the ultimate degradation of ZIF-8 crystals. DI water has the lowest pK_a among the 6 solvents used in this experiment so it could explain the reason why ZIF-8_elec suffers the most significant

doi:10.6342/NTU202303887

degradation after being immersed in DI water. In addition, CO_2 dissolved in DI water (H_2CO_3, $pK_a = 3.49$)[164] also release more proton into the solution, making DI water even more destructive for ZIF-8. ZIF-8_elec suffers less significant degradation in methanol which has a higher pK_a than DI water, and shows no indication of degradation in ethanol which has the highest pK_a among the protic solvents used in this experiment. ZIF-8_elec also shows no indication of degradation in the 3 aprotic solvents because 2-mIm in ZIF-8 structure would not be protonated in aprotic solvents, which also supports this explanation.

However, most aprotic solvents are non-polar solvents including toluene, pentane, etc. These non-polar aprotic solvents struggle to dissolve common drugs like acetaminophen, so DMF stands out as a polar aprotic solvent. DMF not only shows little alternation to ZIF-8 thin films but also shows decent solubilities toward acetaminophen and caffeine which are the two model drugs selected in this research. Therefore, the drug loading experiments were conducted using ethanol or DMF as the solvent if no further indication was made.

doi:10.6342/NTU202303887

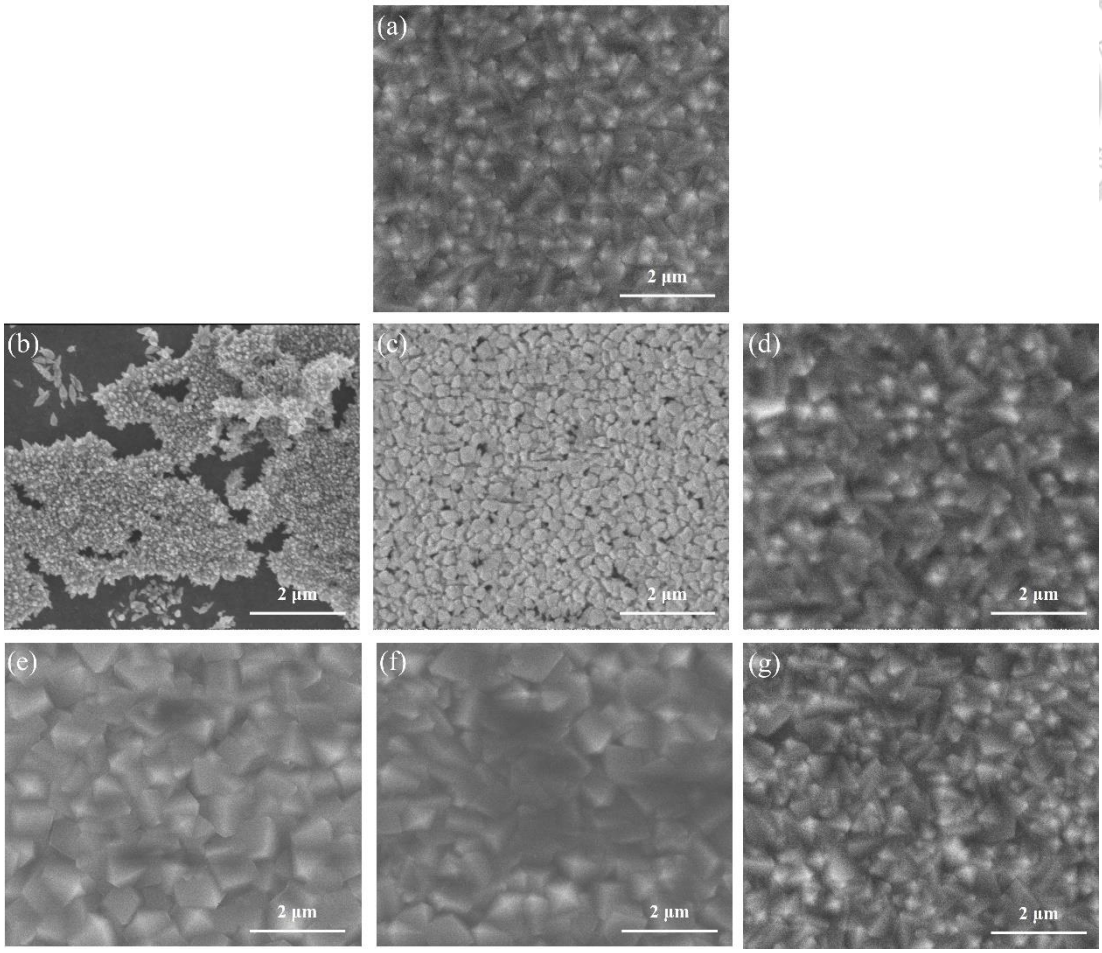

Figure 4.8 SEM images of (a) as prepared ZIF-8_elec and after immersed in (b) DI water, (c) methanol, (d) ethanol, (e) DMF, (f) toluene and (g) pentane for 48 hours.

4.3 ToF-SIMS analysis of HKUST-1

HKUST-1 is a MOF material composed of copper(II) ions bridged by BTC, forming a metal carboxylate paddle wheel [$Cu_2C_4O_{10}$] as the node and BTC as the linker in this structure. The structure of HKUST-1 is illustrated in figure 4.9.In order to genuinely present the metal-organic mixture structure of HKUST-1 in a depth profile, it is necessary to determine the characteristic peaks that could represent the metallic nodes and the

doi:10.6342/NTU202303887

organic linker respectively first.

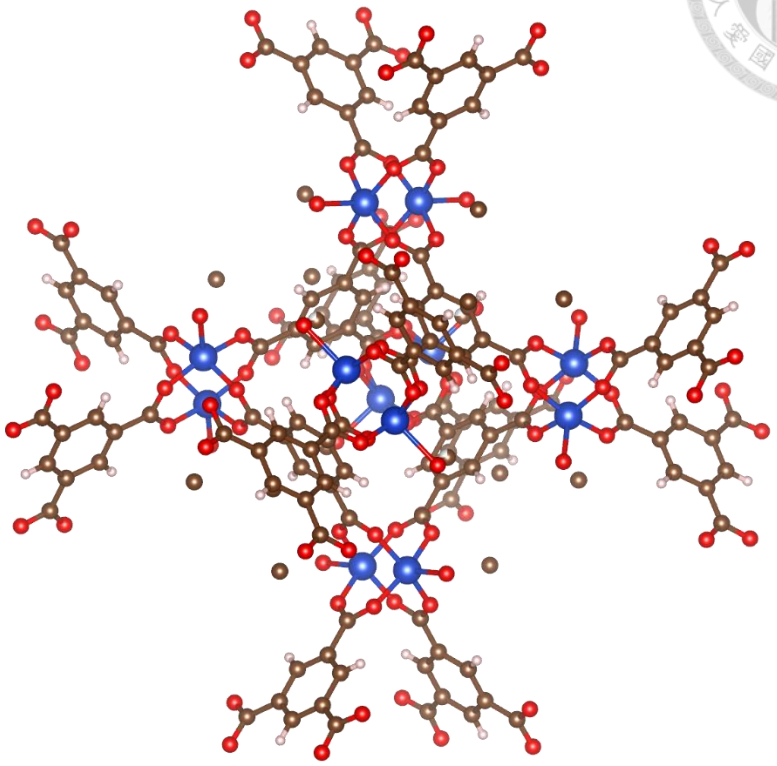

Figure 4.9 Structure of HKUST-1. (Cu(II): blue; O: red; C: brown; H: pink)[159]

4.3.1 Determination of the characteristic peaks of HKUST-1

Figure 4.10 shows the mass spectrum of a HKUST-1 single crystal collected under negative ion mode. Most of the peaks are hydrocarbons that come from C_{60} and have little information about the HKUST-1. Moreover, characteristic peak that could represent the Cu containing metal carboxylate nodes in HKUST-1 structure was not found in this mass spectrum. The naturally occurred Cu on earth has two isotopes, ^{63}Cu and ^{65}Cu, with the abundance of 69.17 % and 30.83 % respectively. There is not any pair of peaks with the ratio of naturally occurred isotopes of Cu could be found in figure 4.10. In brief, both

doi:10.6342/NTU202303887

characteristic peaks that could represent the metallic nodes and the organic linkers in HKUST-1 are hardly recognized in the mass spectrum collected under negative ion mode.

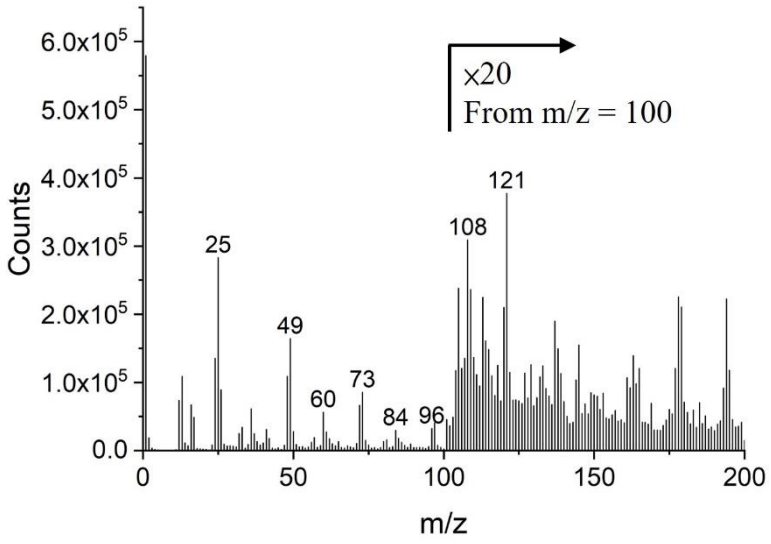

Figure 4.10 Mass spectrum of HKUST-1 collected under negative ion mode.

Therefore, a mass spectrum of a HKUST-1 single crystal was collected under positive ion mode and is shown in figure 4.11 (a) in hope of that the characteristic peaks could be identified in positive ions. A prominent peak at m/z = 63 could be easily observed and a peak at m/z = 65 appears to have the intensity near the abundance of the naturally occurred ^{65}Cu. The slight excess of the intensity of the peak at m/z = 65 than predicted by considering the naturally occurred isotopes of Cu is due to other organic fragments which also have m/z = 65. It is proven by figure 4.11 (b) where a mass spectrum collected after the HKUST-1 was sputtered by 10kV Ar_{2500} is shown, demonstrating that the ratio between peaks at m/z = 63 and 65 matches the ratio of naturally occurred isotopes of Cu accurately after most of the organic signals have been removed.

doi:10.6342/NTU202303887

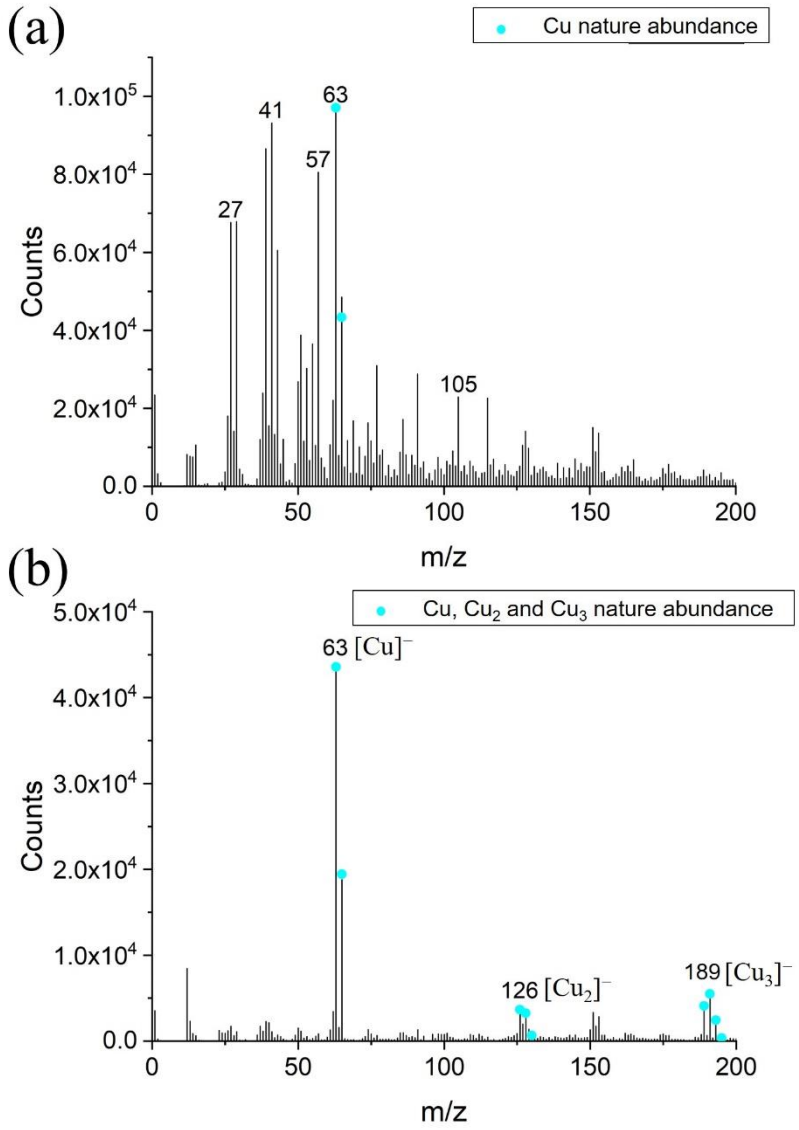

Figure 4.11 Mass spectra of (a) HKUST-1 and (b) HKUST-1 after being sputtered collected under positive ion mode.

In addition, a characteristic peak that could represent the organic linkers in HKUST-1 is also necessary to be determined in the mass spectrum collected under positive ion mode. The peak at m/z = 105 is shown in figure 4.12 (a) with an exact mass larger than

doi:10.6342/NTU202303887

an integral which suggest that this peak might correspond to an organic molecule. In addition, the exact mass also matches the exact mass of $[C_7H_5O]^+$ (105.034 Da) well which is a reasonable fragment from BTC. MS2 was also collected for the peak at m/z = 105 to determine its structure and is shown in figure 4.12 (b). The MS2 shows a series of losses of hydrocarbons following the loss of an oxygen which further suggests that the peak at m/z = 105 corresponds to $[C_7H_5O]^+$. The result of MS2 is also arranged in table 4.1 which clearly summarizes the fragmentation of $[C_7H_5O]^+$ in MS2.

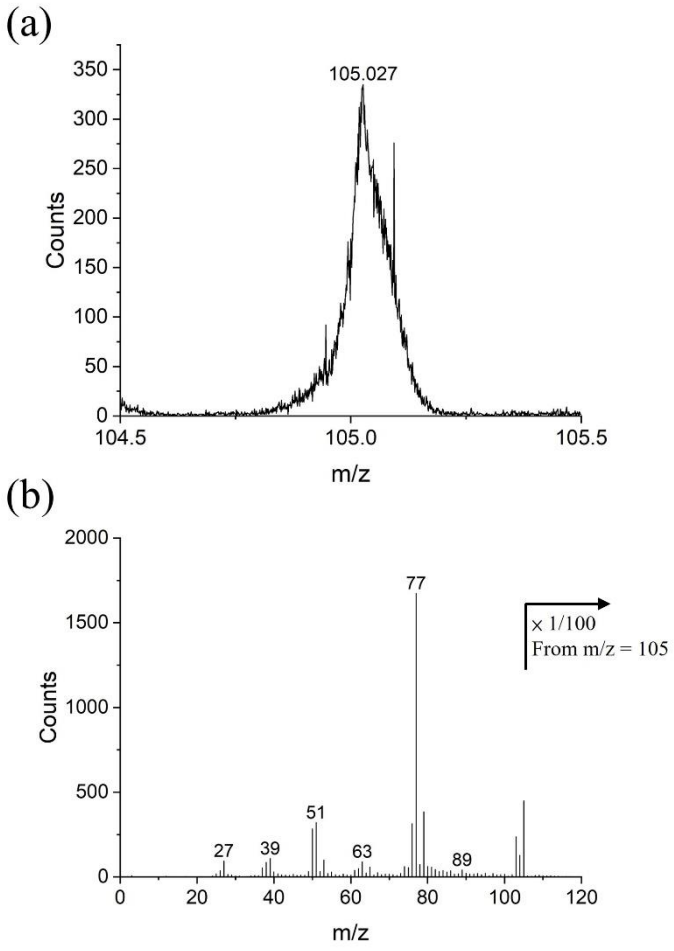

Figure 4.12 Mass spectra of (a) the peak at m/z = 105 and (b) MS2 of the peak at m/z = 105.

doi:10.6342/NTU202303887

Table 4.1 The fragmentation of MS2 of the peak at m/z = 105.

m/z of the fragment (lose from the original fragment)	Chemical structure of the fragment (lost fragment)
105(−0)	$[C_7H_5O]^+$ ($[P]^+$)
89(−16)	$[C_7H_5]^+$ ($[P - O]^+$)
77(−28)	$[C_6H_5]^+$ ($[P - CO]^+$)
63(−42)	$[C_5H_3]^+$ ($[P - C_2H_2O]^+$)
51(−54)	$[C_4H_3]^+$ ($[P - C_3H_2O]^+$)
39(−66)	$[C_3H_3]^+$ ($[P - C_4H_2O]^+$)
27(−78)	$[C_2H_3]^+$ ($[P - C_5H_2O]^+$)

4.3.2 Effect of different sputtering sources on depth profiling of HKUST-1

Although a large HKUST-1 single crystal (~600 μm) showed a much higher crystallinity and a much more uniform surface, which made it a more favorable material for SIMS analysis and discussion of diffusion behavior inside HKUST-1 crystals, it would be challenging to determine the sputter rate due to the lack of reference for the actual thickness of the sputtered material, resulting in the difficulty to deduce the depth in the depth profiles. Therefore, HKUST-1 thin film prepared by spin coating were used for determining the appropriate sputter parameters and denoted as HKUST-1_spin.

4.3.2.1 Depth profiling HKUST-1 thin film by single beam sputtering

To construct a depth profile of a HKUST-1 thin film, it is crucial to identify suitable sputtering parameters that introduce little damage to the HKUST-1 structure while achieving a high sputter rate. Thus, HKUST-1_spin was used to find the optimal

doi:10.6342/NTU202303887

parameters for constructing a depth profile of HKUST-1 using various sputtering sources with tunable acceleration voltages, namely Ar^+, C_{60}^+, and Ar_{2500}^+. To compensate the fluctuations in the intensity of the primary ion, relative intensities were employed to evaluate signal strength instead of counts. The relative intensities of $[Cu]^+$ and $[C_7H_5O]^+$ are used to evaluate metallic and organic signals and represented by blue and red lines respectively. The obtained depth profiles are shown in figure. 4.13 to figure. 4.15 and it could be seen that the organic signals suffered significant drops in all profiles, indicating excessive damage accumulation for organic component.

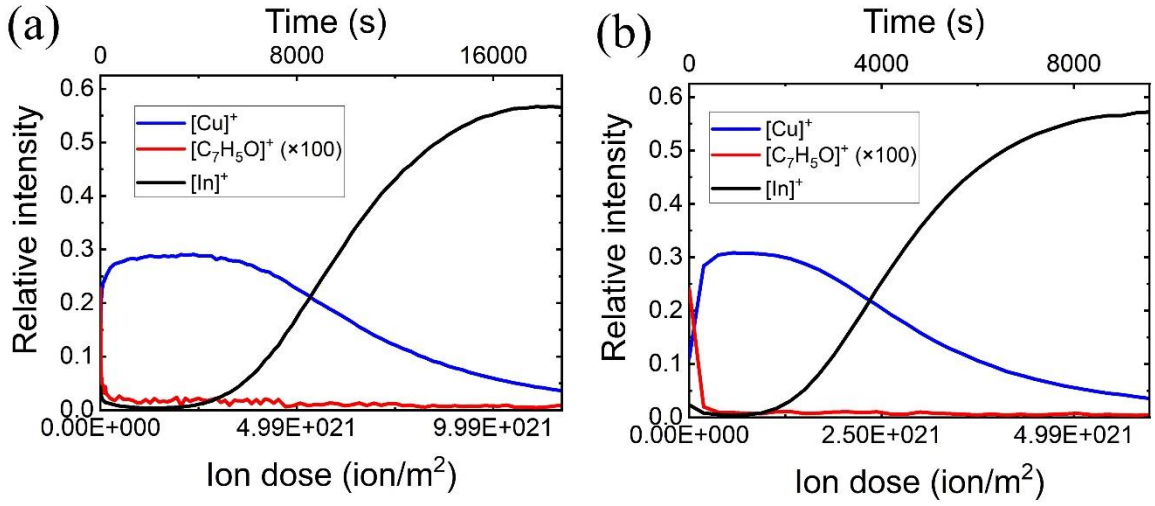

Figure 4.13 Depth profiles of HKUST-1_spin obtained using Ar^+ with acceleration voltages of (a) 500 V Ar^+ and (b) 1 kV as the sputtering sources.

doi:10.6342/NTU202303887

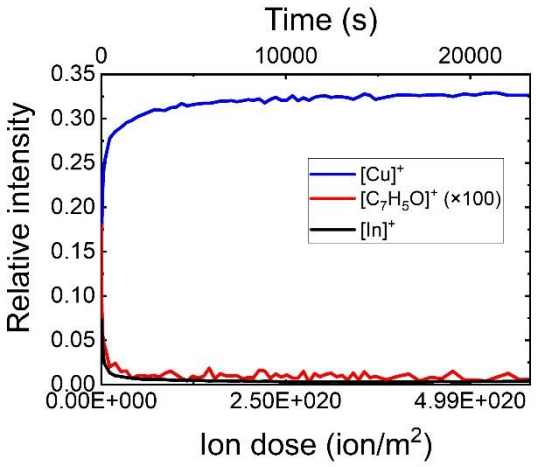

Figure 4.14 Depth profiles of HKUST-1_spin obtained using C_{60}^{+} with an acceleration voltage of 20 kV as the sputtering sources.

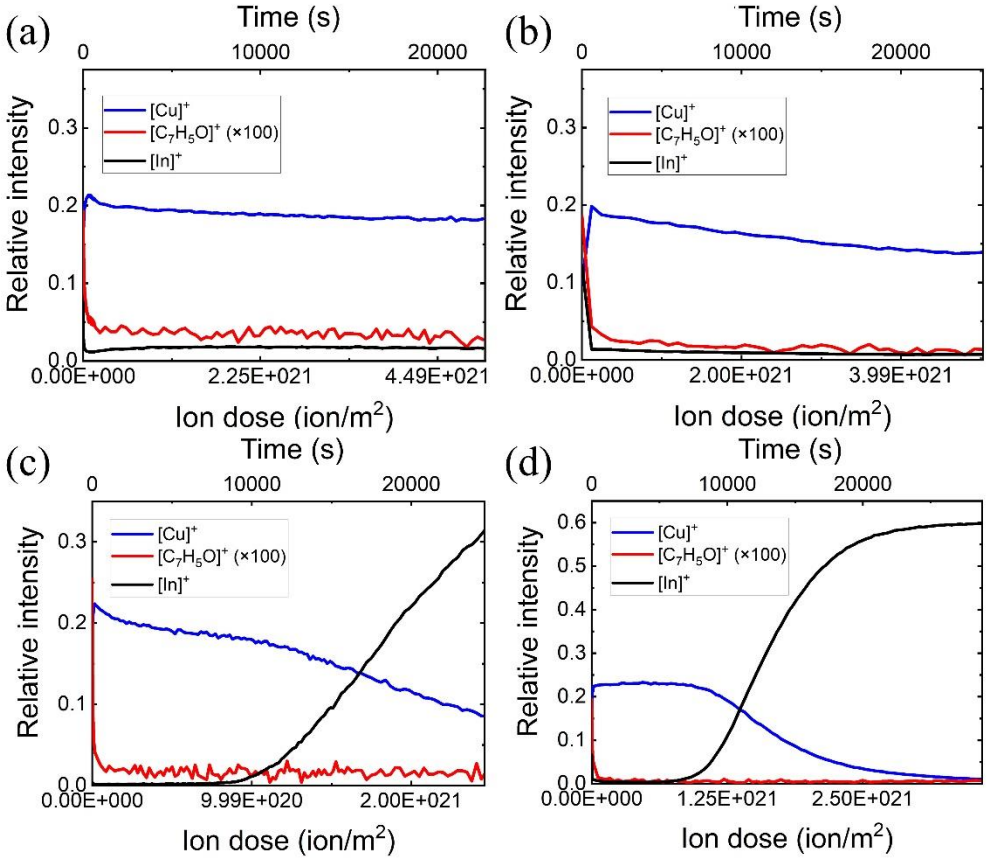

Figure 4.15 Depth profiles of HKUST-1_spin obtained using Ar_{2500}^{+} with acceleration

doi:10.6342/NTU202303887

voltages of (a) 5 kV, (b) 10 kV, (c) 15 kV and (d) 20 kV as the sputtering sources.

The relative intensities of $[C_7H_5O]^+$ at steady state obtained by different sputtering parameters are illustrated in figure 4.16. Although there is a vague trend where the relative intensity of $[C_7H_5O]^+$ at steady state decreases with higher energy density of sputter source, the values are all below 4×10^{-4} which are too low to be even differentiated from the background signal, suggesting that these sputtering parameters are unable to reveal the organic part in HKUST-1 structure.

In addition, the sputter yield obtained by each sputter parameter is shown in figure 4.17. There is no data for 5kV Ar_{2500}^+, 10kV Ar_{2500}^+, and 20kV C_{60}^+ because the sputter yields of these three parameters were so low that the 805 nm HKUST-1_spin thin film could not be removed in a reasonable time. Nonetheless, beside of the extremely low sputter rate, it has been shown that organic signal could not be preserved using these three sputter sources either.

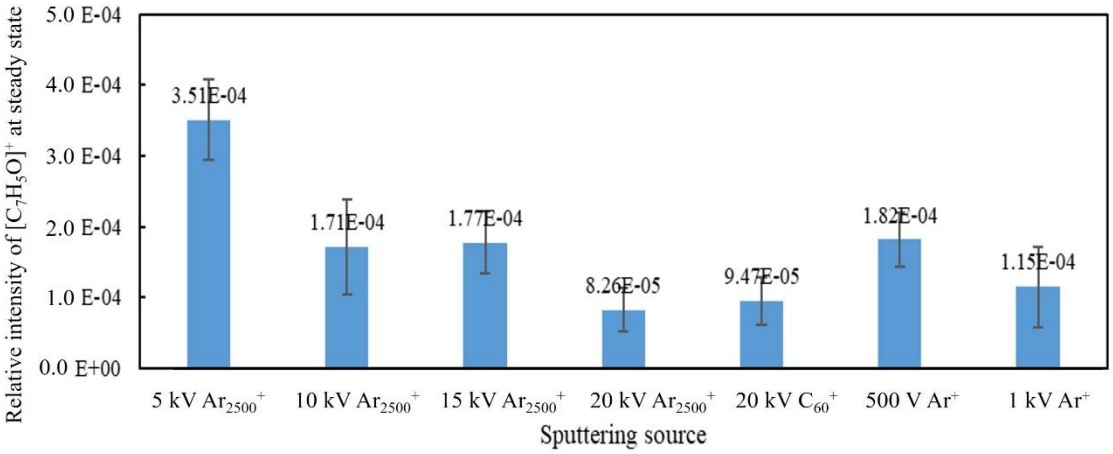

Figure 4.16 The relative intensity of $[C_7H_5O]^+$ at steady state of each sputtering source for HKUST-1_spin.

doi:10.6342/NTU202303887

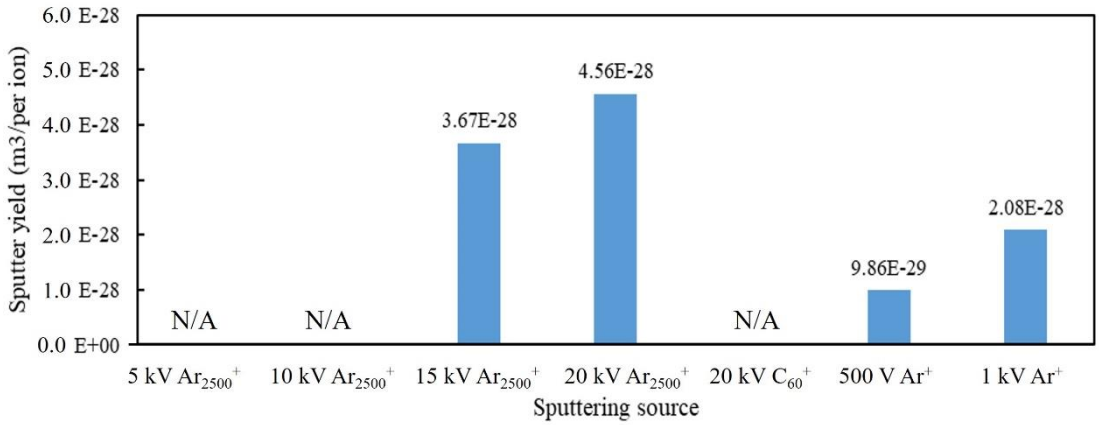

Figure 4.17 Sputter yield of each sputtering source for HKUST-1_spin.

Therefore, cosputtering of Ar^+ and Ar_{2500}^+ was employed in the hope of that the high energy density beam Ar^+ could assist removal of metallic part in HKUST-1 and alleviate preferential sputtering, leading to a depth profile illustrating both metallic and organic signals.

4.3.2.2 Depth profiling HKUST-1 thin film by dual beam cosputtering

Therefore, Ar_{2500}^+ with acceleration voltages of 5 kV, 10 kV, 15 kV and 20 kV were used as the sputter beam cosputtered with Ar^+ with the beam energies of 500 eV or 1 keV and a current density of 25 nA/m^2. The obtained profiles are shown in figure 4.18 and figure 4.19 respectively. The relative intensity of $[C_7H_5O]^+$ at steady state and the sputter rate for each cosputter parameter are also obtained from the profiles and shown in figure 4.20 and figure 4.21 respectively. Unfortunately, all profiles show even lower $[C_7H_5O]^+$ signal than using Ar_{2500}^+ along except 20 kV Ar_{2500}^+ cosputtered with 1 kV Ar^+ which is still within the range of error. Nonetheless, the sputter rates show increases with the

doi:10.6342/NTU202303887

assistance of Ar^+ cosputtering. It could be suggested that although cosputtering of Ar^+ yielded higher sputter rate, it was not enough to remove the damages introduced by Ar_{2500}^+. Moreover, Ar^+ even introduced more damage than it could remove, resulting in lower organic signals than using Ar_{2500}^+ along.

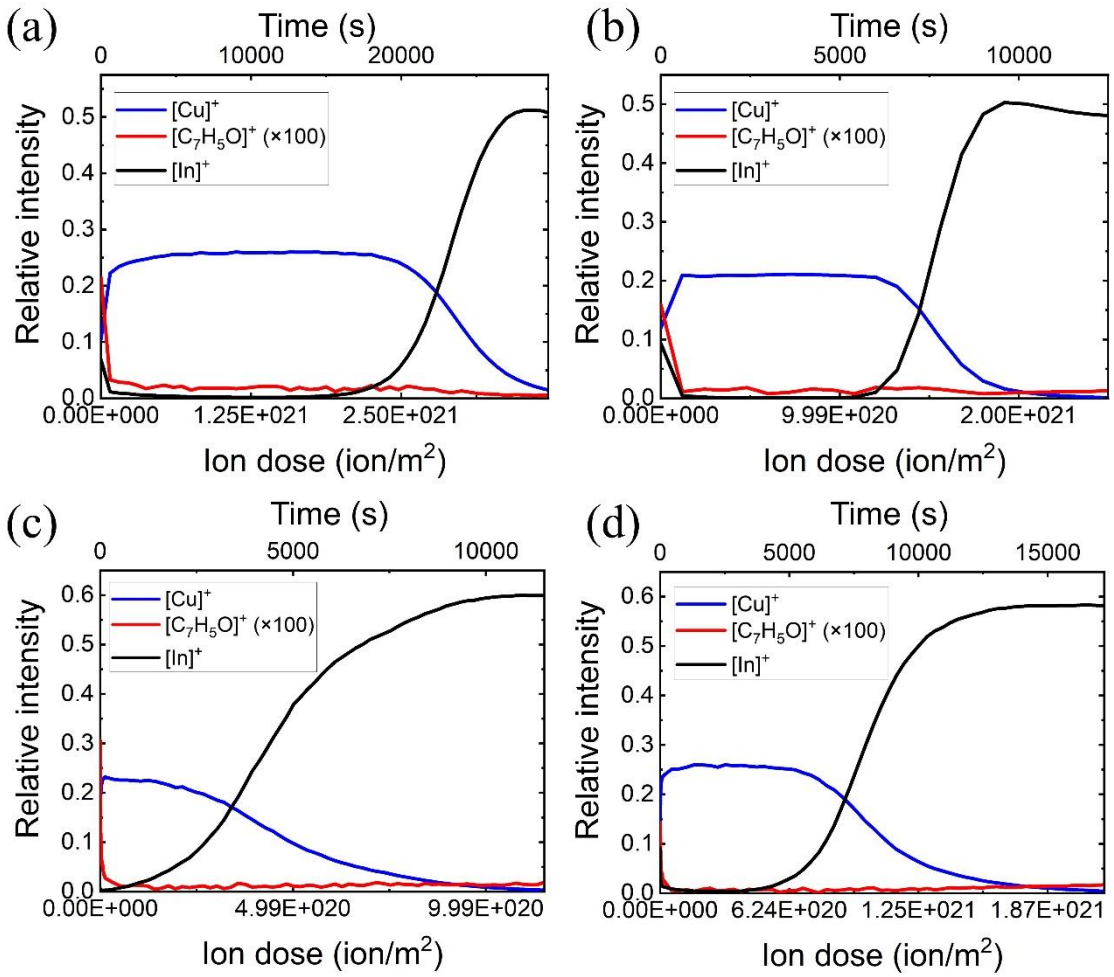

Figure 4.18 Depth profiles of HKUST-1_spin obtained using Ar_{2500}^+ cosputtered with Ar^+ with an acceleration voltage of 500 V and a current density of 25 nA/m^2. The acceleration voltages of Ar_{2500}^+ were (a) 5 kV, (b) 10 kV, (c) 15 kV and (d) 20 kV respectively.

doi:10.6342/NTU202303887

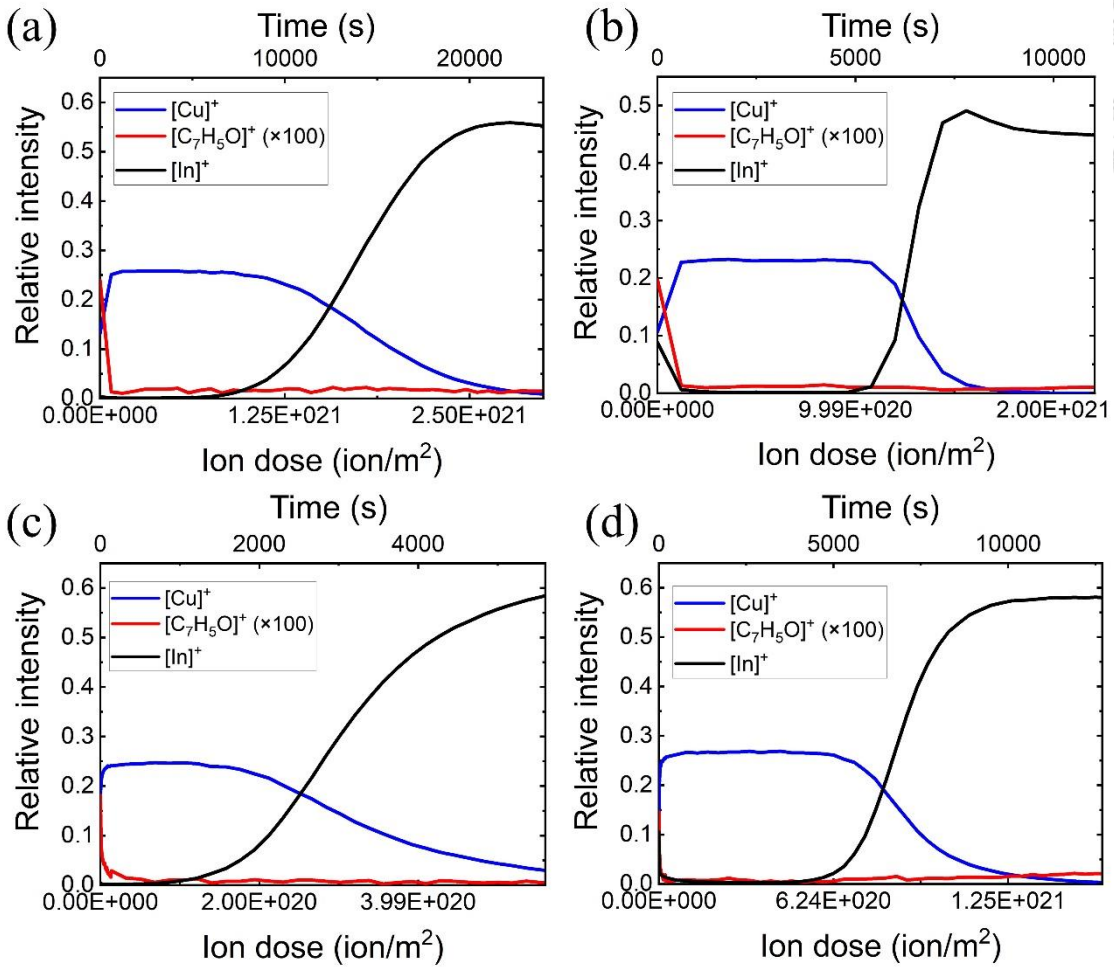

Figure 4.19 Depth profiles of HKUST-1_spin obtained using Ar_{2500}^{+} cosputtered with Ar^{+} with an acceleration voltage of 1 kV and a current density of 25 nA/m^2. The acceleration voltages of Ar_{2500}^{+} were (a) 5 kV, (b) 10 kV, (c) 15 kV and (d) 20 kV respectively.

doi:10.6342/NTU202303887

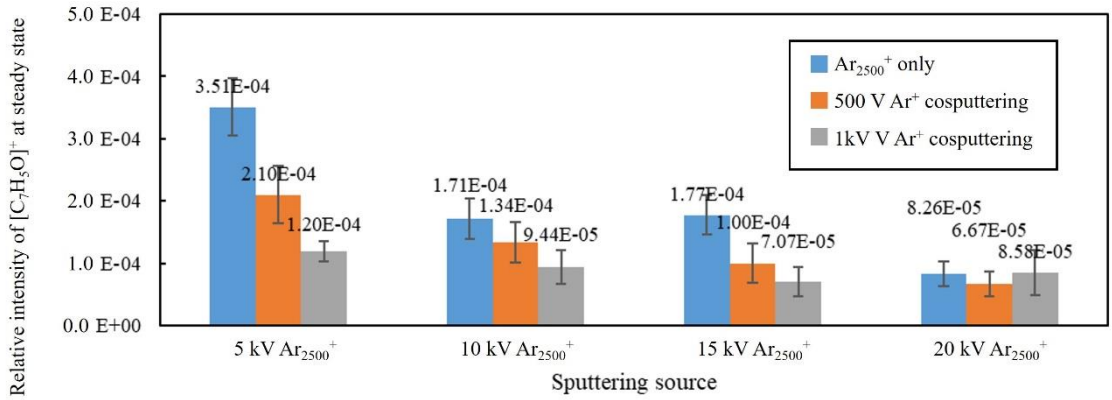

Figure 4.20 The relative intensity of $[C_7H_5O]^+$ at steady state of each cosputter parameter for HKUST-1_spin.

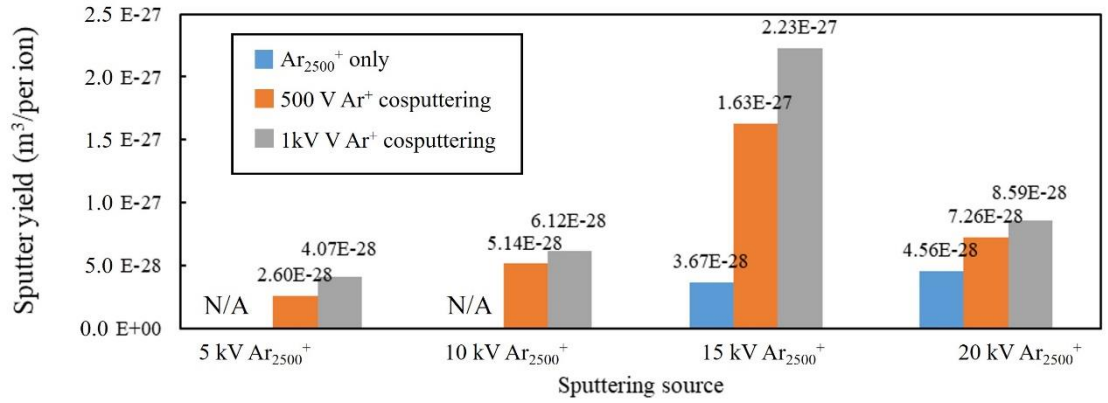

Figure 4.21 Sputter yield of each cosputter parameter for HKUST-1_spin.

It has been concluded that depth profiles of HKUST-1 cannot be constructed using the technique available in our lab without suffering a significant loss of organic signal and it would be necessary to employ another MOF material with a better accessibility to depth profiling for further research. Therefore, ToF-SIMS analysis of ZIF-8 thin film would be discussed in the following section.

doi:10.6342/NTU202303887

4.4 ToF-SIMS analysis of ZIF-8

ZIF-8 is composed of Zn^{2+} as metallic nodes and 2-mIm coordinated to Zn^{2+} as organic linkers with a ratio of 1:2. In order to construct a depth profile of ZIF-8 thin film with ToF-SIMS, it is necessary to determine the peaks which correspond to the metallic node and the organic ligand respectively to illustrate the ZIF-8 structure genuinely.

4.4.1 Determination of the characteristic peaks of ZIF-8

The mass spectra of ZIF-8_ spin and ZIF-8_elec were collected under negative ion mode and shown in figure 4.22. Both spectra show identical peaks with similar intensities between the two spectra which is a reasonable result given the fact that they have the same chemical structure. The peaks with m/z = 26, 50 and 81 corresponded to $[CN]^-$, $[C_3N]^-$ and $[C_4N_2H_5]^-$ respectively, which are all fragments of 2-mIm. Among them, $[C_4N_2H_5]^-$ exactly corresponds to a deprotonated 2-mIm which is the linker in ZIF-8. Therefore, it is reasonable to use $[C_4N_2H_5]^-$ to represent the linker in ZIF-8 in the following discussion.

doi:10.6342/NTU202303887

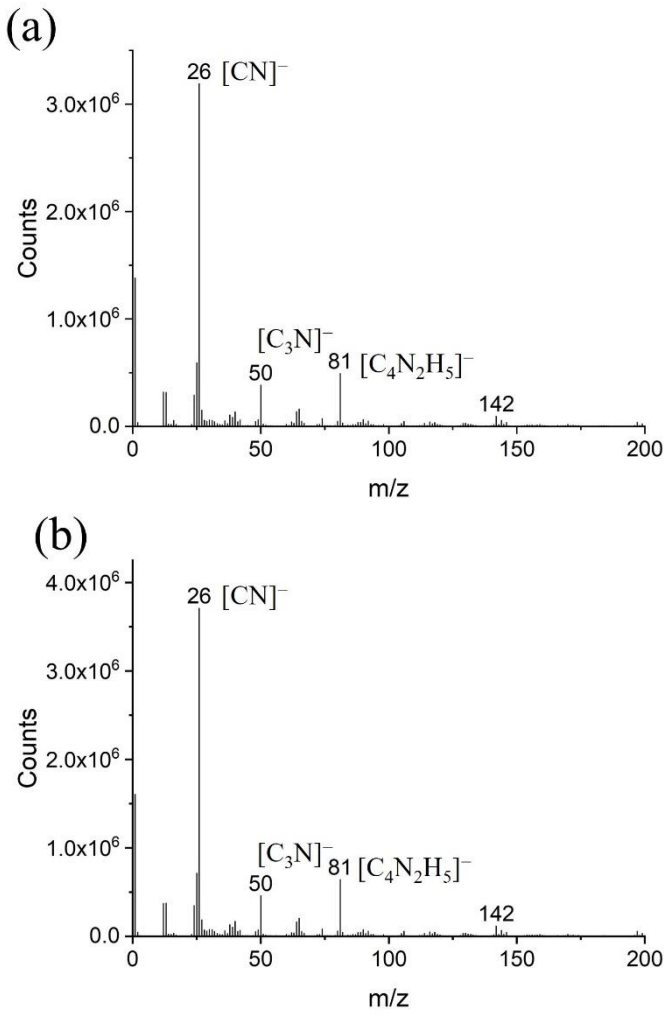

Figure 4.22 Mass spectra of (a) ZIF-8_spin and (b) ZIF-8_elec.

Furthermore, peaks which could correspond to the metallic node of ZIF-8 must be determined as well. Since the fragment of the metallic node of ZIF-8 must contain zinc which has an exact atomic mass of 63.9291 Da, it could be narrowed down to peaks with the m/z larger than 63.9291 Da and smaller than an integral. In addition, there are 5 stable isotopes for naturally occurring zinc on earth, namely ^{64}Zn, ^{66}Zn, ^{67}Zn, ^{68}Zn, and ^{70}Zn with the abundance of 48.6, 27.9, 4.1, 18.8, and 0.6% respectively. Thus, if a peak

doi:10.6342/NTU202303887

corresponds to a fragment containing zinc, other peaks with respective abundance must also be found. Following the rules mentioned above, peak with m/z = 142 was found to be a promising peak which could correspond to the metallic node of ZIF-8 because its exact mass which is shown in figure 4.23 (a) matched the exact mass of $[ZnC_4N_2H_2]^-$ (141.9509 Da) accurately, corresponding to a Zn coordinated by a 2-mIm.

Moreover, the counts for all stable isotopes of $[ZnC_4N_2H_2]^-$ are calculated according to the counts of $^{142}[ZnC_4N_2H_2]^-$ and shown in figure 4.23 (b) represented by blue dots and show good matches for the more abundant isotopes, i.e. $^{142}[ZnC_4N_2H_2]^-$, $^{144}[ZnC_4N_2H_2]^-$ and $^{146}[ZnC_4N_2H_2]^-$. However, the counts detected at the less abundant isotopes, i.e. $^{143}[ZnC_4N_2H_2]^-$ and $^{145}[ZnC_4N_2H_2]^-$ show excesses than expected based on the counts of $^{142}[ZnC_4N_2H_2]^-$ detected. It is suggested that the deviation comes from $^{143}[ZnC_4N_2H_3]^-$ which has one hydrogen more than $^{142}[ZnC_4N_2H_2]^-$. It is assumed that the excess counts detected at m/z = 143 are all attributed to $^{143}[ZnC_4N_2H_3]^-$ and the counts of the other isotopes of $[ZnC_4N_2H_3]^-$ are calculated according to the counts of $^{143}[ZnC_4N_2H_3]^-$. The red cubes in figure 4.23 (b) show the result after the counts of isotopes of $[ZnC_4N_2H_3]^-$ have been added to the counts of isotopes of $[ZnC_4N_2H_2]^-$ and good matches could be seen, further confirming that the peak at m/z = 142 is $^{142}[ZnC_4N_2H_2]^-$.

In brief, the peaks which could represent organic linkers and metallic nodes in ZIF-8 in the mass spectrum were determined to be $^{81}[C_4N_2H_5]^-$ and $^{142}[ZnC_4N_2H_2]^-$ respectively and would be used for further analysis in the following discussions.

doi:10.6342/NTU202303887

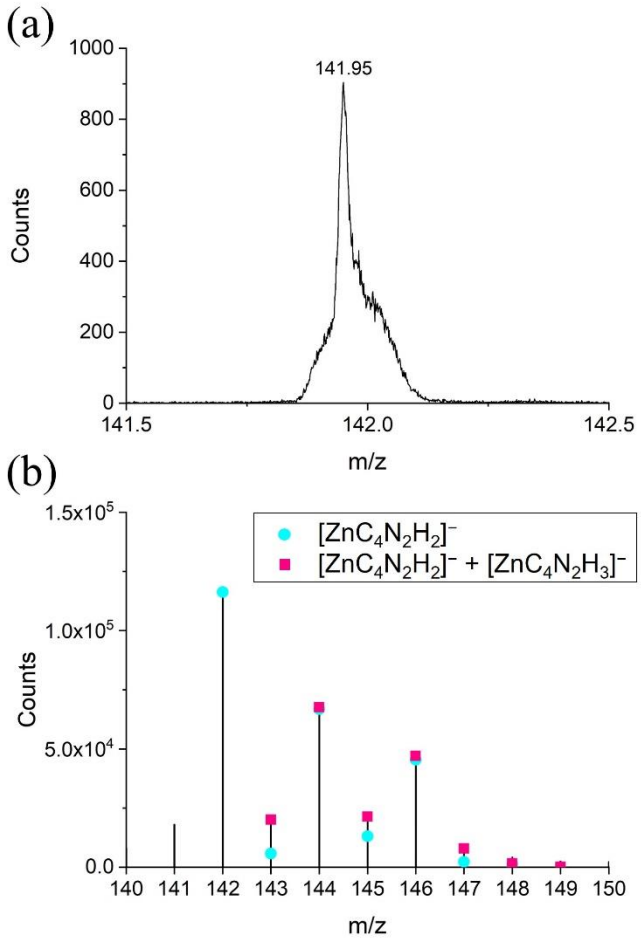

Figure 4.23 (a) Mass spectrum of ZIF-8_elec at m/z = 142 and (b) mass spectrum of ZIF-8_elec between m/z = 140 and 150.

4.4.2 Effect of different sputtering sources on depth profiling of a ZIF-8 thin film

In order to construct a depth profile of a ZIF-8 thin film, it is necessary to determine an appropriate sputtering parameter which introduces little to no damage to ZIF-8 structure and yields a high sputter rate. Therefore, different sputtering sources were employed including Ar^+, C_{60}^+ and Ar_{2500}^+ with tunable acceleration voltage to find out the optimal sputtering conditions for constructing one depth profile of a ZIF-8 thin film. The

doi:10.6342/NTU202303887

relative intensities were utilized to assess the strength of the signal instead of the counts to compensate the fluctuation in the intensity of primary ion.

The obtained depth profiles are shown in figure 4.24 to figure 4.26. Red line represents the relative intensity of $[C_4N_2H_5]^-$, green line represents the relative intensity of $[ZnC_4N_2H_2]^-$ and black line represents the relative intensity of $[InO]^-$, which correspond to the organic linker of ZIF-8, metallic nodes of ZIF-8, and ITO glass respectively. In the profiles, it could be seen that the relative intensity of $[C_4N_2H_5]^-$ usually decays at first and then shows a flat steady state. However, according to the crystal structure determined for ZIF-8_elec, the ratio between linkers and nodes remains at 2:1. In addition, ratio between the relative intensity of $[C_4N_2H_5]^-$ and the relative intensity of $[ZnC_4N_2H_2]^-$ for the same ZIF-8_elec sample differs with different sputtering sources, which further suggests that the variation of the relative intensity of $[C_4N_2H_5]^-$ is not due to the inherent crystal structure variation but more likely due to sputter-induced structure damage.

After the ZIF-8_elec was removed and ITO glass was revealed, both the relative intensity of $[C_4N_2H_5]^-$ and the relative intensity of $[ZnC_4N_2H_2]^-$ showed abrupt decays while the relative intensity of $[InO]^-$ showed an abrupt increase.

doi:10.6342/NTU202303887

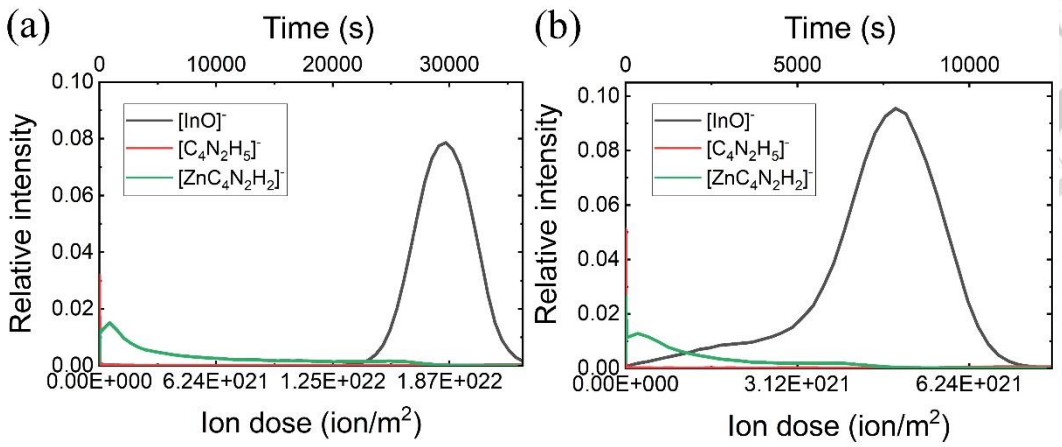

Figure 4.24 Depth profiles of ZIF-8_elec obtained using Ar^+ with acceleration voltages of (a) 500 V Ar^+ and (b) 1 kV as the sputtering sources.

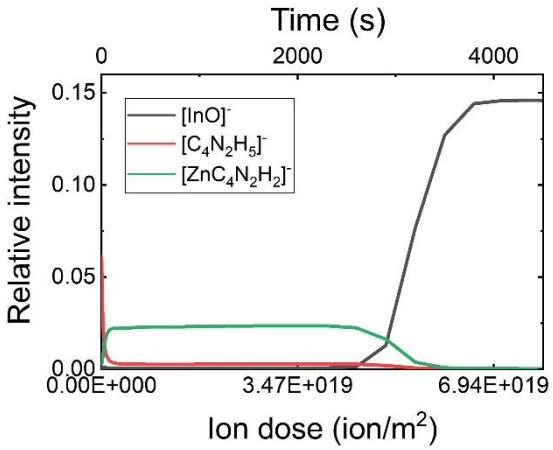

Figure 4.25 Depth profiles of ZIF-8_elec obtained using C_{60}^+ with an acceleration voltage of 20 kV as the sputtering sources.

doi:10.6342/NTU202303887

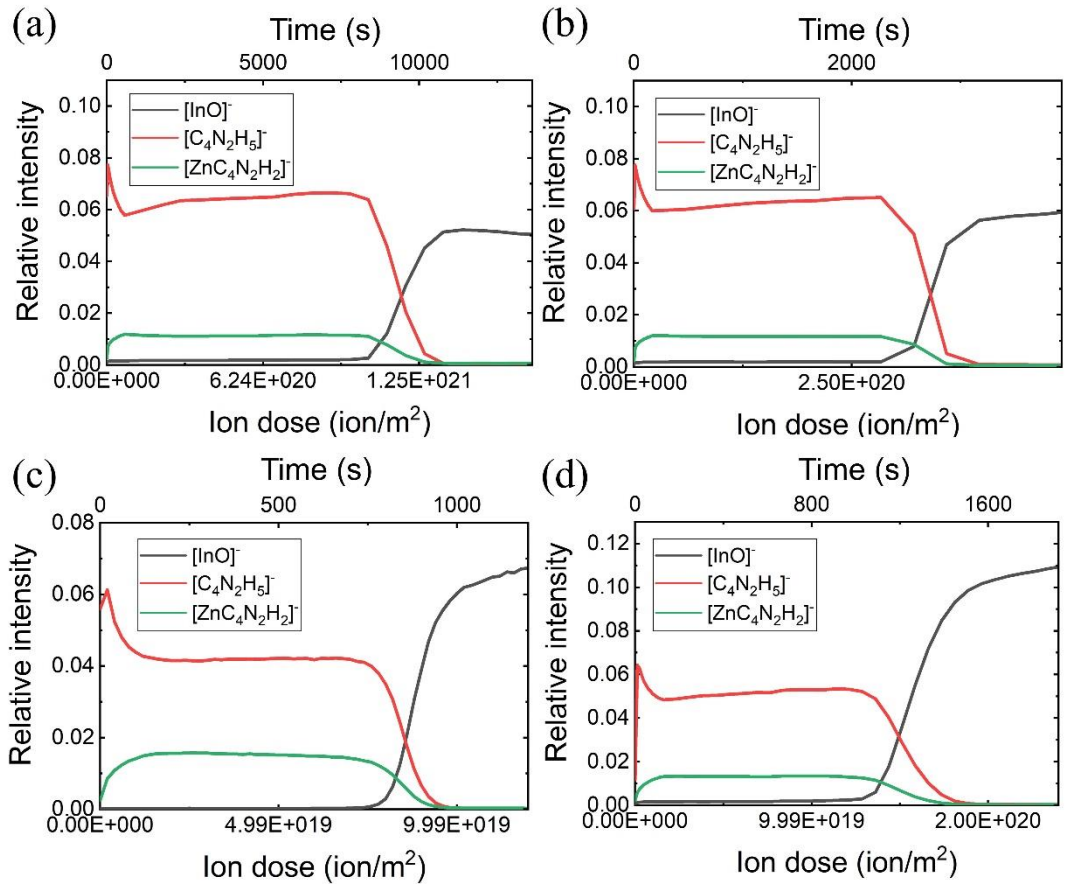

Figure 4.26 Depth profiles of ZIF-8_elec obtained using Ar_{2500}^{+} with acceleration voltages of (a) 5 kV, (b) 10 kV, (c) 15 kV and (d) 20 kV as the sputtering sources.

The obtained depth profiles will be evaluated with three values to determine whether the sputter parameter is favorable, which are relative intensity of $[C_4N_2H_5]^-$ at steady state, effective disappearance cross-section, and sputter rate.

4.4.2.1 Relative intensity of $[C_4N_2H_5]^-$ at steady state

The relative intensity of $[C_4N_2H_5]^-$ at steady state was averaged by collecting intensities from the flat region and is shown in the figure 4.27 In general, the relative intensity of $[C_4N_2H_5]^-$ show a decreasing trend with increasing energy density. The sputtering source with the lowest energy density, 5 kV Ar_{2500}^{+}, shows the highest relative

doi:10.6342/NTU202303887

intensity of $[C_4N_2H_5]^-$, which is reasonable since organic signals tend to be more susceptible to damage when using a sputtering source with a higher energy density, as previously reported.[165] Although 15 kV Ar_{2500}^+ shows a lower relative intensity of $[C_4N_2H_5]^-$ at steady state than 20 kV Ar_{2500}^+, the difference is not significant compared to that observed with C_{60}+ and Ar^+, which show values that are one and two orders of magnitude less than 15 kV Ar_{2500}^+, respectively.

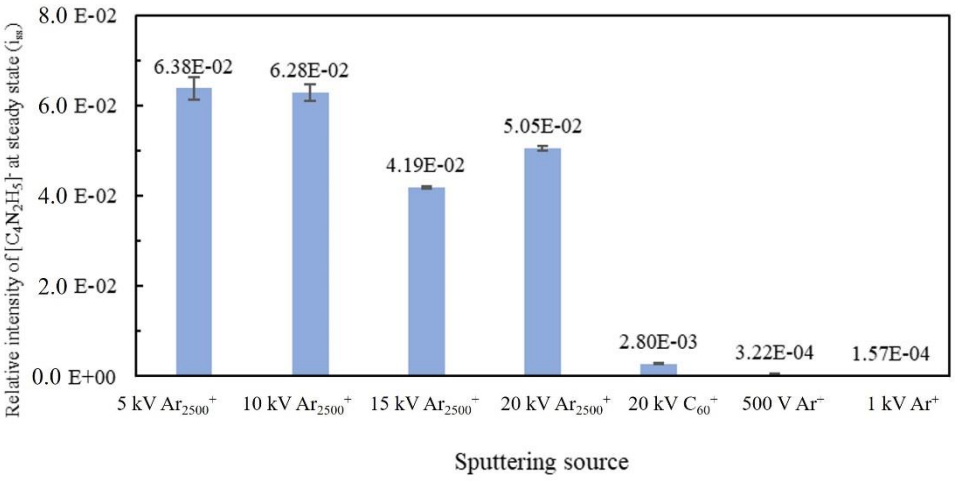

Figure 4.27 The relative intensity of $[C_4N_2H_5]^-$ at steady state of each sputtering source for ZIF-8_elec.

4.4.2.2 Effective disappearance cross-section (σ_{eff})

The damage introduced by sputtering is evaluated by effective disappearance cross-section σ_{eff}, which is defined as:

$$i(x) = i_{ss} + i_{0-ss}\exp(-\sigma_{eff} \times x) \qquad \text{Eq. 4.1}$$

where i is the measured signal intensity of interest at x fluence; i_{ss} is the signal intensity at steady state; $i_{0\text{-}ss}$ is difference between intensity at zero fluence and steady

doi:10.6342/NTU202303887

state; σ_{eff} is the effective disappearance cross-section.[166] In this experiment, σ_{eff} were obtained by fitting to eq. 4.1 using Origin 2018© and shown in figure 4.28 to figure 4.30.

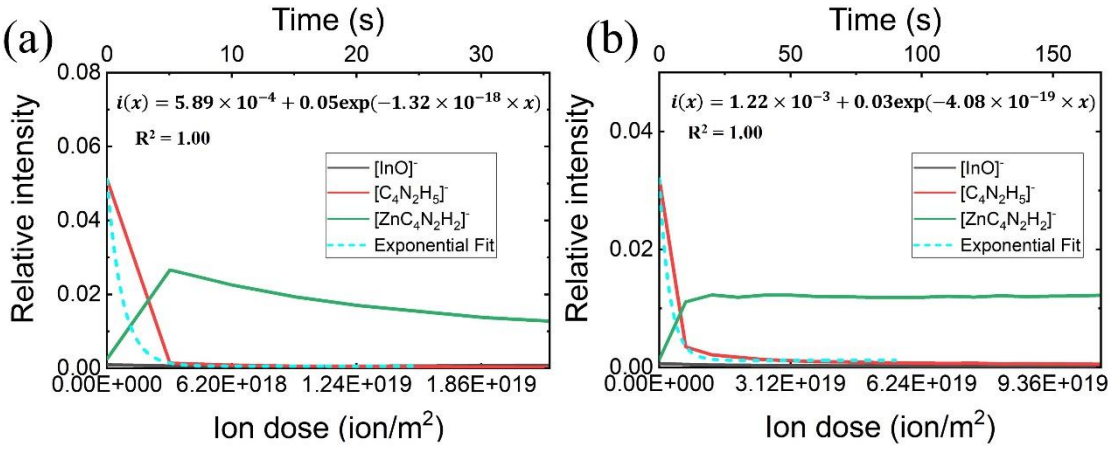

Figure 4.28 Fitting results of depth profiles of ZIF-8_elec to eq. 4.1 respectively using Ar^+ with acceleration voltages of (a) 500 V Ar^+ and (b) 1 kV as the sputtering sources.

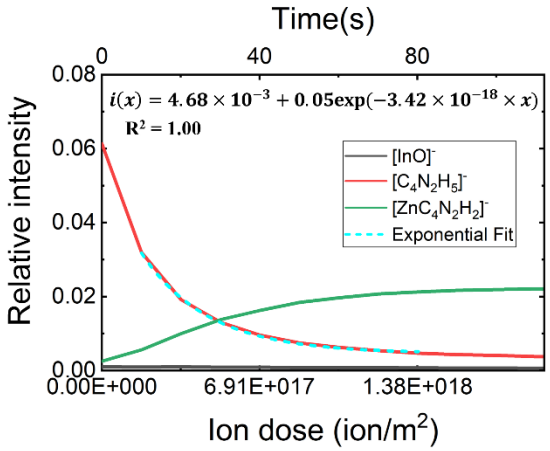

Figure 4.29 Fitting results of depth profiles of ZIF-8_elec to eq. 4.1 respectively using C_{60}^+ with an acceleration voltage of 20 kV as the sputtering sources.

doi:10.6342/NTU202303887

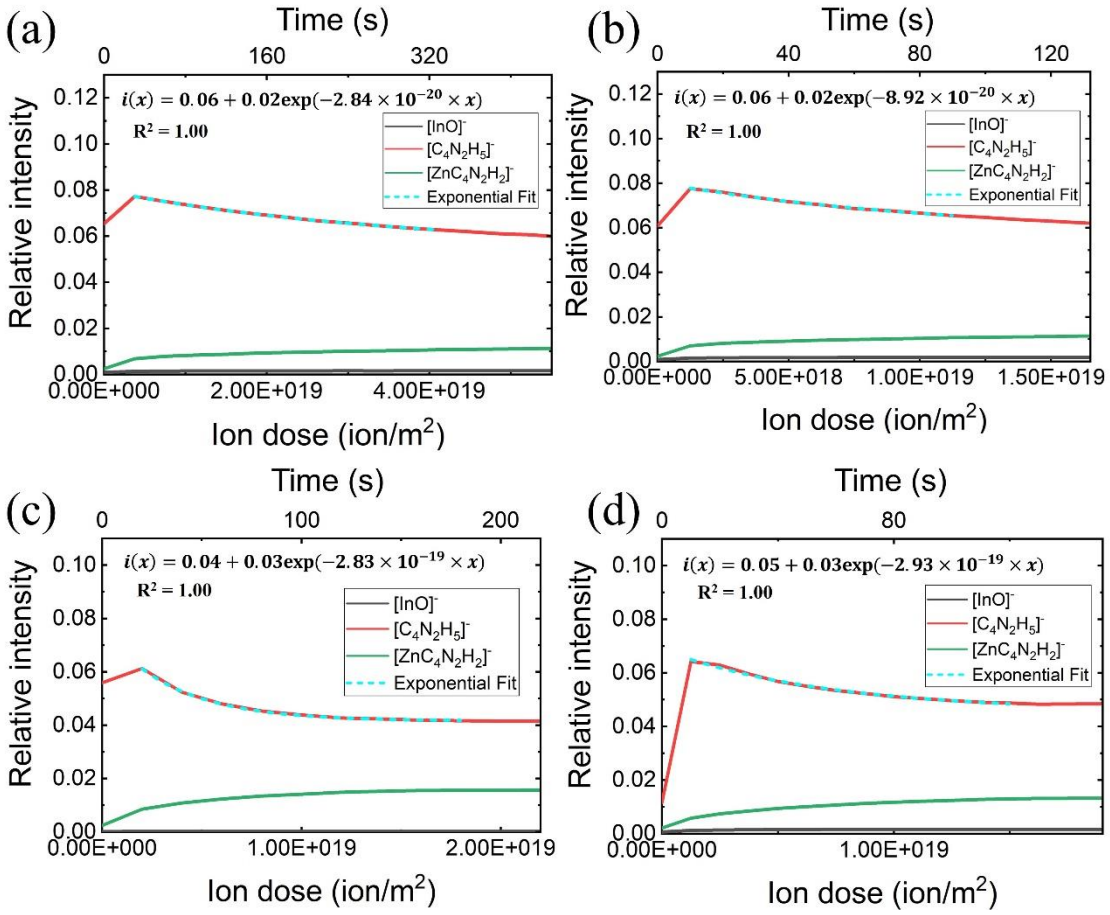

Figure 4.30 Fitting results of depth profiles of ZIF-8_elec to eq. 4.1 respectively using Ar_{2500}^+ with acceleration voltages of (a) 5 kV, (b) 10 kV, (c) 15 kV and (d) 20 kV as the sputtering sources.

Figure 4.31 indicates that $-\sigma_{eff}$ increased with the energy density of the sputtering source. This trend is reasonable because ions with higher energy densities tend to penetrate deeper into the sample and destroy bonds more, causing more damage in a thicker altered layer. However, the data shows an exception in the case of 20 kV C_{60}^+, which has an energy density of 333.33 eV/atom and exhibits the highest $-\sigma_{eff}$ among the seven sputtering sources used in the experiment. Surprisingly, this value is even higher

doi:10.6342/NTU202303887

than that obtained using 1 kV Ar^+, which has an energy density of 1000 eV/atom. It is suggested that this inconsistency is caused by the deposition of amorphous carbon on the surface of the sample after sputtering with C_{60}^+, which has been reported to occur when the sample is a carbon-based polymorphic material.[167] In summary, the data indicates that 5 kV Ar_{2500}^+ has the lowest $-\sigma_{eff}$ and $-\sigma_{eff}$ increases with energy density, with the exception of 20 kV C_{60}^+ due to the deposition of amorphous carbon on the sample surface.

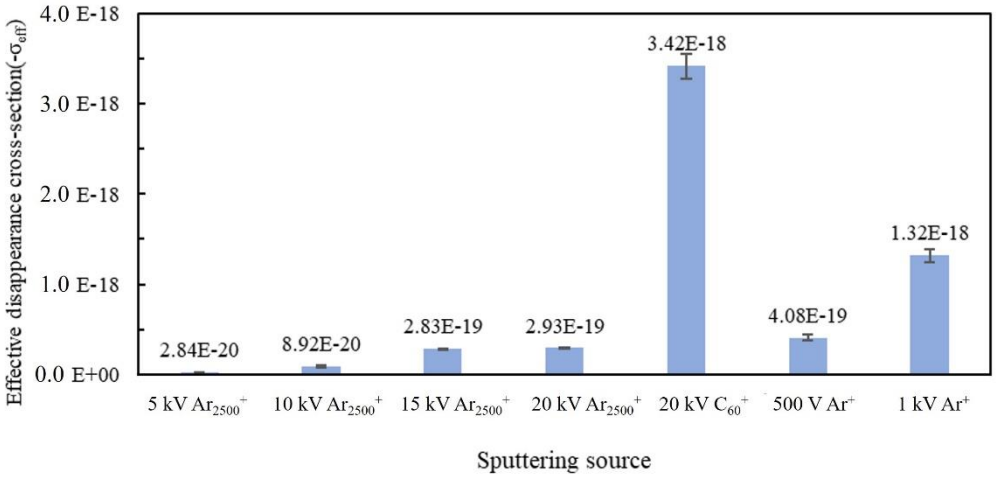

Figure 4.31 Effective disappearance cross-section($-\sigma_{eff}$) of each sputtering source for ZIF-8_elec.

4.4.2.3 Sputter yields

The sputter yields were calculated by dividing the thickness of ZIF-8_elec (635 ± 60 nm) by the fluence of the sputtering ion when the relative intensity of $[C_4N_2H_5]^-$ was half of the value at steady state. The sputtering rates are shown in figure 4.32 and show a trend of increase with energy density in general for cluster ion sources including both Ar_{2500}^+ and C_{60}^+. However, despite the atomic source Ar^+ has the highest energy density, it shows

doi:10.6342/NTU202303887

the lowest sputtering rate. This was attributed to the nonlinear enhancement effect observed in organic materials when cluster ion beams were used for sputtering. This effect was previously reported in the literature[168] and was also observed in this experiment for ZIF-8 material. Therefore, it could be concluded that cluster ion beams are more efficient than atomic ion beams for removing ZIF-8_elec.

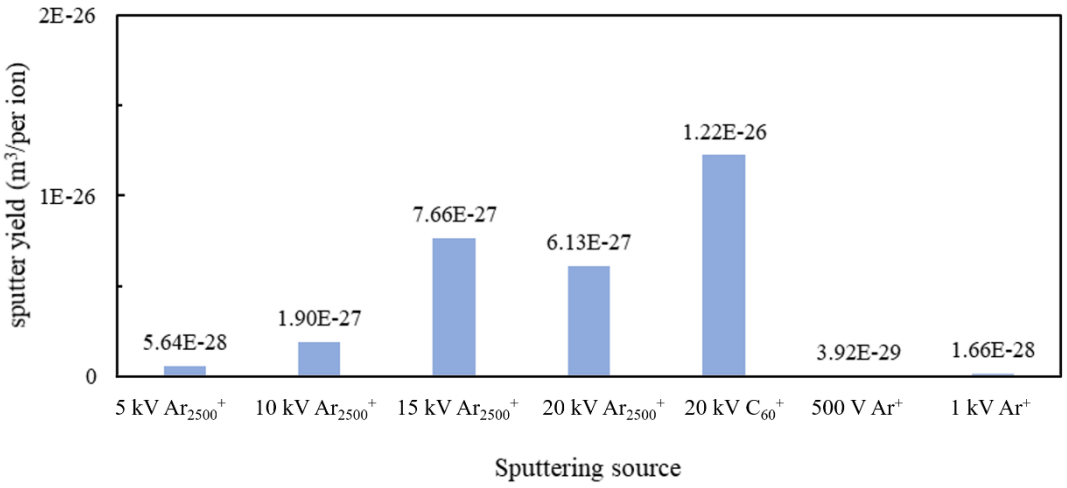

Figure 4.32 Sputter yields of each sputtering source for ZIF-8_elec.

To sum up, cluster ion beams all show more prominent relative intensities of $[C_4N_2H_5]^-$ and higher sputtering rates than the atomic ion beam Ar^+, which all indicate that cluster ion beams are more ideal for sputtering to constantly depth profiling ZIF-8_elec. Between two cluster ion beams in this experiment, 20 kV C_{60}^+ shows a relative intensity of $[C_4N_2H_5]^-$ at steady state an order less than all those obtained using Ar_{2500}^+, which will be problematic in studying organic signal. Moreover, despite 20 kV C_{60}^+ shows a higher sputtering rate, the actual time needed for sputtering using 20 kV C_{60}^+ is higher due to the lower achievable current of 20 kV C_{60}^+ in the instrument used in our lab.

doi:10.6342/NTU202303887

Therefore, Ar_{2500}^+ appears to be the best choice of sputtering source for this experiment.

To determine the optimal acceleration voltage of Ar_{2500}^+, sputtering rate is considered more important than $-\sigma_{eff}$ and the relative intensity of $[C_4N_2H_5]^-$ because the damages introduced by Ar_{2500}^+ to the organic signal are all low enough, allowing studying without any problem. Thus, among them 15 kV Ar_{2500}^+ show the highest sputtering rate and will be used for further analysis.

4.4.3 Depth profile of ZIF-8 loaded with model drugs

Acetaminophen and caffeine were chosen as the two model drugs to determine the loading behavior. Acetaminophen is a widely adopted analgesic drug to treat symptoms such as fever and headache, and it has been previously utilized as a model drug in the studies of other drug delivery systems.[169,170] Additionally, caffeine is a frequently used adjuvant in combination with acetaminophen which has been discussed in conjunction with acetaminophen in numerous studies.[171–174] Therefore, acetaminophen and caffeine were utilized as model drugs to evaluate the drug loading behavior of ZIF-8 in this work where acetaminophen and caffeine were loaded into ZIF-8 thin film by immersing ZIF-8 thin film in solutions of acetaminophen or caffeine.

4.4.3.1 Determination of the characteristic peaks of model drugs loaded in ZIF-8

In order to track the acetaminophen and caffeine molecules in ZIF-8 thin film, it is necessary to determine the peaks that represent acetaminophen and caffeine in mass spectra first. Figure 4.33 (a) shows the spectrum of acetaminophen collected under negative ion mode and the molecular structure of acetaminophen is shown in figure 4.33

doi:10.6342/NTU202303887

(b). The peaks at m/z = 150, 134 and 107 correspond to $[C_8H_8NO_2]^-$, $[C_7H_4NO_2]^-$ and $[C_6H_5NO]^-$ respectively which are all fragments of acetaminophen.

In order to compensate the difference in the fluence of primary ion, relative intensity is employed to assess the intensity of each peak. Table 4.2 shows the relative intensities of these three peaks corresponding to acetaminophen in ZIF-8_elec without acetaminophen loading and ZIF-8_elec that had been immersed in 10 mM ethanolic solution of acetaminophen for 24 hours ($ACE_{(EtOH)}$@ZIF-8 _elec_24hr). $ACE_{(EtOH)}$@ZIF-8_elec_24hr shows a clear increase in the relative intensities of peaks representing acetaminophen after being immersed in acetaminophen solution. Among these three peaks, $[C_8H_8NO_2]^-$ shows the lowest background and an increase of more than an order of magnitude in the relative intensity after immersed in the acetaminophen solution.

Briefly, these three peaks are proven to be valid to represent acetaminophen loaded in ZIF-8 thin film. Nonetheless, $[C_8H_8NO_2]^-$ shows the lowest background and the highest order of increase, making it the most ideal peak to assess the amount of acetaminophen loaded in ZIF-8_elec.

doi:10.6342/NTU202303887

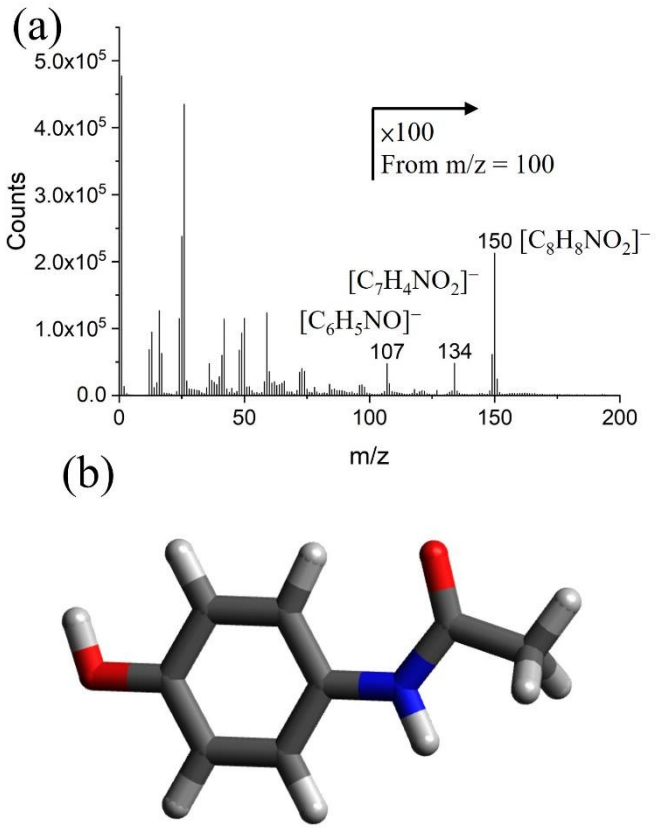

Figure 4.33 (a) Mass spectrum of acetaminophen collected under negative ion mode. (b) Molecular structure of acetaminophen. (white: hydrogen; grey: carbon; blue: nitrogen; red: oxygen)[163]

Table 4.2 Relative intensity of $[C_8H_8NO_2]^-$, $[C_7H_4NO_2]^-$ and $[C_6H_5NO]^-$ in ZIF-8 thin film before and after immersed in ethanolic acetaminophen solution for 24 hours.

	ZIF-8_spin	$ACE_{(EtOH)}$@ZIF-8_spin_24hr	ZIF-8_elec	$ACE_{(EtOH)}$@ZIF-8_elec_24hr
$[C_6H_5NO]^-$	0.46×10^{-3}	1.18×10^{-3}	0.67×10^{-3}	2.85×10^{-3}
$[C_7H_4NO_2]^-$	0.68×10^{-3}	2.84×10^{-3}	1.15×10^{-3}	6.45×10^{-3}
$[C_8H_8NO_2]^-$	0.04×10^{-3}	1.06×10^{-3}	0.09×10^{-3}	3.80×10^{-3}

doi:10.6342/NTU202303887

In addition, the presence of caffeine in ZIF-8 thin film was investigated by identifying peaks that could represent caffeine (molecular formula: $C_8H_{10}N_4O_2$, shown in figure 4.34) first. Our lab had previously identified four peaks, $[C_4H_3N_2O_2]^-$, $[C_6H_4N_4O_2]^-$, $[C_7H_7N_4O_2]^-$, and $[C_8H_9N_4O_2]^-$ that could represent caffeine in UiO-66 crystals.[10] To determine if these peaks could also represent caffeine in ZIF-8, the relative intensities of these four peaks before and after immersion in a 10 mM ethanolic solution of caffeine for 24 hours (CAF@ZIF-8 _24hr) were compared and shown in table 4.3 It should be noted that ZIF-8_spin was used instead of ZIF-8_elec because there was no evident enhancement in any of these four peaks after immersion in caffeine solution for ZIF-8_elec. This will be discussed later, where it was found that little caffeine entered ZIF-8_elec after immersion. All four peaks showed higher intensity after immersion in caffeine solution for ZIF-8_spin, indicating that they could represent caffeine in ZIF-8 as well. Among these peaks, $[C_7H_7N_4O_2]^-$ showed the highest increase in intensity, doubling its value. Therefore, $[C_7H_7N_4O_2]^-$ was used to assess the entry of caffeine into ZIF-8 in further discussions.

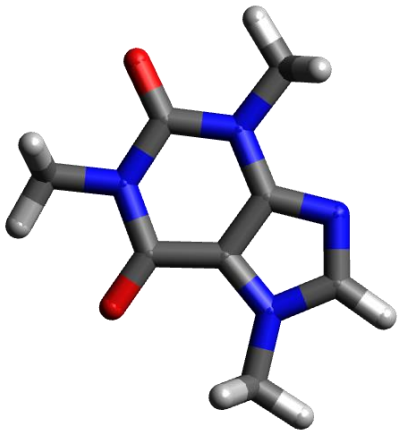

Figure 4.34 Molecular structure of caffeine. (white: hydrogen; grey: carbon; blue: nitrogen; red: oxygen)[163]

doi:10.6342/NTU202303887

Table 4.3 The relative intensity of $[C_4H_3N_2O_2]^-$, $[C_6H_4N_4O_2]^-$, $[C_7H_7N_4O_2]^-$, and $[C_8H_9N_4O_2]^-$ in ZIF-8 thin film before and after immersed in ethanolic caffeine solution for 24 hours.

	ZIF-8_spin	$CAF_{(EtOH)}$@ZIF-8_spin_24hr	ZIF-8_elec	$CAF_{(EtOH)}$@ZIF-8_elec_24hr
$[C_4H_3N_2O_2]^-$	1.95×10^{-4}	2.59×10^{-4}	3.59×10^{-4}	3.00×10^{-4}
$[C_6H_4N_4O_2]^-$	0.73×10^{-4}	1.37×10^{-4}	2.09×10^{-4}	1.45×10^{-4}
$[C_7H_7N_4O_2]^-$	0.93×10^{-4}	2.75×10^{-4}	1.43×10^{-4}	1.55×10^{-4}
$[C_8H_9N_4O_2]^-$	4.94×10^{-5}	6.76×10^{-5}	8.47×10^{-5}	6.88×10^{-5}

4.4.3.2 Determining the diffusion kinetics of molecules in ZIF-8 using depth profiles

Figure 4.35 shows the depth profiles of ZIF-8_spin, ZIF-8_elec, and the profiles of each thin film immersed in 10 mM ethanolic solutions of acetaminophen or caffeine for 24 hours. The orange lines represent the profiles of acetaminophen and the blue lines represent the profiles of caffeine. Figure 4.35 (a) and (b) show the depth profiles of ZIF-8_spin and ZIF-8_elec which both had not been immersed in solutions of acetaminophen nor caffeine. The orange lines and blue lines in figure 4.35 (a) and (b) indicates the background relative intensity of these two peaks in ZIF-8_elec and ZIF-8_spin respectively. Based on the data, only the profile of acetaminophen in $ACE_{(EtOH)}$@ZIF-8_elec _24hr (figure 4.35 (c)) shows a clear concentration profile indicating diffusion, while the profile of caffeine in $CAF_{(EtOH)}$@ZIF-8_elec _24hr (figure 4.35 (e)) only shows an increase in the intensity of the model drug on the very surface. Both samples prepared

doi:10.6342/NTU202303887

by spin coating, namely $ACE_{(EtOH)}$@ZIF-8_spin _24hr and $CAF_{(EtOH)}$@ZIF-8_spin _24hr (figure 4.35 (d) and (f)), show an increase in the intensity of the model drug throughout the whole sample where diffusion gradient could not be observed.

Besides, in the profiles which show the orange lines representing the concentration of acetaminophen (figure 4.35 (a), (b), (c), and (d)), it could be found out that the orange lines all show increases after ZIF-8 thin film was sputtered and ITO substrate was revealed. It does not indicate that acetaminophen exists in ITO substrate but due to the $^{150}[SnO_2]^-$ signal which has the same m/z = 150 as $^{150}[C_8H_8NO_2]^-$.

Furthermore, it is suggested that the morphology of the ZIF-8 thin film plays an important role in the transportation of molecules in the thin film. Figure 4.35 (c) and (d) show the depth profiles of ZIF-8 thin films immersed in ethanolic solution of acetaminophen prepared with different morphologies, namely ZIF-8_elec and ZIF-8_spin. Although acetaminophen was shown to be able to enter at limited depth in ZIF-8_elec, it showed increase in intensity throughout the ZIF-8_spin without diffusion gradient. In spite of diffusion of acetaminophen being extremely faster in ZIF-8_spin, the more reasonable explanation would be the transportation of acetaminophen in ZIF-8_spin is not through the pores in ZIF-8 but rather the space between ZIF-8 nanoparticles, which allowed acetaminophen to move freely. By this means, acetaminophen would have access to all ZIF-8 crystals in ZIF-8_spin no matter the depth it was at.

Moreover, figure 4.35 (e) shows that caffeine only existed near the surface of ZIF-8_elec after ZIF-8_elec being immersed in ethanolic caffeine solution, indicating that caffeine has even more limited access into ZIF-8_elec than acetaminophen. However, figure 4.35 (f) indicates that after ZIF-8_spin had been immersed in ethanolic caffeine

doi:10.6342/NTU202303887

solution, the intensity of caffeine throughout the whole $CAF_{(EtOH)}$@ZIF-8_spin _24hr show increases at all depth without observable diffusion gradient. It further supports the suggestion that guest molecules move freely in ZIF-8_spin through free volumes between nanoparticles where it would be hard to study diffusion in ZIF-8_spin.

By looking closely to the interface between ZIF-8 and ITO substrate, it was found out that ZIF-8_elec (figure 4.35 (a), (c) and(e)) showed a much sharper interface than ZIF-8_spin did (figure 4.35 (b), (d) and (f)), suggesting that there was space between ZIF-8 nanoparticles in ZIF-8_spin which lead to a less densely packed structure. This finding also supports the suggestion that unlike molecules diffuse through intracrystalline pores in ZIF-8_elec, molecules move freely through space between ZIF-8 nanoparticles in ZIF-8 spin.

Therefore, ZIF-8_elec will be used for discussing diffusion of guest molecules in ZIF-8 in the following sections rather than ZIF-8_spin.

doi:10.6342/NTU202303887

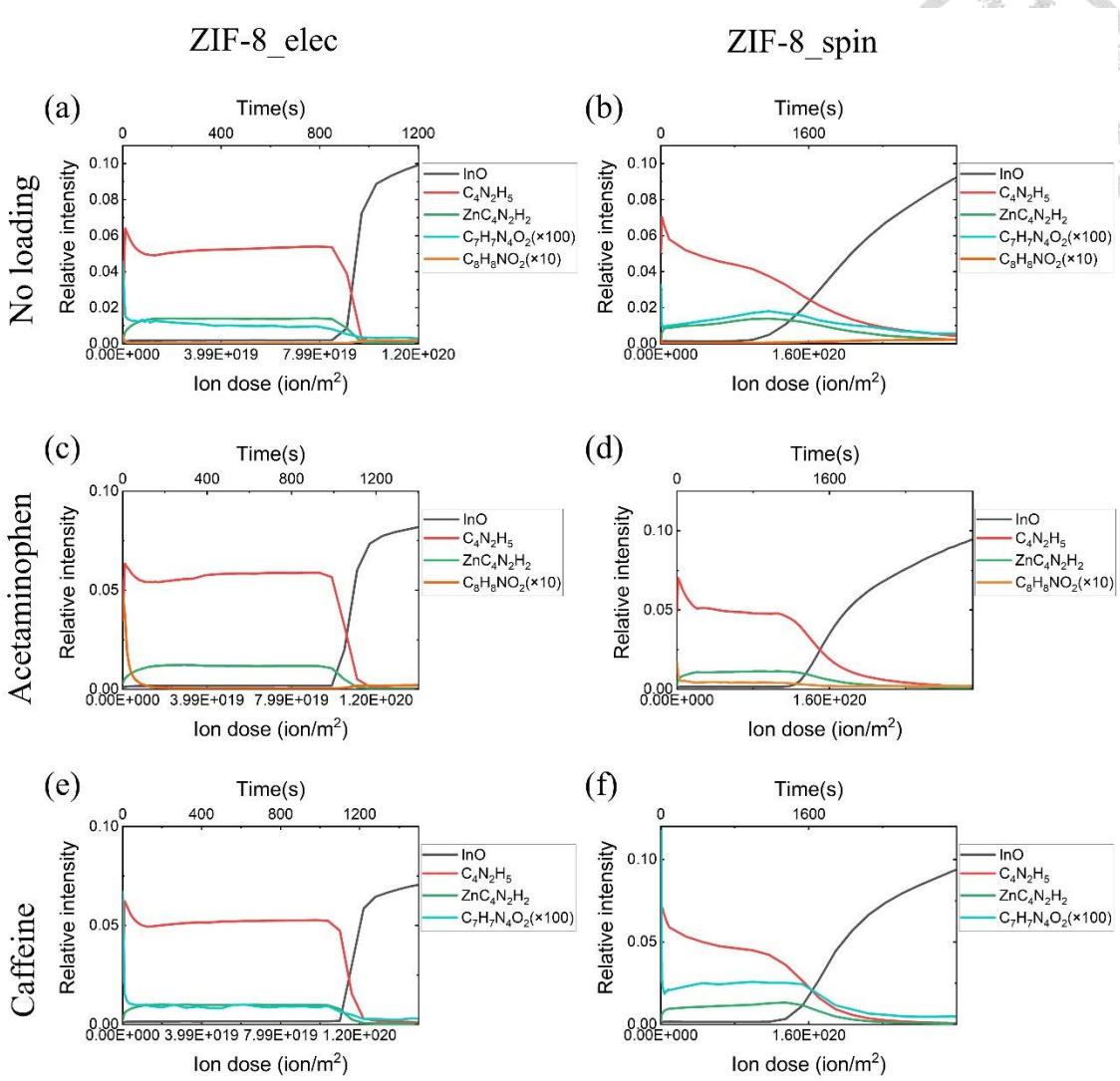

Figure 4.35 Depth profiles of (a) ZIF-8_elec, (b) ZIF-8_spin, (c) $ACE_{(EtOH)}$@ZIF-8_elec _24hr, (d) $ACE_{(EtOH)}$@ZIF-8_spin_24hr, (e) $CAF_{(EtOH)}$@ZIF-8_elec_24hr, and (f) $CAF_{(EtOH)}$@ZIF-8_spin _24hr.

The solution to Fick's second law with a fixed surface concentration was used to described the diffusion of model drugs in ZIF-8_elec in this research because the amount of acetaminophen entering the ZIF-8_elec is insignificant compared with the total, leading to a fixed concentration in the solution. The solution to Fick's second law with a

doi:10.6342/NTU202303887

fixed surface concentration has been solved and could be expressed as the following:

$$c(x,t) = c_s - (c_s - c_0)erf\left(\frac{x}{2\sqrt{Dt}}\right) \qquad \text{Eq 4.2}$$

where c is the concentration; x is the position; t is the time; c_s is the concentration at surface; c_0 is the concentration in the sample at $t = 0$; D is the effective diffusivity and *erf* is error function defined as:

$$erf(z) = \frac{2}{\sqrt{\pi}}\int_0^z e^{-y^2}dy \qquad \text{Eq 4.3}$$

The concentration profile of acetaminophen in $ACE_{(EtOH)}$@ZIF-8_elec _24hr was fitted to eq 4.2 using Origin 2018© and the result is shown in figure 4.36 and the effective diffusivity could be obtained to be $1.58 \pm 0.11 \times 10^{-21}$ m/s^2 with a coefficient value (R^2) of 0.98, indicating that the diffusion behavior could be described by this equation well.

doi:10.6342/NTU202303887

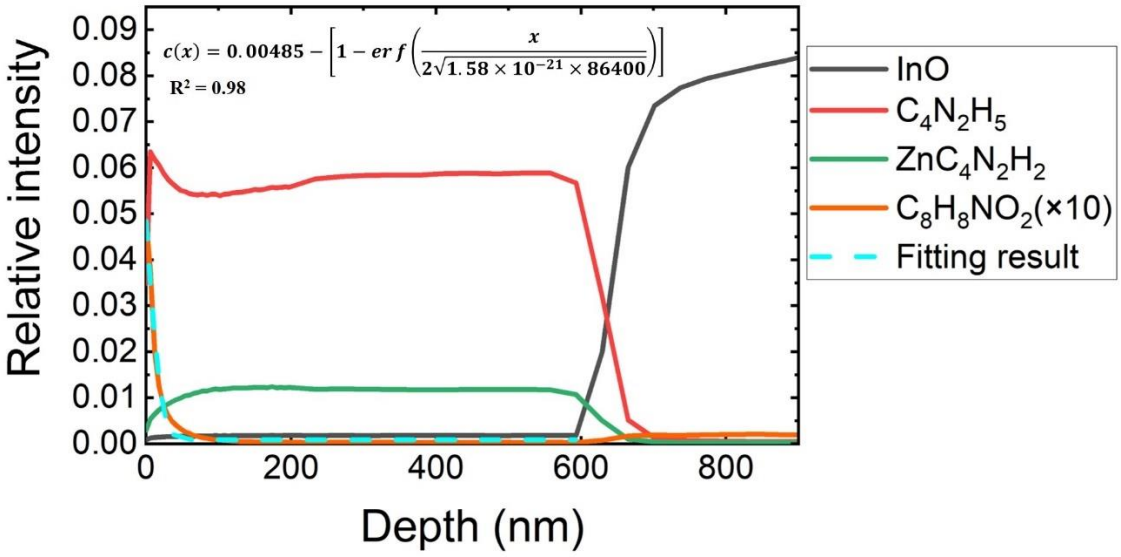

Figure 4.36 Fitting curve for $ACE_{(EtOH)}$@ZIF-8_elec _24hr.

Having established the research method for the diffusion in ZIF-8, different molecules, namely acetaminophen and caffeine, were compared to show the size effect of the guest molecules on diffusion in ZIF-8. Figure 4.37 shows the depth profiles of ZIF-8_elec immersed in 10 mM ethanolic solution of acetaminophen and caffeine for 24 hours respectively and the diffusivities were obtained by fitting to eq 4.2 for both profiles. While figure 4.37 (a) shows a diffusion profile of acetaminophen entering a depth about 100 nm, Figure 4.37 (b) shows increase of caffeine signal intensity only near the surface. Moreover, the diffusivities obtained for acetaminophen and caffeine in ZIF-8 by these two profiles are $1.58 \pm 0.11 \times 10^{-21}$ m/s^2 and $5.63 \pm 0.54 \times 10^{-23}$ m/s^2 respectively, indicating that diffusion of caffeine in ZIF-8 is much slower than diffusion of acetaminophen in ZIF-8. The fitting results are summarized in table 4.4 and more discussion would be made.

doi:10.6342/NTU202303887

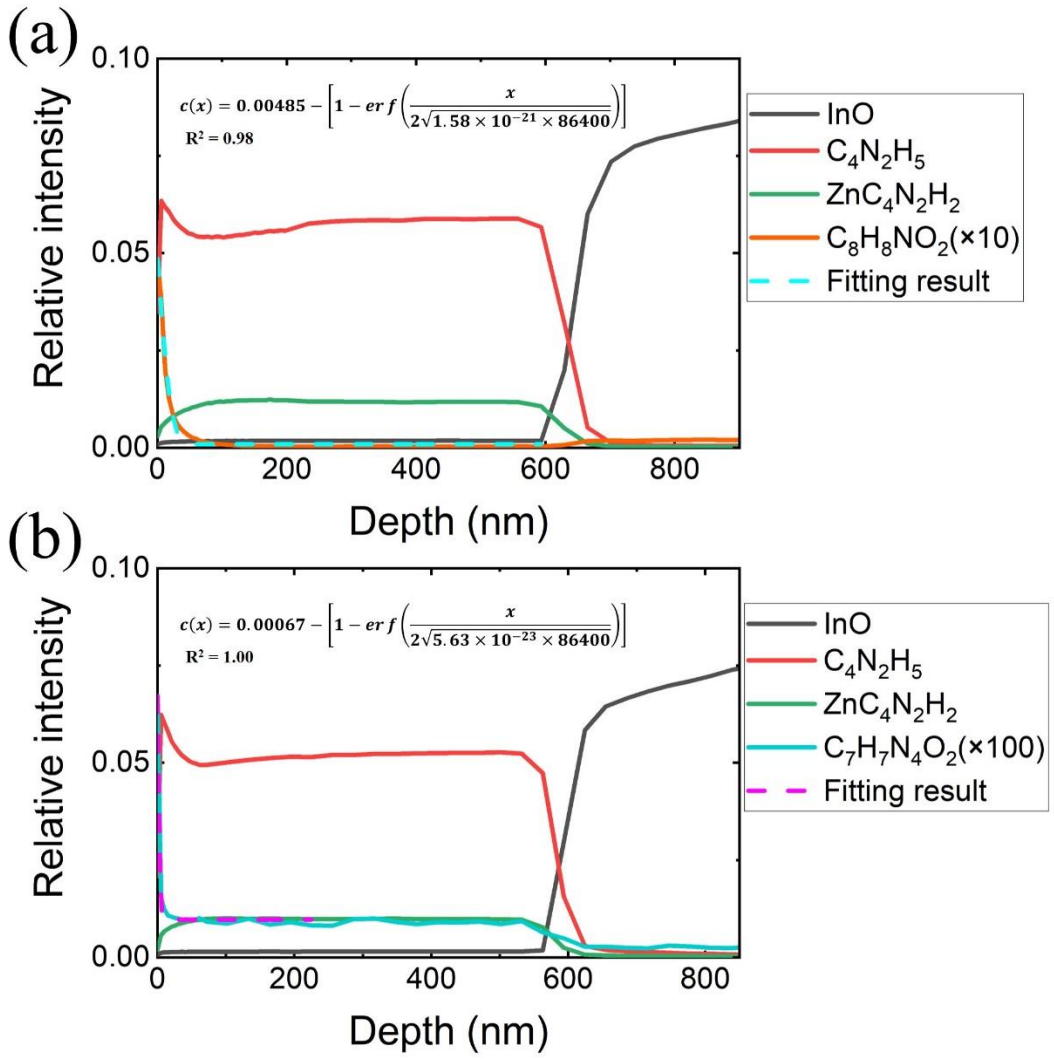

Figure 4.37 Depth profiles of (a) $ACE_{(EtOH)}$@ZIF-8_elec _24hr and (b) $CAF_{(EtOH)}$@ZIF-8_elec _24hr.

doi:10.6342/NTU202303887

Table 4.4 The obtained diffusivities and the residuals of the fitting results of ZIF-8_elec loaded with model drugs to Fick's diffusion with a fixed surface concentration.

Drug	Solvent	Time (hour)	Diffusivity (m/s^2)	R^2
Caffeine	Ethanol	24	$0.563 \pm 0.054 \times 10^{-22}$	1.00
Acetaminophen	Ethanol	24	$15.8 \pm 1.1 \times 10^{-22}$	0.98
Acetaminophen	DMF	24	$0.843 \pm 0.082 \times 10^{-22}$	0.99
Acetaminophen	Butanol	24	$4.17 \pm 0.4 \times 10^{-22}$	0.98

It is suggested to be due to the size of caffeine which has the dimension of 7.8 ×6.1 Å while acetaminophen has a longer length and a shorter width of 8.8 ×4.3 Å which are shown in figure 4.38. The slimmest dimension determines whether a molecule could enter ZIF-8 or not. It is because the pore size of ZIF-8 has been determined by XRD to be 11.6 Å, but ZIF-8 has a relatively small aperture size of 3.4 Å connecting between pores. The pore structure of ZIF-8 (figure 4.39) exhibited a large pore with a diameter of 11.6 Å enclosed inside with 3.4 Å apertures connecting between pores.[175] The 3.4 Å aperture has been reported to have flexibility and experiments have shown that the diffusivities of gas molecules across a range of sizes only decreased severely for molecules which were larger than 4.0 Å,[176] suggesting an effective aperture size of 4.0 to 4.2 Å. In this case, though both caffeine and acetaminophen could fit into the 11.6 Å pore of ZIF-8, only acetaminophen with a width of 4.3 Å could enter ZIF-8_elec while caffeine could not.

doi:10.6342/NTU202303887

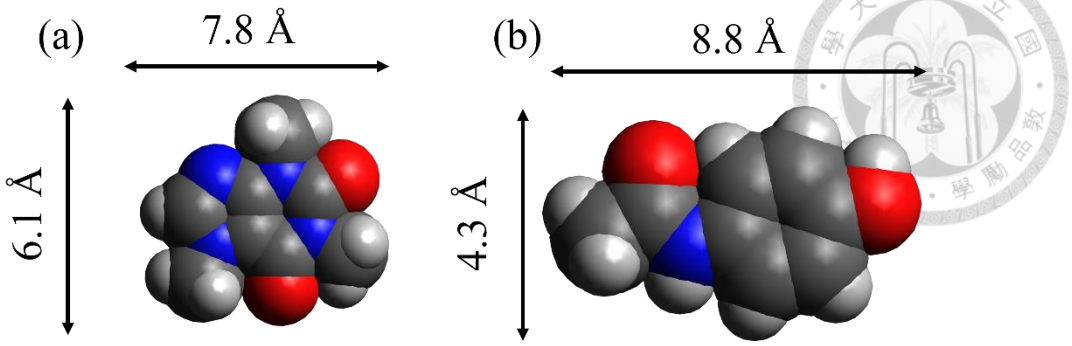

Figure 4.38 Dimensions of (a) caffeine and (b) acetaminophen.[163]

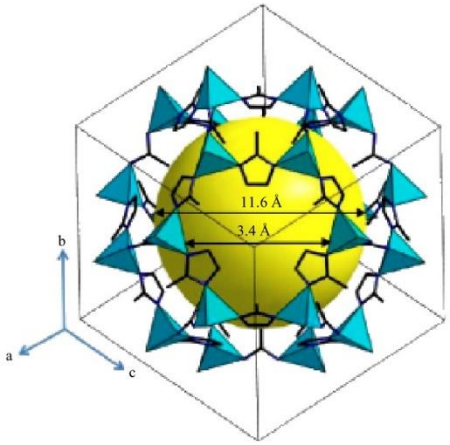

Figure 4.39 Illustration of the pore structure of ZIF-8 with a 11.6 Å pore and 3.4 Å apertures.[175]

Besides the size of model drug, the size of solvent also affected the diffusion in ZIF-8. Figure 4.40 shows depth profiles of ZIF-8_elec immersed in ethanolic and DMF solutions of acetaminophen for 24 hours respectively and the amount of acetaminophen entered ZIF-8_elec is obviously more in the ethanolic solution with a faster diffusivity of $1.58 \pm 0.11 \times 10^{-21}$ m/s^2 compared to $8.43 \pm 0.82 \times 10^{-23}$ m/s^2 in the DMF solution.

doi:10.6342/NTU202303887

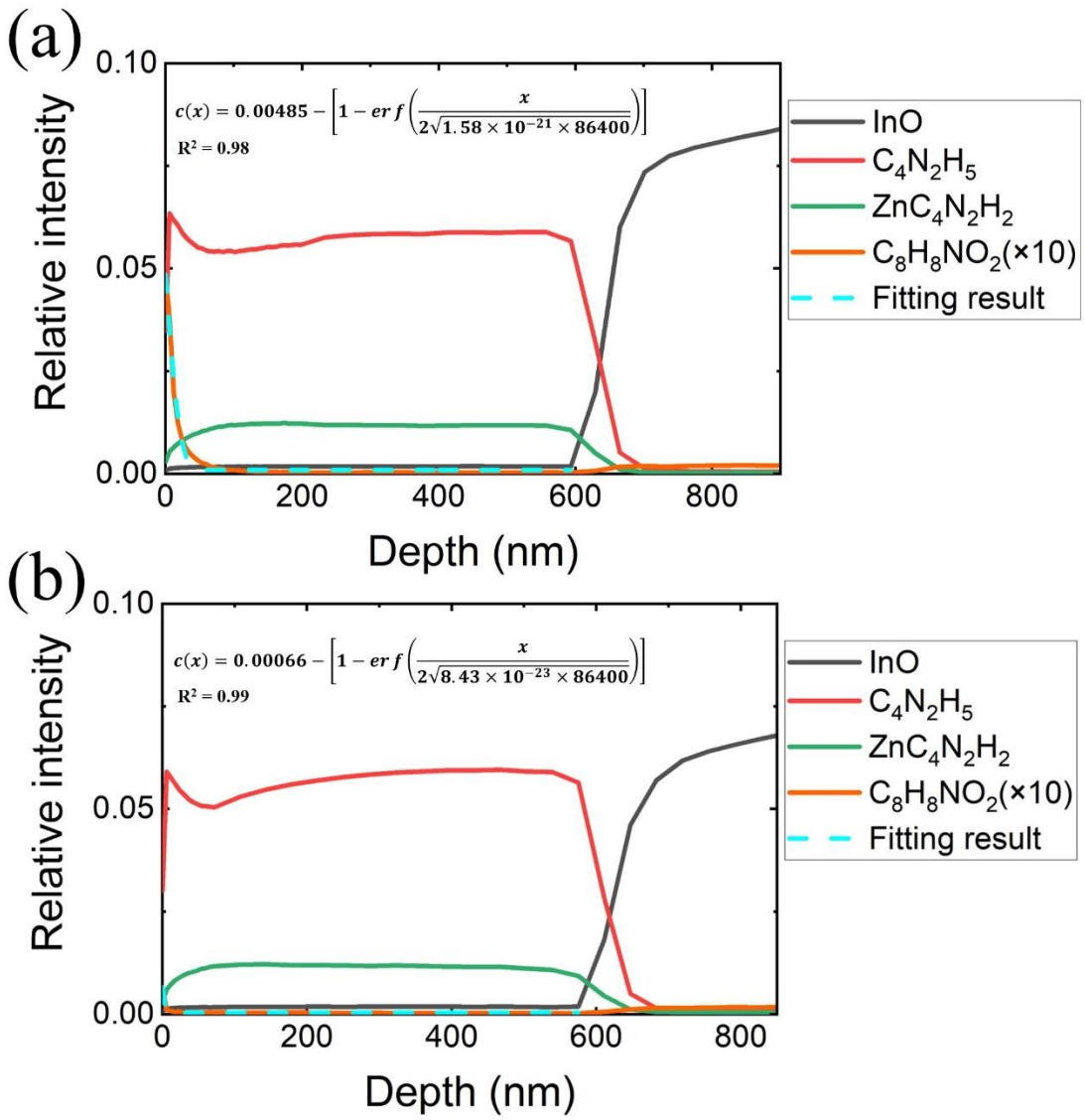

Figure 4.40 Depth profiles of (a) $ACE_{(EtOH)}$@ZIF-8_elec _24hr and (b) $ACE_{(DMF)}$@ZIF-8_elec _24hr.

doi:10.6342/NTU202303887

It is suggested that the larger size of DMF than ethanol obstruct the transfer of acetaminophen in ZIF-8. Therefore, butanol which has the same functional group of ethanol but a larger size was used as the solvent for further experiments. The concentration profile of acetaminophen using butanol as the solvent is shown in figure 4.41 (a) and a diffusivity of $4.17 \pm 0.40 \times 10^{-22}$ m/s^2 was obtained by fitting the profile to eq 4.2. The comparison of the profiles using ethanol, butanol and DMF is shown in figure 4.41 (b) and the value of the diffusivity using butanol as the solvent lies between the values using ethanol and DMF as the solvents, which also agrees with the molecular sizes of these three solvents. It further suggests that the choice of solvent affects diffusion in ZIF-8 where solvent with a larger molecular size tends to obstruct the diffusion in ZIF-8, resulting in a smaller diffusivity.

doi:10.6342/NTU202303887

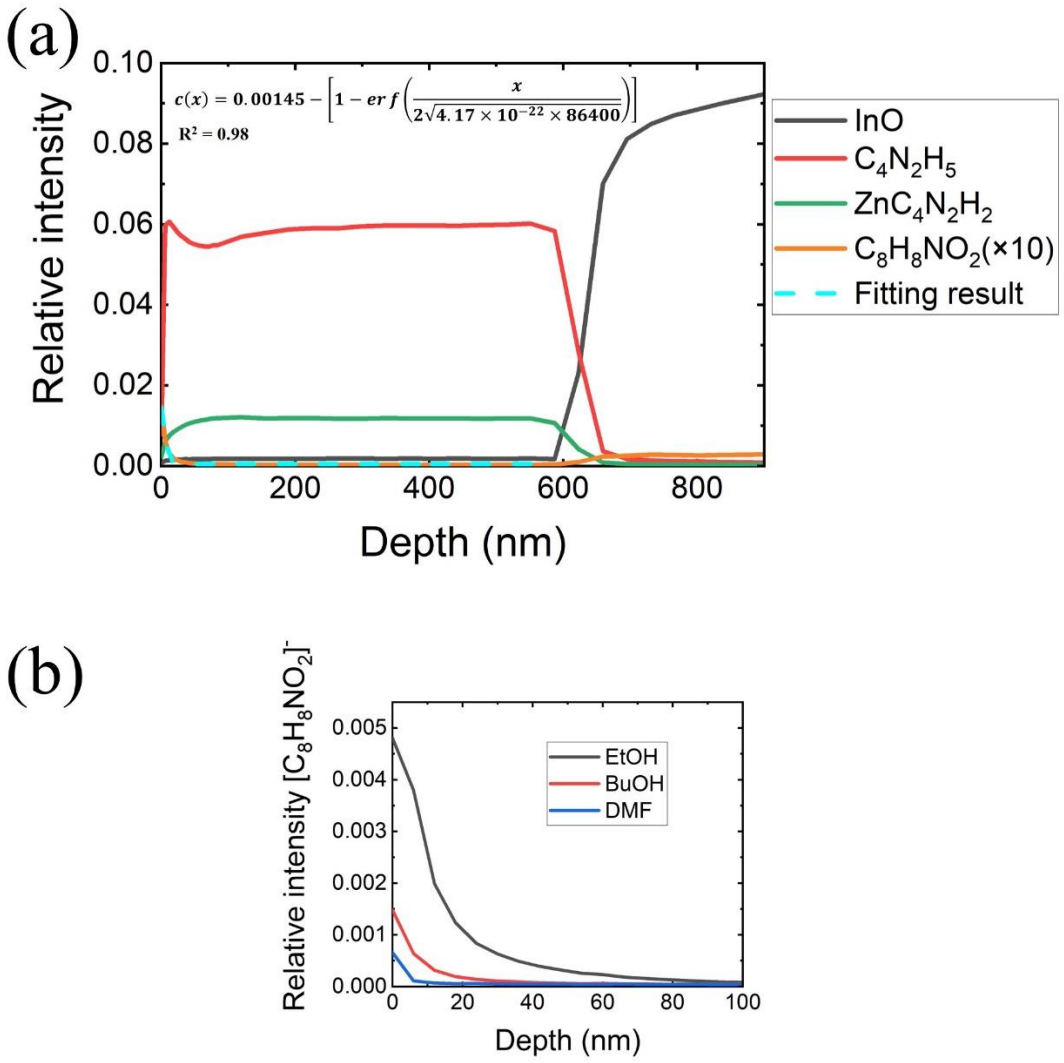

Figure 4.41 (a) Depth profiles of $ACE_{(BuOH)}$@ZIF-8_elec _24hr. (b) Comparison between concentration profiles of acetaminophen loaded in ZIF-8 using black: ethanol; red: butanol; blue: DMF as the solvents.

4.4.4 Summary

After knowing that GCIB is capable of sputtering ZIF-8 with an excellent sputter rate and preserving organic signal at the same time, we constructed depth profiles of ZIF-

doi:10.6342/NTU202303887

8 illustrating its chemical structure using ToF-SIMS with a slice-and-view scheme. In addition, model drugs including acetaminophen and caffeine were loaded into ZIF-8 thin film by immersing the ZIF-8 thin film in respective solution where solvents ranging from ethanol, butanol to DMF were used. The results showed concentration profiles of model drugs corresponding to the behavior of Fick's diffusion with a fixed surface concentration. The diffusivities were obtained by fitting and the results are shown in table 4.4. It could be seen that acetaminophen showed higher diffusivities than caffeine did because the smaller molecular size of acetaminophen makes it easier to enter ZIF-8. Furthermore, solvents with larger sizes show a tendency to obstruct the diffusion of drug molecules in ZIF-8, resulting in smaller diffusivities.

Chapter 5 Conclusion

In conclusion, this study utilized a range of techniques, including XRD, SEM, and SIMS, to determine the structure of a range of prepared MOFs. The prepared MOFs involved preparing ZIF-8 thin films by spin coating and cathodic deposition and preparing HKUST-1 in a 600 μm single crystal and in an 800 nm thin film. The results showed that these MOFs had been synthesized successfully in our lab with well-defined crystal structures and chemical compositions. The accessibility of these MOFs to depth profiling had also been examined. ZIF-8 showed easy accessibility to depth profiling using Ar-GCIB while HKUST-1 turned out to be challenging for all sputtering sources we had. The depth profile of HKUST-1 could not be constructed without losing all the organic signal.

This research also explored the potential of utilizing SIMS to directly determine the guest molecules distribution in MOFs. In this study, a protocol using depth profiles of guest molecules in ZIF-8, a popular metal-organic framework material, to determine the

doi:10.6342/NTU202303887

diffusivity by fitting to Fick's second law was established. It was found that size of the guest molecule, solvent used for the loading process, and morphology of the ZIF-8 thin film all contributed to diffusion in ZIF-8. As acetaminophen and caffeine were used as the model drugs in this study, only acetaminophen with the width of 4.3 Å was able to enter the 11.6 Å pores of ZIF-8 through the relatively small effective aperture size of 4.0 to 4.2 Å. The size of the solvent also affected diffusion in ZIF-8 in the way that acetaminophen showed a faster diffusion in ethanol than in DMF or butanol, which both have larger sizes than ethanol. Finally, the well-intergrown morphology of ZIF-8 thin film prepared by cathodic deposition prevented guest molecules entering through the space between ZIF-8 crystals, while ZIF-8 thin film prepared by spin coating allowed guest molecules moving freely in its less densely packed structure.

The findings of this study have important implications for the development of MOFs. This research reveals the prospect of examining distribution of molecules in MOFs and deducing the diffusion behavior of these molecules. By understanding the factors affecting diffusion in MOFs, researchers can design materials with a specific performance to selectively allow or prevent the diffusion of certain molecules. This could lead to the development of more efficient and selective materials for a wide range of applications including drug delivery.

In the future, molecules with a wider range of properties would be tested to uncover other factors affecting diffusion in MOFs. Other MOFs would be examine using this protocol to study how the inherent properties of MOFs affect diffusion in MOFs either. Moreover, it was found out that the distribution of different metallic nodes in the bimetallic ZIF thin film could also be determined using this protocol. A number of

doi:10.6342/NTU202303887

preliminary data was collected and shown in the appendix and the data show a great potential of revealing the nature of coordination process of bimetallic ZIF.

Overall, this research provides important insights into the behavior of guest molecules in ZIF-8 and lays the foundation for further studies on the design and development of MOFs.

doi:10.6342/NTU202303887

Chapter 6 Reference

(1) Rajkumar, T.; Kukkar, D.; Kim, K. H.; Sohn, J. R.; Deep, A.Cyclodextrin-Metal–Organic Framework (CD-MOF): From Synthesis to Applications. *J. Ind. Eng. Chem.* **2019**, *72*, 50–66. https://doi.org/10.1016/j.jiec.2018.12.048.

(2) Nadar, S. S.; Vaidya, L.; Maurya, S.; Rathod, V. K.Polysaccharide Based Metal Organic Frameworks (Polysaccharide–MOF): A Review. *Coord. Chem. Rev.* **2019**, *396*, 1–21. https://doi.org/10.1016/j.ccr.2019.05.011.

(3) Liu, C.; Wang, J.; Wan, J.; Yu, C.MOF-on-MOF Hybrids: Synthesis and Applications. *Coord. Chem. Rev.* **2021**, *432*, 213743. https://doi.org/10.1016/j.ccr.2020.213743.

(4) Amombo Noa, F. M.; Svensson Grape, E.; Brülls, S. M.; Cheung, O.; Malmberg, P.; Inge, A. K.; Mckenzie, C. J.; Mårtensson, J.; Öhrström, L.Metal-Organic Frameworks with Hexakis(4-Carboxyphenyl)Benzene: Extensions to Reticular Chemistry and Introducing Foldable Nets. *J. Am. Chem. Soc.* **2020**, *142* (20), 9471–9481. https://doi.org/10.1021/jacs.0c02984.

(5) Liu, R.; Xie, Y.; Cui, K.; Xie, J.; Zhang, Y.; Huang, Y.Adsorption Behavior and Adsorption Mechanism of Glyphosate in Water by Amino-MIL-101(Fe). *J. Phys. Chem. Solids* **2022**, *161* (September 2021), 110403. https://doi.org/10.1016/j.jpcs.2021.110403.

(6) Tanaka, S.; Fujita, K.; Miyake, Y.; Miyamoto, M.; Hasegawa, Y.; Makino, T.; Van DerPerre, S.; Cousin Saint Remi, J.; VanAssche, T.; Baron, G.V.; Denayer, J. F. M.Adsorption and Diffusion Phenomena in Crystal Size Engineered ZIF-8 MOF. *J. Phys. Chem. C* **2015**, *119* (51), 28430–28439. https://doi.org/10.1021/acs.jpcc.5b09520.

(7) Sabale, S.; Barpaga, D.; Yao, J.; Kovarik, L.; Zhu, Z.; Chatterjee, S.; McGrail, B. P.; Motkuri, R. K.; Yu, X. Y.Understanding Time Dependence on Zinc Metal-Organic Framework Growth Using in Situ Liquid Secondary Ion Mass Spectrometry-SI. *ACS Appl. Mater. Interfaces* **2020**, *12* (4), 5090–5098. https://doi.org/10.1021/acsami.9b19991.

(8) Noël, C.; Pescetelli, S.; Agresti, A.; Franquet, A.; Spampinato, V.; Felten, A.; diCarlo, A.; Houssiau, L.; Busby, Y.Hybrid Perovskites Depth Profiling with Variable-Size Argon Clusters and Monatomic Ions Beams. *Materials (Basel).* **2019**, *12* (5). https://doi.org/10.3390/ma12050726.

(9) Hou, C. H.; Hung, S. H.; Jhang, L. J.; Chou, K. J.; Hu, Y. K.; Chou, P. T.; Su, W. F.; Tsai, F. Y.; Shieh, J.; Shyue, J. J.Validated Analysis of Component Distribution Inside Perovskite Solar Cells and Its Utility in Unveiling Factors of

doi:10.6342/NTU202303887

Device Performance and Degradation. *ACS Appl. Mater. Interfaces* **2020**, *12* (20), 22730–22740. https://doi.org/10.1021/acsami.9b22492.

(10) Chiang, P.-H.Effect of Energy per Atom (E/n) in Ar Gas Cluster Ion Beam (Ar1000,2500+) with Ar+ Cosputter on Depth Profile of Metal-Organic Framework Thin Film by Secondary Ion Mass Spectroscopy, National Taiwan University, 2021. https://doi.org/10.6342/NTU202102598.

(11) Tovar, T. M.; Zhao, J.; Nunn, W. T.; Barton, H. F.; Peterson, G. W.; Parsons, G. N.; LeVan, M. D.Diffusion of CO2 in Large Crystals of Cu-BTC MOF. *J. Am. Chem. Soc.* **2016**, *138* (36), 11449–11452. https://doi.org/10.1021/jacs.6b05930.

(12) Mu, X.; Chen, Y.; Lester, E.; Wu, T.Optimized Synthesis of Nano-Scale High Quality HKUST-1 under Mild Conditions and Its Application in CO2 Capture. *Microporous Mesoporous Mater.* **2018**, *270* (January), 249–257. https://doi.org/10.1016/j.micromeso.2018.05.027.

(13) Liédana, N.; Galve, A.; Rubio, C.; Téllez, C.; Coronas, J.CAF@ZIF-8: One-Step Encapsulation of Caffeine in MOF. *ACS Appl. Mater. Interfaces* **2012**, *4* (9), 5016–5021. https://doi.org/10.1021/am301365h.

(14) Wei, R.; Chi, H. Y.; Li, X.; Lu, D.; Wan, Y.; Yang, C. W.; Lai, Z.Aqueously Cathodic Deposition of ZIF-8 Membranes for Superior Propylene/Propane Separation. *Adv. Funct. Mater.* **2020**, *30* (7), 1–7. https://doi.org/10.1002/adfm.201907089.

(15) Li, H.; Eddaoudi, M.; O'Keeffe, M.; Yaghi, O. M.Design and Synthesis of an Exceptionally Stable and Highly Porous Metal-Organic Framework. *Nature* **1999**, *402* (6759), 276–279. https://doi.org/10.1038/46248.

(16) Biradha, K.; Ramanan, A.; Vittal, J. J.Coordination Polymers Versus Metal−Organic Frameworks. *Cryst. Growth Des.* **2009**, *9* (7), 2969–2970. https://doi.org/10.1021/cg801381p.

(17) Abrahams, B. F.; Hoskins, B. F.; Robson, R.A New Type of Infinite 3D Polymeric Network Containing 4-Connected, Peripherally-Linked Metalloporphyrin Building Blocks. *J. Am. Chem. Soc.* **1991**, *113* (9), 3606–3607. https://doi.org/10.1021/ja00009a065.

(18) Yaghi, O. M.; Li, H.Hydrothermal Synthesis of a Metal-Organic Framework Containing Large Rectangular Channels. *J. Am. Chem. Soc.* **1995**, *117* (41), 10401–10402. https://doi.org/10.1021/ja00146a033.

(19) Chui, S. S. Y.; Lo, S. M. F.; Charmant, J. P. H.; Orpen, A. G.; Williams, I. D.A Chemically Functionalizable Nanoporous Material [Cu3(TMA)2 (H2O)3](N). *Science (80-.).* **1999**, *283* (5405), 1148–1150. https://doi.org/10.1126/science.283.5405.1148.

doi:10.6342/NTU202303887

(20) Serpaggi, F.; Férey, G.Hybrid Open Frameworks (MIL-n). Part 4 Synthesis and Crystal Structure of MIL-8, a Series of Lanthanide Glutarates with an Open Framework, [Ln(H2O)]2[O2C(CH2)3CO2]3·4H2O. *J. Mater. Chem.* **1998**, *8* (12), 2737–2741. https://doi.org/10.1039/a802713g.

(21) Serpaggi, F.; Férey, G.Hybrid Open Frameworks (MIL-n). Part 6 Hydrothermal Synthesis and X-Ray Powder Ab Initio Structure Determination of MIL-11, a Series of Lanthanide Organodiphosphonates with Three-Dimensional Networks, LnIIIH[O3P(CH2)NPO3] (N=1-3). *J. Mater. Chem.* **1998**, *8* (12), 2749–2755. https://doi.org/10.1039/a802715c.

(22) Livage, C.; Egger, C.; Nogues, M.; Férey, G.Hybrid Open Frameworks (MIL-n). Part 5 Synthesis and Crystal Structure of MIL-9: A New Three-Dimensional Ferrimagnetic Cobalt(II) Carboxylate with a Two-Dimensional Array of Edge-Sharing Co Octahedra with 12-Membered Rings. *J. Mater. Chem.* **1998**, *8* (12), 2743–2747. https://doi.org/10.1039/a802714e.

(23) Serre, C.; Férey, G.Hydrothermal Synthesis and Crystal Structure of a New Three-Dimensional Titanium(IV) Phosphate with an Open Structure: Ti6O3(H2O)3(PO4)7•(H3O)3•H2O or MIL-18. *Comptes Rendus l'Académie des Sci. - Ser. IIC - Chem.* **1999**, *2* (2), 85–91. https://doi.org/10.1016/S1387-1609(99)80006-1.

(24) Simon, N.; Loiseau, T.; Férey, G.Synthesis and Crystal Structure of MIL-14: A New Layered Fluoroaluminophosphate Templated with Tris(2-Aminoethylamine): Al2(HPO4)3F2·H2PO4·N4C6H21. *J. Mater. Chem.* **1999**, *9* (2), 585–589. https://doi.org/https://doi.org/10.1021/cm980781r.

(25) Livage, C.; Egger, C.; Férey, G.Hybrid Open Networks (MIL 16): Synthesis, Crystal Structure, and Ferrimagnetism of Co 4 (OH) 2 (H 2 O) 2 (C 4 H 4 O 4) 3 ·2H 2 O, a New Layered Cobalt(II) Carboxylate with 14-Membered Ring Channels. *Chem. Mater.* **1999**, *11* (6), 1546–1550. https://doi.org/10.1021/cm980781r.

(26) Faulet, C.; Serre, C.; Loiseau, T.; Riou, D.; Férey, G.Hybrid Open-Frameworks (MIL-n): Syntheses and Structures of 2-Dimensional Gallium Methylphosphonates (MIL-23) and 3-Dimensional Copper Vanadium Methyldiphosphonate (MIL-24). *Comptes Rendus l'Académie des Sci. - Ser. IIC - Chem.* **1999**, *2* (11–13), 631–636. https://doi.org/10.1016/S1387-1609(00)88576-X.

(27) Serpaggi, F.; Férey, G.Hybrid Organic-Inorganic Frameworks (MIL-n). Hydrothermal Synthesis of a Series of Pillared Lanthanide Carboxyethylphosphonates and x-Ray Powder Ab Initio Structure Determination

doi:10.6342/NTU202303887

of MIL-19, Pr[O3P(CH2)2CO2]. *Inorg. Chem.* **1999**, *38* (21), 4741–4744. https://doi.org/10.1021/ic981440i.

(28) Simon, N.; Loiseau, T.; Férey, G.Synthesis and Crystal Structure of MIL-27, a New Oxyfluorinated Three-Dimensional Framework Metallophosphate Obtained with Aluminium in Four, Five and Sixfold Coordination and Templated with the Tris(2-Aminoethyl)Amine. *Solid State Sci.* **1999**, *1* (6), 339–349. https://doi.org/10.1016/S1293-2558(00)80088-6.

(29) Serre, C.; Férey, G.Hydrothermal Synthesis, Structure Determination from Powder Data of a Three-Dimensional Zirconium Diphosphonate with an Exceptionally High Thermal Stability: Zr(O3P-(CH2)-PO3) or MIL-57. *J. Mater. Chem.* **2002**, *12* (8), 2367–2369. https://doi.org/10.1039/b202188a.

(30) Riou-Cavellec, M.; Férey, G.A New Three-Dimensional Iron Trimesate: [Fe3(H2O)5(C9 O6H3)2·3H2O] or MIL-65. *Solid State Sci.* **2002**, *4* (9), 1221–1225. https://doi.org/10.1016/S1293-2558(02)01381-X.

(31) Serpaggi, F.; Férey, G.Hybrid Open Frameworks (MIL-n): Synthesis and Crystal Structure of MIL-17 - A Rare-Earth Dicarboxylate with a Relatively Open Framework, [Pr(H2O)]2[O2C(CH2) 2CO2]3·H2O. *Microporous Mesoporous Mater.* **1999**, *32* (3), 311–318. https://doi.org/10.1016/S1387-1811(99)00120-1.

(32) Simon, N.; Loiseau, T.; Férey, G.Synthesis and Crystal Structure of MIL-32: A New Chiral Layered Aluminophosphate Templated with Non Chiral Tris(2-Aminoethyl)Amine: Al3(PO4)4, N4C6H21, H2O. *Solid State Sci.* **2000**, *2* (3), 391–397. https://doi.org/10.1016/s1293-2558(00)00142-4.

(33) Livage, C.; Egger, C.; Nogues, M.; Férey, G.Synthesis, Structural and Magnetic Characterisation of MIL 36, Co(C 7 H 10 O 4), a Three-Dimensional Coordination Polymer. *Comptes Rendus l'Académie des Sci. - Ser. IIC - Chem.* **2001**, *4* (3), 221–226. https://doi.org/10.1016/S1387-1609(00)01214-7.

(34) Riou-Cavellec, M.; Sanselme, M.; Grenèche, J.-M.; Férey, G.Hydrothermal Synthesis, Structural Approach, Magnetic and Mössbauer Study of the Layered Fe(III) Carboxyethylphosphonate [Fe(OH)(H2O)(O3P-(CH2)2-CO2H)] or MIL-37. *Solid State Sci.* **2000**, *2* (7), 717–724. https://doi.org/10.1016/S1293-2558(00)01080-3.

(35) Barthelet, K.; Jouve, C.; Riou, D.; Férey, G.Hybrid Open-Frameworks: Structure Determinations and Ferromagnetism of MIL-41 or (V(IV)O)2M(II)(H2O)4{HO3P-CH2-PO3}2 · 2H2O (M = MN, Co, Ni, Zn): Four Mixed Metallomethylendiphosphonates Hydrothermally Synthesized by Using Pre-Assembled Building Units. *Solid State Sci.* **2000**, *2* (8), 871–876. https://doi.org/10.1016/S1293-2558(00)01093-1.

doi:10.6342/NTU202303887

(36) Barthelet, K.; Riou, D.; Férey, G.Hydrothermal Synthesis and Structure Determination of Ag3(VvO2){O3P-CH2-PO 3} or MIL-42: A New Vanadium(V) Methylendiphosphonate Inserting Silver Cations. *Solid State Sci.* **2001**, *3* (1–2), 203–209. https://doi.org/10.1016/S1293-2558(00)01132-8.

(37) Serre, C.; Taulelle, F.; Ferey, G.Synthesis and Characterisation of MIL-43 and MIL-44, Two New Layered Templated Tetravalent Phosphates: Zr(PO4)2·N2C2H10 and Ti2(PO4)2(HPO4)2·N2C2H10. *Solid State Sci.* **2001**, *3* (5), 623–632. https://doi.org/10.1016/S1293-2558(01)01171-2.

(38) Serre, C.; Férey, G.Hydrothermal Synthesis and Structure Determination from Powder Data of New Three-Dimensional Titanium(IV) Diphosphonates Ti(O3P-(CH2)n-PO3) or MIL-25n (N=2, 3). *Inorg. Chem.* **2001**, *40* (21), 5350–5353. https://doi.org/10.1021/ic010260x.

(39) Riou-Cavellec, M.; Albinet, C.; Livage, C.; Guillou, N.; Noguès, M.; Grenèche, J. M.; Férey, G.Ferromagnetism of the Hybrid Open Framework K[M3(BTC)3]·5H2O (M = Fe, Co) or MIL-45. *Solid State Sci.* **2002**, *4* (2), 267–270. https://doi.org/10.1016/S1293-2558(01)01225-0.

(40) Riou-Cavellec, M.; Sanselme, M.; Noguès, M.; Grenèche, J.-M.; Férey, G.Synthesis, Structure and Metamagnetic Behaviour of a Three-Dimensional Fe(II) Carboxyethylphosphonate: [Fe3(OH)2(H2O)4(O3P (CH2)2 CO2H)2] or MIL-38. *Solid State Sci.* **2002**, *4* (5), 619–625. https://doi.org/10.1016/S1293-2558(02)01305-5.

(41) Barthelet, K.; Riou, D.; Férey, G.Hydrothermal Synthesis and Structure Determination of Na2Zn{O3P-CH2-PO3}.H2O (MIL-58): A New Zincomethylenediphosphonate Exhibiting a Hybrid Zeotype. *Solid State Sci.* **2002**, *4* (6), 841–844. https://doi.org/10.1016/S1293-2558(02)01331-6.

(42) Horcajada, P.; Serre, C.; Grosso, D.; Boissière, C.; Perruchas, S.; Sanchez, C.; Férey, G.Colloidal Route for Preparing Optical Thin Films of Nanoporous Metal-Organic Frameworks. *Adv. Mater.* **2009**, *21* (19), 1931–1935. https://doi.org/10.1002/adma.200801851.

(43) Serre, C.; Millange, F.; Thouvenot, C.; Noguès, M.; Marsolier, G.; Louër, D.; Férey, G.Very Large Breathing Effect in the First Nanoporous Chromium(III)-Based Solids: MIL-53 or CrIII(OH)·{O2C-C6H4- CO2}·{HO2C-C6H4 - CO2H}x·H2Oy. *J. Am. Chem. Soc.* **2002**, *124* (45), 13519–13526. https://doi.org/10.1021/ja0276974.

(44) Férey, C.; Mellot-Draznieks, C.; Serre, C.; Millange, F.; Dutour, J.; Surblé, S.; Margiolaki, I.Chemistry: A Chromium Terephthalate-Based Solid with Unusually Large Pore Volumes and Surface Area. *Science (80-.).* **2005**, *309*

doi:10.6342/NTU202303887

(5743), 2040–2042. https://doi.org/10.1126/science.1116275.

(45) Park, K. S.; Ni, Z.; Côté, A. P.; Choi, J. Y.; Huang, R.; Uribe-Romo, F. J.; Chae, H. K.; O'Keeffe, M.; Yaghi, O. M.Exceptional Chemical and Thermal Stability of Zeolitic Imidazolate Frameworks. *Proc. Natl. Acad. Sci. U. S. A.* **2006**, *103* (27), 10186–10191. https://doi.org/10.1073/pnas.0602439103.

(46) Cavka, J. H.; Jakobsen, S.; Olsbye, U.; Guillou, N.; Lamberti, C.; Bordiga, S.; Lillerud, K. P.A New Zirconium Inorganic Building Brick Forming Metal Organic Frameworks with Exceptional Stability. *J. Am. Chem. Soc.* **2008**, *130* (42), 13850–13851. https://doi.org/10.1021/ja8057953.

(47) Nabipour, H.; Mansoorianfar, M.; Hu, Y.Carboxymethyl Cellulose-Coated HKUST-1 for Baclofen Drug Delivery in Vitro. *Chem. Pap.* **2022**. https://doi.org/10.1007/s11696-022-02348-0.

(48) Alsaiari, S. K.; Patil, S.; Alyami, M.; Alamoudi, K. O.; Aleisa, F. A.; Merzaban, J. S.; Li, M.; Khashab, N. M.Endosomal Escape and Delivery of CRISPR/Cas9 Genome Editing Machinery Enabled by Nanoscale Zeolitic Imidazolate Framework. *J. Am. Chem. Soc.* **2018**, *140* (1), 143–146. https://doi.org/10.1021/jacs.7b11754.

(49) Jiang, K.; Ni, W.; Cao, X.; Zhang, L.; Lin, S.A Nanosized Anionic MOF with Rich Thiadiazole Groups for Controlled Oral Drug Delivery. *Mater. Today Bio* **2022**, *13* (December 2021), 100180. https://doi.org/10.1016/j.mtbio.2021.100180.

(50) Horcajada, P.; Gref, R.; Baati, T.; Allan, P. K.; Maurin, G.; Couvreur, P.Metal À Organic Frameworks in Biomedicine. **2012**, 1232–1268.

(51) Jodłowski, P. J.; Kurowski, G.; Skoczylas, N.; Pajdak, A.; Kudasik, M.; Jędrzejczyk, R. J.; Kuterasiński, Ł.; Jeleń, P.; Sitarz, M.; Li, A.; Mazur, M.Silver and Copper Modified Zeolite Imidazole Frameworks as Sustainable Methane Storage Systems. *J. Clean. Prod.* **2022**, *352* (March). https://doi.org/10.1016/j.jclepro.2022.131638.

(52) Sumida, K.; Rogow, D. L.; Mason, J. A.; McDonald, T. M.; Bloch, E. D.; Herm, Z. R.; Bae, T. H.; Long, J. R.Carbon Dioxide Capture in Metal-Organic Frameworks. *Chem. Rev.* **2012**, *112* (2), 724–781. https://doi.org/10.1021/cr2003272.

(53) Peng, X.; Chen, L.; Li, Y.Ordered Macroporous MOF-Based Materials for Catalysis. *Mol. Catal.* **2022**, *529* (July), 112568. https://doi.org/10.1016/j.mcat.2022.112568.

(54) Dhakshinamoorthy, A.; Garcia, H.Metal-Organic Frameworks as Solid Catalysts for the Synthesis of Nitrogen-Containing Heterocycles. *Chem. Soc. Rev.* **2014**, *43*

doi:10.6342/NTU202303887

(16), 5750–5765. https://doi.org/10.1039/c3cs60442j.

(55) Lee, J.; Farha, O. K.; Roberts, J.; Scheidt, K. A.; Nguyen, S. T.; Hupp, J. T.Metal-Organic Framework Materials as Catalysts. *Chem. Soc. Rev.* **2009**, *38* (5), 1450–1459. https://doi.org/10.1039/b807080f.

(56) Li, D.; Xu, F.Removal of Cu (II) from Aqueous Solutions Using ZIF-8@GO Composites. *J. Solid State Chem.* **2021**, *302* (May), 122406. https://doi.org/10.1016/j.jssc.2021.122406.

(57) Li, J. R.; Kuppler, R. J.; Zhou, H. C.Selective Gas Adsorption and Separation in Metal-Organic Frameworks. *Chem. Soc. Rev.* **2009**, *38* (5), 1477–1504. https://doi.org/10.1039/b802426j.

(58) Sepehrmansourie, H.; Alamgholiloo, H.; Noroozi Pesyan, N.; Zolfigol, M. A.A MOF-on-MOF Strategy to Construct Double Z-Scheme Heterojunction for High-Performance Photocatalytic Degradation. *Appl. Catal. B Environ.* **2023**, *321* (June 2022), 122082. https://doi.org/10.1016/j.apcatb.2022.122082.

(59) Chen, Q.; Ying, Y.; Wang, L.; Guo, Z.; Zhou, Y.; Wang, D.; Li, C.A Heterometallic MOF Based on Monofunctional Linker by "One-Pot" Solvothermal Method for Highly Selective Gas Adsorption. *Zeitschrift fur Anorg. und Allg. Chemie* **2020**, *646* (9), 437–443. https://doi.org/10.1002/zaac.201900325.

(60) McKinstry, C.; Cathcart, R. J.; Cussen, E. J.; Fletcher, A. J.; Patwardhan, S.V.; Sefcik, J.Scalable Continuous Solvothermal Synthesis of Metal Organic Framework (MOF-5) Crystals. *Chem. Eng. J.* **2016**, *285*, 718–725. https://doi.org/10.1016/j.cej.2015.10.023.

(61) Solís, R. R.; Peñas-Garzón, M.; Belver, C.; Rodriguez, J. J.; Bedia, J.Highly Stable UiO-66-NH2 by the Microwave-Assisted Synthesis for Solar Photocatalytic Water Treatment. *J. Environ. Chem. Eng.* **2022**, *10* (2). https://doi.org/10.1016/j.jece.2021.107122.

(62) Blanita, G.; Borodi, G.; Lazar, M. D.; Biris, A. R.; Barbu-Tudoran, L.; Coldea, I.; Lupu, D.Microwave Assisted Non-Solvothermal Synthesis of Metal-Organic Frameworks. *RSC Adv.* **2016**, *6* (31), 25967–25974. https://doi.org/10.1039/c5ra26097c.

(63) Li, X.; Dong, H.; Fan, Q.; Chen, K.; Sun, D.; Hu, T.; Ni, Z.One-Pot, Rapid Microwave-Assisted Synthesis of Bimetallic Metal–Organic Framework for Efficient Enzyme-Free Glucose Detection. *Microchem. J.* **2022**, *179* (April), 107468. https://doi.org/10.1016/j.microc.2022.107468.

(64) Wenger, S. R.; Kearns, E. R.; Miller, K. L.; D'Alessandro, D. M.Green, One-Step Mechanochemical Synthesis and Techno-Economic Analysis of UiO-66-

doi:10.6342/NTU202303887

NH2. *ACS Appl. Energy Mater.* **2022**. https://doi.org/10.1021/acsaem.2c02460.

(65) Chen, Y.; Wu, H.; Yuan, Y.; Lv, D.; Qiao, Z.; An, D.; Wu, X.; Liang, H.; Li, Z.; Xia, Q.Highly Rapid Mechanochemical Synthesis of a Pillar-Layer Metal-Organic Framework for Efficient CH4/N2 Separation. *Chem. Eng. J.* **2020**, *385* (October 2019), 123836. https://doi.org/10.1016/j.cej.2019.123836.

(66) Szczęśniak, B.; Borysiuk, S.; Choma, J.; Jaroniec, M.Mechanochemical Synthesis of Highly Porous Materials. *Mater. Horizons* **2020**, *7* (6), 1457–1473. https://doi.org/10.1039/D0MH00081G.

(67) Han, S.; Wei, Y.; Valente, C.; Lagzi, I.; Gassensmith, J. J.; Coskun, A.; Stoddart, J. F.; Grzybowski, B. A.Chromatography in a Single Metal-Organic Framework (MOF) Crystal. *J. Am. Chem. Soc.* **2010**, *132* (46), 16358–16361. https://doi.org/10.1021/ja1074322.

(68) Han, S.; Hermans, T. M.; Fuller, P. E.; Wei, Y.; Grzybowski, B. A.Transport into Metal-Organic Frameworks from Solution Is Not Purely Diffusive. *Angew. Chemie - Int. Ed.* **2012**, *51* (11), 2662–2666. https://doi.org/10.1002/anie.201108492.

(69) Li, L.; Sun, F.; Jia, J.; Borjigin, T.; Zhu, G.Growth of Large Single MOF Crystals and Effective Separation of Organic Dyes. *CrystEngComm* **2013**, *15* (20), 4094–4098. https://doi.org/10.1039/c3ce40137e.

(70) Kwon, O.; Kim, J. Y.; Park, S.; Lee, J. H.; Ha, J.; Park, H.; Moon, H. R.; Kim, J.Computer-Aided Discovery of Connected Metal-Organic Frameworks. *Nat. Commun.* **2019**, *10* (1), 1–8. https://doi.org/10.1038/s41467-019-11629-4.

(71) Shekhah, O.; Liu, J.; Fischer, R. A.; Wöll, C.MOF Thin Films: Existing and Future Applications. *Chem. Soc. Rev.* **2011**, *40* (2), 1081–1106. https://doi.org/10.1039/c0cs00147c.

(72) Norrman, K.; Ghanbari-Siahkali, A.; Larsen, N. B.6 Studies of Spin-Coated Polymer Films. *Annu. Reports Sect. "C" (Physical Chem.* **2005**, *101*, 174. https://doi.org/10.1039/b408857n.

(73) Huang, Y.; Tao, C. A.; Chen, R.; Sheng, L.; Wang, J.Comparison of Fabrication Methods of Metal-Organic Framework Optical Thin Films. *Nanomaterials* **2018**, *8* (9), 1–20. https://doi.org/10.3390/nano8090676.

(74) Liu, B.; Fischer, R. A.Liquid-Phase Epitaxy of Metal Organic Framework Thin Films. *Sci. China Chem.* **2011**, *54* (12), 1851–1866. https://doi.org/10.1007/s11426-011-4406-8.

(75) Shekhah, O.; Wang, H.; Zacher, D.; Fischer, R. A.; Wöll, C.Growth Mechanism of Metal-Organic Frameworks: Insights into the Nucleation by Employing a Step-by-Step Route. *Angew. Chemie Int. Ed.* **2009**, *48* (27), 5038–5041.

doi:10.6342/NTU202303887

https://doi.org/10.1002/anie.200900378.

(76) Zheng, R.; Fu, Z.; Deng, W.; Wen, Y.; Wu, A.; Ye, X.The Growth Mechanism of a Conductive MOF Thin Film in Spray- Based Layer-by-Layer Liquid Phase Epitaxy. **2022**, *100049*. https://doi.org/10.1002/anie.202212797.

(77) Ohnsorg, M. L.; Beaudoin, C. K.; Anderson, M. E.Fundamentals of MOF Thin Film Growth via Liquid-Phase Epitaxy: Investigating the Initiation of Deposition and the Influence of Temperature. *Langmuir* **2015**, *31* (22), 6114–6121. https://doi.org/10.1021/acs.langmuir.5b01333.

(78) Nijem, N.; Fürsich, K.; Kelly, S. T.; Swain, C.; Leone, S. R.; Gilles, M. K.HKUST-1 Thin Film Layer-by-Layer Liquid Phase Epitaxial Growth: Film Properties and Stability Dependence on Layer Number. *Cryst. Growth Des.* **2015**, *15* (6), 2948–2957. https://doi.org/10.1021/acs.cgd.5b00384.

(79) Shekhah, O.; Wang, H.; Kowarik, S.; Schreiber, F.; Paulus, M.; Tolan, M.; Sternemann, C.; Evers, F.; Zacher, D.; Fischer, R. A.; Wöll, C.Step-by-Step Route for the Synthesis of Metal−Organic Frameworks. *J. Am. Chem. Soc.* **2007**, *129* (49), 15118–15119. https://doi.org/10.1021/ja076210u.

(80) Shekhah, O.; Eddaoudi, M.The Liquid Phase Epitaxy Method for the Construction of Oriented ZIF-8 Thin Films with Controlled Growth on Functionalized Surfaces. *Chem. Commun.* **2013**, *49* (86), 10079–10081. https://doi.org/10.1039/c3cc45343j.

(81) Cookney, J.; Ogieglo, W.; Hrabanek, P.; Vankelecom, I.; Fila, V.; Benes, N. E.Dynamic Response of Ultrathin Highly Dense ZIF-8 Nanofilms. *Chem. Commun.* **2014**, *50* (79), 11698–11700. https://doi.org/10.1039/c4cc04754k.

(82) Shekhah, O.; Swaidan, R.; Belmabkhout, Y.; DuPlessis, M.; Jacobs, T.; Barbour, L. J.; Pinnau, I.; Eddaoudi, M.The Liquid Phase Epitaxy Approach for the Successful Construction of Ultra-Thin and Defect-Free ZIF-8 Membranes: Pure and Mixed Gas Transport Study. *Chem. Commun.* **2014**, *50* (17), 2089–2092. https://doi.org/10.1039/c3cc47495j.

(83) Valadez Sánchez, E. P.; Gliemann, H.; Haas-Santo, K.; Wöll, C.; Dittmeyer, R.ZIF-8 SURMOF Membranes Synthesized by Au-Assisted Liquid Phase Epitaxy for Application in Gas Separation. *Chemie-Ingenieur-Technik* **2016**, *88* (11), 1798–1805. https://doi.org/10.1002/cite.201600061.

(84) Valadez Sánchez, E. P.; Gliemann, H.; Haas-Santo, K.; Ding, W.; Hansjosten, E.; Wohlgemuth, J.; Wöll, C.; Dittmeyer, R.α-Al2O3-Supported ZIF-8 SURMOF Membranes: Diffusion Mechanism of Ethene/Ethane Mixtures and Gas Separation Performance. *J. Memb. Sci.* **2020**, *594* (July 2019), 117421. https://doi.org/10.1016/j.memsci.2019.117421.

doi:10.6342/NTU202303887

(85) Chernikova, V.; Shekhah, O.; Eddaoudi, M.Advanced Fabrication Method for the Preparation of MOF Thin Films: Liquid-Phase Epitaxy Approach Meets Spin Coating Method. *ACS Appl. Mater. Interfaces* **2016**, *8* (31), 20459–20464. https://doi.org/10.1021/acsami.6b04701.

(86) Semrau, A. L.; Wannapaiboon, S.; Pujari, S. P.; Vervoorts, P.; Albada, B.; Zuilhof, H.; Fischer, R. A.Highly Porous Nanocrystalline UiO-66 Thin Films via Coordination Modulation Controlled Step-by-Step Liquid-Phase Growth. *Cryst. Growth Des.* **2019**, *19* (3), 1738–1747. https://doi.org/10.1021/acs.cgd.8b01719.

(87) Li, M.; Dincă, M.Reductive Electrosynthesis of Crystalline Metal-Organic Frameworks. *J. Am. Chem. Soc.* **2011**, *133* (33), 12926–12929. https://doi.org/10.1021/ja2041546.

(88) He, G.; Dakhchoune, M.; Zhao, J.; Huang, S.; Agrawal, K. V.Electrophoretic Nuclei Assembly for Crystallization of High-Performance Membranes on Unmodified Supports. *Adv. Funct. Mater.* **2018**, *28* (20), 1–8. https://doi.org/10.1002/adfm.201707427.

(89) Zhou, S.; Wei, Y.; Li, L.; Duan, Y.; Hou, Q.; Zhang, L.; Ding, L. X.; Xue, J.; Wang, H.; Caro, J.Paralyzed Membrane: Current-Driven Synthesis of a Metal-Organic Framework with Sharpened Propene/Propane Separation. *Sci. Adv.* **2018**, *4* (10), 1–9. https://doi.org/10.1126/sciadv.aau1393.

(90) Xie, S.; Monnens, W.; Wan, K.; Zhang, W.; Guo, W.; Xu, M. W.; Vankelecom, I. F. J.; Zhang, X.; Fransaer, J.Cathodic Electrodeposition of MOF Films Using Hydrogen Peroxide. *Angew. Chemie - Int. Ed.* **2021**, *60* (47), 24950–24957. https://doi.org/10.1002/anie.202108485.

(91) Warfsmann, J.; Tokay, B.; Champness, N. R.Synthesis of MIL-53 Thin Films by Vapour-Assisted Conversion. *CrystEngComm* **2020**, *22* (6), 1009–1017. https://doi.org/10.1039/c9ce01644a.

(92) Mahringer, A.; Jakowetz, A. C.; Rotter, J. M.; Bohn, B. J.; Stolarczyk, J. K.; Feldmann, J.; Bein, T.; Medina, D. D.Oriented Thin Films of Electroactive Triphenylene Catecholate-Based Two-Dimensional MetalOrganic Frameworks. *ACS Nano* **2019**, *13* (6), 6711–6719. https://doi.org/10.1021/acsnano.9b01137.

(93) Shi, Q.; Chen, Z.; Song, Z.; Li, J.; Dong, J.Synthesis of ZIF-8 and ZIF-67 by Steam-Assisted Conversion and an Investigation of Their Tribological Behaviors. *Angew. Chemie - Int. Ed.* **2011**, *50* (3), 672–675. https://doi.org/10.1002/anie.201004937.

(94) Zhang, H.; Shi, Q.; Kang, X.; Dong, J.Vapor-Assisted Conversion Synthesis of Prototypical Zeolitic Imidazolate Framework-8. *J. Coord. Chem.* **2013**, *66* (12), 2079–2090. https://doi.org/10.1080/00958972.2013.797966.

doi:10.6342/NTU202303887

(95) Virmani, E.; Rotter, J. M.; Mähringer, A.; VonZons, T.; Godt, A.; Bein, T.; Wuttke, S.; Medina, D. D.On-Surface Synthesis of Highly Oriented Thin Metal-Organic Framework Films through Vapor-Assisted Conversion. *J. Am. Chem. Soc.* **2018**, *140* (14), 4812–4819. https://doi.org/10.1021/jacs.7b08174.

(96) Scheurle, P. I.; Mähringer, A.; Biewald, A.; Hartschuh, A.; Bein, T.; Medina, D. D.MOF-74(M) Films Obtained through Vapor-Assisted Conversion - Impact on Crystal Orientation and Optical Properties. *Chem. Mater.* **2021**, *33* (15), 5896–5904. https://doi.org/10.1021/acs.chemmater.1c00743.

(97) Kim, K. J.; Culp, J. T.; Ohodnicki, P. R.; Thallapally, P. K.; Tao, J.Synthesis of High-Quality Mg-MOF-74 Thin Films via Vapor-Assisted Crystallization. *ACS Appl. Mater. Interfaces* **2021**, *13* (29), 35223–35231. https://doi.org/10.1021/acsami.1c12000.

(98) Li, C.; Wang, J.; Wang, Y.; Gao, H.; Wei, G.; Huang, Y.; Yu, H.; Gan, Y.; Wang, Y.; Mei, L.; Chen, H.; Hu, H.; Zhang, Z.; Jin, Y.Recent Progress in Drug Delivery. *Acta Pharm. Sin. B* **2019**, *9* (6), 1145–1162. https://doi.org/10.1016/j.apsb.2019.08.003.

(99) He, S.; Wu, L.; Li, X.; Sun, H.; Xiong, T.; Liu, J.; Huang, C.; Xu, H.; Sun, H.; Chen, W.; Gref, R.; Zhang, J.Metal-Organic Frameworks for Advanced Drug Delivery. *Acta Pharm. Sin. B* **2021**, *11* (8), 2362–2395. https://doi.org/10.1016/j.apsb.2021.03.019.

(100) Large, D. E.; Abdelmessih, R. G.; Fink, E. A.; Auguste, D. T.Liposome Composition in Drug Delivery Design, Synthesis, Characterization, and Clinical Application. *Adv. Drug Deliv. Rev.* **2021**, *176*, 113851. https://doi.org/10.1016/j.addr.2021.113851.

(101) Kotta, S.; Aldawsari, H. M.; Badr-Eldin, S. M.; Nair, A. B.; YT, K.Progress in Polymeric Micelles for Drug Delivery Applications. *Pharmaceutics* **2022**, *14* (8), 1–32. https://doi.org/10.3390/pharmaceutics14081636.

(102) Wang, J.; Li, B.; Qiu, L.; Qiao, X.; Yang, H.Dendrimer-Based Drug Delivery Systems: History, Challenges, and Latest Developments. *J. Biol. Eng.* **2022**, *16* (1), 1–12. https://doi.org/10.1186/s13036-022-00298-5.

(103) Tan, E.; Wan, T.; Yu, C.; Fan, Q.; Liu, W.; Chang, H.; Lv, J.; Wang, H.; Li, D.; Ping, Y.; Cheng, Y.ROS-Responsive Polypeptides for Intracellular Protein Delivery and CRISPR/Cas9 Gene Editing. *Nano Today* **2022**, *46*, 101617. https://doi.org/10.1016/j.nantod.2022.101617.

(104) Jakubowski, M.; Kucinska, M.; Ratajczak, M.; Pokora, M.; Murias, M.; Voelkel, A.; Sandomierski, M.Zinc Forms of Faujasite Zeolites as a Drug Delivery System for 6-Mercaptopurine. *Microporous Mesoporous Mater.* **2022**, *343* (March),

doi:10.6342/NTU202303887

112194. https://doi.org/10.1016/j.micromeso.2022.112194.

(105) Wang, Y.; Yan, J.; Wen, N.; Xiong, H.; Cai, S.; He, Q.; Hu, Y.; Peng, D.; Liu, Z.; Liu, Y.Metal-Organic Frameworks for Stimuli-Responsive Drug Delivery. *Biomaterials* **2020**, *230* (June 2019), 119619. https://doi.org/10.1016/j.biomaterials.2019.119619.

(106) Horcajada, P.; Serre, C.; Vallet-Regí, M.; Sebban, M.; Taulelle, F.; Férey, G.Metal-Organic Frameworks as Efficient Materials for Drug Delivery. *Angew. Chemie - Int. Ed.* **2006**, *45* (36), 5974–5978. https://doi.org/10.1002/anie.200601878.

(107) Horcajada, P.; Chalati, T.; Serre, C.; Gillet, B.; Sebrie, C.; Baati, T.; Eubank, J. F.; Heurtaux, D.; Clayette, P.; Kreuz, C.; Chang, J. S.; Hwang, Y. K.; Marsaud, V.; Bories, P. N.; Cynober, L.; Gil, S.; Férey, G.; Couvreur, P.; Gref, R.Porous Metal-Organic-Framework Nanoscale Carriers as a Potential Platform for Drug Deliveryand Imaging. *Nat. Mater.* **2010**, *9* (2), 172–178. https://doi.org/10.1038/nmat2608.

(108) Zheng, H.; Zhang, Y.; Liu, L.; Wan, W.; Guo, P.; Nyström, A. M.; Zou, X.One-Pot Synthesis of Metal-Organic Frameworks with Encapsulated Target Molecules and Their Applications for Controlled Drug Delivery. *J. Am. Chem. Soc.* **2016**, *138* (3), 962–968. https://doi.org/10.1021/jacs.5b11720.

(109) Gautam, S.; Singhal, J.; Lee, H. K.; Chae, K. H.Drug Delivery of Paracetamol by Metal-Organic Frameworks (HKUST-1): Improvised Synthesis and Investigations. *Mater. Today Chem.* **2022**, *23*, 100647. https://doi.org/10.1016/j.mtchem.2021.100647.

(110) Karimzadeh, Z.; Javanbakht, S.; Namazi, H.Carboxymethylcellulose/MOF-5/Graphene Oxide Bio-Nanocomposite as Antibacterial Drug Nanocarrier Agent. *BioImpacts* **2018**, *9* (1), 5–13. https://doi.org/10.15171/bi.2019.02.

(111) Li, Z.; Zhao, S.; Wang, H.; Peng, Y.; Tan, Z.; Tang, B.Functional Groups Influence and Mechanism Research of UiO-66-Type Metal-Organic Frameworks for Ketoprofen Delivery-SI. *Colloids Surfaces B Biointerfaces* **2019**, *178*, 1–7. https://doi.org/10.1016/j.colsurfb.2019.02.027.

(112) Ke, F.; Yuan, Y. P.; Qiu, L. G.; Shen, Y. H.; Xie, A. J.; Zhu, J. F.; Tian, X. Y.; Zhang, L.De.Facile Fabrication of Magnetic Metal-Organic Framework Nanocomposites for Potential Targeted Drug Delivery. *J. Mater. Chem.* **2011**, *21* (11), 3843–3848. https://doi.org/10.1039/c0jm01770a.

(113) Akbar, M. U.; Badar, M.; Zaheer, M.Programmable Drug Release from a Dual-Stimuli Responsive Magnetic Metal-Organic Framework. *ACS Omega* **2022**, *7* (36), 32588–32598. https://doi.org/10.1021/acsomega.2c04144.

doi:10.6342/NTU202303887

(114) Sharp, C. H.; Bukowski, B. C.; Li, H.; Johnson, E. M.; Ilic, S.; Morris, A. J.; Gersappe, D.; Snurr, R. Q.; Morris, J. R.Nanoconfinement and Mass Transport in Metal-Organic Frameworks. *Chem. Soc. Rev.* **2021**, *50* (20), 11530–11558. https://doi.org/10.1039/d1cs00558h.

(115) Stallmach, F.; Gröger, S.; Künzel, V.; Kärger, J.; Yaghi, O. M.; Hesse, M.; Müller, U.NMR Studies on the Diffusion of Hydrocarbons on the Metal-Organic Framework Material MOF-5. *Angew. Chemie - Int. Ed.* **2006**, *45* (13), 2123–2126. https://doi.org/10.1002/anie.200502553.

(116) Song, J.; Liu, L.; Hong, Y.High Interfacial Resistances of CH4 and CO2 Transport through Metal-Organic Framework 5 (MOF-5). *Sep. Purif. Technol.* **2022**, *301* (June), 121895. https://doi.org/10.1016/j.seppur.2022.121895.

(117) Zybaylo, O.; Shekhah, O.; Wang, H.; Tafipolsky, M.; Schmid, R.; Johannsmann, D.; Wöll, C.A Novel Method to Measure Diffusion Coefficients in Porous Metal-Organic Frameworks. *Phys. Chem. Chem. Phys.* **2010**, *12* (28), 8092–8097. https://doi.org/10.1039/b927601g.

(118) Tuninetti, J. S.; Rafti, M.; Andrieu-Brunsen, A.; Azzaroni, O.Molecular Transport Properties of ZIF-8 Thin Films in Aqueous Environments: The Critical Role of Intergrain Mesoporosity as Diffusional Pathway. *Microporous Mesoporous Mater.* **2016**, *220*, 253–257. https://doi.org/10.1016/j.micromeso.2015.08.035.

(119) Stassin, T.; Verbeke, R.; Cruz, A. J.; Rodríguez-Hermida, S.; Stassen, I.; Marreiros, J.; Krishtab, M.; Dickmann, M.; Egger, W.; Vankelecom, I. F. J.; Furukawa, S.; DeVos, D.; Grosso, D.; Thommes, M.; Ameloot, R.Porosimetry for Thin Films of Metal–Organic Frameworks: A Comparison of Positron Annihilation Lifetime Spectroscopy and Adsorption-Based Methods. *Adv. Mater.* **2021**, *2006993*, 1–14. https://doi.org/10.1002/adma.202006993.

(120) Wagner, A.; Pullen, S.; Ott, S.; Primetzhofer, D.The Potential of Ion Beams for Characterization of Metal-Organic Frameworks. *Nucl. Instruments Methods Phys. Res. Sect. B Beam Interact. with Mater. Atoms* **2016**, *371*, 327–331. https://doi.org/10.1016/j.nimb.2015.10.059.

(121) Yan, J.; Carl, A. D.; Maag, A. R.; MacDonald, J. C.; Müller, P.; Grimm, R. L.; Burdette, S. C.Detection of Adsorbates on Emissive MOF Surfaces with X-Ray Photoelectron Spectroscopy. *Dalt. Trans.* **2019**, *48* (14), 4520–4529. https://doi.org/10.1039/C8DT04404J.

(122) Chang, H. Y.; Lin, W. C.; Chu, P. C.; Wang, Y. K.; Sogo, M.; Iida, S. I.; Peng, C. J.; Miyayama, T.X-Ray Photoelectron Spectroscopy Equipped with Gas Cluster Ion Beams for Evaluation of the Sputtering Behavior of Various Nanomaterials.

doi:10.6342/NTU202303887

ACS Appl. Nano Mater. **2022**, *5* (3), 4260–4268. https://doi.org/10.1021/acsanm.2c00202.

(123) Chehreh Chelgani, S.; Hart, B.TOF-SIMS Studies of Surface Chemistry of Minerals Subjected to Flotation Separation - A Review. *Miner. Eng.* **2014**, *57*, 1–11. https://doi.org/10.1016/j.mineng.2013.12.001.

(124) Lee, J. C.; Won, J.; Chung, Y.; Lee, H.; Lee, E.; Kang, D.; Kim, C.; Choi, J.; Kim, J.Investigations of Semiconductor Devices Using SIMS; Diffusion, Contamination, Process Control. *Appl. Surf. Sci.* **2008**, *255* (4), 1395–1399. https://doi.org/10.1016/j.apsusc.2008.06.129.

(125) Aoyagi, S.Review of TOF-SIMS Bioanalysis Using Mutual Information. *Surf. Interface Anal.* **2009**, *41* (2), 136–142. https://doi.org/10.1002/sia.2989.

(126) Glish, G. L.; Vachet, R. W.The Basics of Mass Spectrometry in the Twenty-First Century. *Nat. Rev. Drug Discov.* **2003**, *2* (2), 140–150. https://doi.org/10.1038/nrd1011.

(127) Buckner, C. A.; Lafrenie, R. M.; Dénommée, J. A.; Caswell, J. M.; Want, D. A.; Gan, G. G.; Leong, Y. C.; Bee, P. C.; Chin, E.; Teh, A. K. H.; Picco, S.; Villegas, L.; Tonelli, F.; Merlo, M.; Rigau, J.; Diaz, D.; Masuelli, M.; Korrapati, S.; Kurra, P.; Puttugunta, S.; Picco, S.; Villegas, L.; Tonelli, F.; Merlo, M.; Rigau, J.; Diaz, D.; Masuelli, M.; Tascilar, M.; deJong, F. A.; Verweij, J.; Mathijssen, R. H. J.*Mass Spectrometry*; Aliofkhazraei, M., Ed.; InTech, 2017; Vol. 11. https://doi.org/10.5772/65165.

(128) Griffiths, J.A Brief History of Mass Spectrometry. *Anal. Chem.* **2008**, *80* (15), 5678–5683. https://doi.org/10.1021/ac8013065.

(129) Dole, M.; Mack, L. L.; Hines, R. L.; Mobley, R. C.; Ferguson, L. D.; Alice, M. B.Molecular Beams of Macroions. *J. Chem. Phys.* **1968**, *49* (5), 2240–2249. https://doi.org/10.1063/1.1670391.

(130) An, Z.; Zhang, Z.; Zhang, X.; Yang, H.; Lu, H.; Liu, M.; Shao, Y.; Zhao, X.; Zhang, H.Oligosaccharide Mapping Analysis by HILIC-ESI-HCD-MS/MS for Structural Elucidation of Fucoidan from Sea Cucumber Holothuria Floridana. *Carbohydr. Polym.* **2022**, *275* (August 2021), 118694. https://doi.org/10.1016/j.carbpol.2021.118694.

(131) Wan, J.; He, P.; Chen, Y.; Zhu, Q.Comprehensive Target Analysis for 19 Pyrethroids in Tea and Orange Samples Based on LC-ESI-QqQ-MS/MS and LC-ESI-Q-ToF/MS. *Lwt* **2021**, *151* (July), 112072. https://doi.org/10.1016/j.lwt.2021.112072.

(132) Zhong, B.; Robinson, N. A.; Warner, R. D.; Barrow, C. J.; Dunshea, F. R.; Suleria, H. A. R.LC-ESI-QTOF-MS/MS Characterization of Seaweed Phenolics

doi:10.6342/NTU202303887

and Their Antioxidant Potential. *Mar. Drugs* **2020**, *18* (6), 1–21. https://doi.org/10.3390/md18060331.

(133) Karas, M.; Bachmann, D.; Hillenkamp, F.Influence of the Wavelength in High-Irradiance Ultraviolet Laser Desorption Mass Spectrometry of Organic Molecules. *Anal. Chem.* **1985**, *57* (14), 2935–2939. https://doi.org/10.1021/ac00291a042.

(134) McMillen, J. C.; Gutierrez, D. B.; Judd, A. M.; Spraggins, J. M.; Caprioli, R. M.Enhancement of Tryptic Peptide Signals from Tissue Sections Using MALDI IMS Postionization (MALDI-2). *J. Am. Soc. Mass Spectrom.* **2021**, *32* (10), 2583–2591. https://doi.org/10.1021/jasms.1c00213.

(135) McMillen, J. C.; Fincher, J. A.; Klein, D. R.; Spraggins, J. M.; Caprioli, R. M.Effect of MALDI Matrices on Lipid Analyses of Biological Tissues Using MALDI-2 Postionization Mass Spectrometry. *J. Mass Spectrom.* **2020**, *55* (12). https://doi.org/10.1002/jms.4663.

(136) Hertel Pereira, A. C.; Auer, A. C.; Biedel, L.; deAlmeida, C. M.; Romão, W.; Endringer, D. C.Analysis of Gliricidia Sepium Leaves by MALDI Mass Spectrometry Imaging. *J. Am. Soc. Mass Spectrom.* **2022**, *33* (3), 573–583. https://doi.org/10.1021/jasms.1c00367.

(137) *Atomic and Ion Collisions in Solids and at Surfaces*; Smith, R., Ed.; Cambridge University Press, 1997. https://doi.org/10.1017/CBO9780511524325.

(138) Benninghoven, A.The Development of SIMS and International SIMS Conferences: A Personal Retrospective View. *Surf. Interface Anal.* **2011**, *43* (1–2), 2–11. https://doi.org/10.1002/sia.3688.

(139) van derHeide, P.*Secondary Ion Mass Spectrometry*; John Wiley & Sons, Inc.: Hoboken, NJ, USA, 2014; Vol. 15. https://doi.org/10.1002/9781118916780.

(140) DeSouza, R. A.; Martin, M.Secondary Ion Mass Spectrometry (SIMS) - a Powerful Tool for Studying Mass Transport over Various Length Scales. *Phys. Status Solidi Curr. Top. Solid State Phys.* **2007**, *4* (6), 1785–1801. https://doi.org/10.1002/pssc.200675227.

(141) Woodcock, K. S.The Emission of Negative Ions under the Bombardment of Positive Ions. *Phys. Rev.* **1931**, *38* (9), 1696–1703. https://doi.org/10.1103/PhysRev.38.1696.

(142) Thompson, J. S.A New Method of Producing Negative Ions. *Phys. Rev.* **1931**, *38* (7), 1389–1389. https://doi.org/10.1103/PhysRev.38.1389.

(143) Herzog, R. F. K.; Viehböck, F. P.Ion Source for Mass Spectrography. *Phys. Rev.* **1949**, *76* (6), 855–856. https://doi.org/10.1103/PhysRev.76.855.

(144) Benninghoven, A.Die Analyse Monomolekularer

doi:10.6342/NTU202303887

Festkörperoberflächenschichten Mit Hilfe Der Sekundärionenemission - The Analysis of Monomolecular Layers of Solids by Secondary Ion Emission. *Zeitschrift für Phys. A Hadron. Nucl.* **1970**, *230* (5), 403–417.

(145) Chait, B. T.; Standing, K. G.A Time-of-Flight Mass Spectrometer for Measurement of Secondary Ion Mass Spectra. *Int. J. Mass Spectrom. Ion Phys.* **1981**, *40* (2), 185–193. https://doi.org/10.1016/0020-7381(81)80041-1.

(146) Appelhans, A. D.; Delmore, J. E.Comparison of Polyatomic and Atomic Primary Beams for Secondary Ion Mass Spectrometry of Organics. *Anal. Chem.* **1989**, *61* (10), 1087–1093. https://doi.org/10.1021/ac00185a009.

(147) Davies, N.; Weibel, D. E.; Blenkinsopp, P.; Lockyer, N.; Hill, R.; Vickerman, J. C.Development and Experimental Application of a Gold Liquid Metal Ion Source. *Appl. Surf. Sci.* **2003**, *203–204*, 223–227. https://doi.org/10.1016/S0169-4332(02)00631-1.

(148) Sun, S.; Szakal, C.; Roll, T.; Mazarov, P.; Wucher, A.; Winograd, N.Use of C60 Cluster Projectiles for Sputter Depth Profiling of Polycrystalline Metals. *Surf. Interface Anal.* **2004**, *36* (10), 1367–1372. https://doi.org/10.1002/sia.1923.

(149) Toyoda, N.; Matsuo, J.; Aoki, T.; Yamada, I.; Fenner, D. B.Secondary Ion Mass Spectrometry with Gas Cluster Ion Beams. *Nucl. Instruments Methods Phys. Res. Sect. B Beam Interact. with Mater. Atoms* **2002**, *190* (1–4), 860–864. https://doi.org/10.1016/S0168-583X(02)00463-9.

(150) Bertrand, P.; Weng, L.Time-of-Flight Secondary Ion Mass Spectrometry. **1996**, *182*, 167–182.

(151) Vickerman, J. C.Impact of Mass Spectrometry in Surface Analysis. *Analyst* **1994**, *119* (4), 513–523. https://doi.org/10.1039/AN9941900513.

(152) Ogaki, R.; Green, F. M.; Li, S.; Vert, M.; Alexander, M. R.; Gilmore, I. S.; Davies, M. C.A Comparison of the Static SIMS and G-SIMS Spectra of Biodegradable Homo-Polyesters. *Surf. Interface Anal.* **2008**, *40* (8), 1202–1208. https://doi.org/10.1002/sia.2866.

(153) Urbini, M.; Petito, V.; deNotaristefani, F.; Scaldaferri, F.; Gasbarrini, A.; Tortora, L.ToF-SIMS and Principal Component Analysis of Lipids and Amino Acids from Inflamed and Dysplastic Human Colonic Mucosa. *Anal. Bioanal. Chem.* **2017**, *409* (26), 6097–6111. https://doi.org/10.1007/s00216-017-0546-9.

(154) Kennedy, A. K.; Wotzlaw, J. F.; Crowley, J. L.; Schmitz, M.; Schaltegger, U.; Wade, B.; Martin, L.; Talavera, C.; Ware, B.; Bui, T. H.Apatite Reference Materials for SIMS Microanalysis of Isotopes and Trace Elements. *Geostand. Geoanalytical Res.* **2022**, No. 4, 1–30. https://doi.org/10.1111/ggr.12477.

(155) Gardner, W.; Winkler, D. A.; Maliki, R.; Cutts, S. M.; Ellis, S.; Anderson, R. L.;

doi:10.6342/NTU202303887

Muir, B. W.; Pigram, P. J.Fusing ToF-SIMS Images for Spatial-Spectral Resolution Enhancement Using a Convolutional Neural Network. *Adv. Mater. Interfaces* **2022**, *9* (34). https://doi.org/10.1002/admi.202201464.

(156) Passarelli, M. K.; Pirkl, A.; Moellers, R.; Grinfeld, D.; Kollmer, F.; Havelund, R.; Newman, C. F.; Marshall, P. S.; Arlinghaus, H.; Alexander, M. R.; West, A.; Horning, S.; Niehuis, E.; Makarov, A.; Dollery, C. T.; Gilmore, I. S.The 3D OrbiSIMS - Label-Free Metabolic Imaging with Subcellular Lateral Resolution and High Mass-Resolving Power. *Nat. Methods* **2017**, *14* (12), 1175–1183. https://doi.org/10.1038/nmeth.4504.

(157) Schroder, K.; Alvarado, J.; Yersak, T. A.; Li, J.; Dudney, N.; Webb, L. J.; Meng, Y. S.; Stevenson, K. J.The Effect of Fluoroethylene Carbonate as an Additive on the Solid Electrolyte Interphase on Silicon Lithium-Ion Electrodes. *Chem. Mater.* **2015**, *27* (16), 5531–5542. https://doi.org/10.1021/acs.chemmater.5b01627.

(158) Dass, C.*Fundamentals of Contemporary Mass Spectrometry*; John Wiley & Sons, Inc.: Hoboken, NJ, USA, 2007; Vol. 45. https://doi.org/10.1002/0470118490.

(159) Yakovenko, A. A.; Reibenspies, J. H.; Bhuvanesh, N.; Zhou, H.-C.Generation and Applications of Structure Envelopes for Porous Metal–Organic Frameworks. *J. Appl. Crystallogr.* **2013**, *46* (2), 346–353. https://doi.org/10.1107/S0021889812050935.

(160) Karagiaridi, O.; Lalonde, M. B.; Bury, W.; Sarjeant, A. A.; Farha, O. K.; Hupp, J. T.Opening ZIF-8: A Catalytically Active Zeolitic Imidazolate Framework of Sodalite Topology with Unsubstituted Linkers. *J. Am. Chem. Soc.* **2012**, *134* (45), 18790–18796. https://doi.org/10.1021/ja308786r.

(161) Zhang, C.; Han, C.; Sholl, D. S.; Schmidt, J. R.Computational Characterization of Defects in Metal-Organic Frameworks: Spontaneous and Water-Induced Point Defects in ZIF-8. *J. Phys. Chem. Lett.* **2016**, *7* (3), 459–464. https://doi.org/10.1021/acs.jpclett.5b02683.

(162) Han, C.; Zhang, C.; Tymińska, N.; Schmidt, J. R.; Sholl, D. S.Insights into the Stability of Zeolitic Imidazolate Frameworks in Humid Acidic Environments from First-Principles Calculations. *J. Phys. Chem. C* **2018**, *122* (8), 4339–4348. https://doi.org/10.1021/acs.jpcc.7b12058.

(163) Kim, S.; Chen, J.; Cheng, T.; Gindulyte, A.; He, J.; He, S.; Li, Q.; Shoemaker, B. A.; Thiessen, P. A.; Yu, B.; Zaslavsky, L.; Zhang, J.; Bolton, E. E.PubChem in 2021: New Data Content and Improved Web Interfaces. *Nucleic Acids Res.* **2021**, *49* (D1), D1388–D1395. https://doi.org/10.1093/nar/gkaa971.

(164) Pines, D.; Ditkovich, J.; Mukra, T.; Miller, Y.; Kiefer, P. M.; Daschakraborty, S.; Hynes, J. T.; Pines, E.How Acidic Is Carbonic Acid? *J. Phys. Chem. B* **2016**, *120*

doi:10.6342/NTU202303887

(9), 2440–2451. https://doi.org/10.1021/acs.jpcb.5b12428.
(165) Harvey, S. P.; Zhang, F.; Palmstrom, A.; Luther, J. M.; Zhu, K.; Berry, J. J.Mitigating Measurement Artifacts in TOF-SIMS Analysis of Perovskite Solar Cells. *ACS Appl. Mater. Interfaces* **2019**, *11* (34), 30911–30918. https://doi.org/10.1021/acsami.9b09445.
(166) Cheng, J.; Wucher, A.; Winograd, N.Molecular Depth Profiling with Cluster Ion Beams. *J. Phys. Chem. B* **2006**, *110* (16), 8329–8336. https://doi.org/10.1021/jp0573341.
(167) Chen, Y. Y.; Yu, B. Y.; Wang, W.Ben; Hsu, M. F.; Lin, W. C.; Lin, Y. C.; Jou, J. H.; Shyue, J. J.X-Ray Photoelectron Spectrometry Depth Profiling of Organic Thin Films Using C60 Sputtering. *Anal. Chem.* **2008**, *80* (2), 501–505. https://doi.org/10.1021/ac701899a.
(168) Postawa, Z.Sputtering Simulations of Organic Overlayers on Metal Substrates by Monoatomic and Clusters Projectiles. *Appl. Surf. Sci.* **2004**, *231–232*, 22–28. https://doi.org/10.1016/j.apsusc.2004.03.019.
(169) Miyazaki, S.; Ishitani, M.; Takahashi, A.; Shimoyama, T.; Itoh, K.; Attwood, D.Carrageenan Gels for Oral Sustained Delivery of Acetaminophen to Dysphagic Patients. *Biol. Pharm. Bull.* **2011**, *34* (1), 164–166. https://doi.org/10.1248/bpb.34.164.
(170) Zhang, J.; Xu, P.; Vo, A. Q.; Repka, M. A.Oral Drug Delivery Systems Using Core-Shell Structure Additive Manufacturing Technologies: A Proof-of-Concept Study. *J. Pharm. Pharmacol.* **2021**, *73* (2), 152–160. https://doi.org/10.1093/jpp/rgaa037.
(171) Laska, E. M.Caffeine as an Analgesic Adjuvant. *JAMA J. Am. Med. Assoc.* **1984**, *251* (13), 1711. https://doi.org/10.1001/jama.1984.03340370043028.
(172) Lipton, R. B.; Stewart, W. F.; Ryan, R. E.; Saper, J.; Silberstein, S.; Sheftell, F.Efficacy and Safety of Acetaminophen, Aspirin, and Caffeine in Alleviating Migraine Headache Pain. *Arch. Neurol.* **1998**, *55* (2), 210. https://doi.org/10.1001/archneur.55.2.210.
(173) Renner, B.; Clarke, G.; Grattan, T.; Beisel, A.; Mueller, C.; Werner, U.; Kobal, G.; Brune, K.Caffeine Accelerates Absorption and Enhances the Analgesic Effect of Acetaminophen. *J. Clin. Pharmacol.* **2007**, *47* (6), 715–726. https://doi.org/10.1177/0091270007299762.
(174) Zhang, P.; Xu, P.; Chung, S.; Bandari, S.; Repka, M. A.Fabrication of Bilayer Tablets Using Hot Melt Extrusion-Based Dual-Nozzle Fused Deposition Modeling 3D Printing. *Int. J. Pharm.* **2022**, *624* (June), 121972. https://doi.org/10.1016/j.ijpharm.2022.121972.

doi:10.6342/NTU202303887

(175) Sze Lai, L.; Fong Yeong, Y.; Keong Lau, K.; Shariff Az, M.Zeolite Imidazole Frameworks Membranes for CO2/CH4 Separation from Natural Gas: A Review. *J. Appl. Sci.* **2014**, *14* (11), 1161–1167. https://doi.org/10.3923/jas.2014.1161.1167.

(176) Zhang, C.; Lively, R. P.; Zhang, K.; Johnson, J. R.; Karvan, O.; Koros, W. J.Unexpected Molecular Sieving Properties of Zeolitic Imidazolate Framework-8. *J. Phys. Chem. Lett.* **2012**, *3* (16), 2130–2134. https://doi.org/10.1021/jz300855a.

doi:10.6342/NTU202303887

Appendix. Depth profile of bimetallic ZIF

ToF-SIMS analysis is not only capable of assessing drug molecules in ZIF-8 thin film, but also capable of assessing different metallic nodes in a bimetallic ZIF system. It has been shown above that $[ZnC_4N_2H_2]^-$ represents metallic nodes in ZIF-8 thin film, so it is reasonable to suggest that $[CoC_4N_2H_2]^-$ should be detected at m/z = 137 which could then represent the Co^{2+} coordinated by 2-mIm in the bimetallic ZIF system. Figure A.1 shows the mass spectrum of a bimetallic ZIF thin film synthesized with a molar ratio of Zn^{2+} : Co^{2+} as 1 : 1 and a prominent peak at m/z = 137 could be seen. There is no naturally occurred stable isotope of Co other than ^{59}Co on earth, so it is not feasible to confirm if the peak at m/z = 137 is $[CoC_4N_2H_2]^-$ by matching the abundance of its isotopes. Nonetheless, figure A.2 (a) shows that the exact mass of the peak matches the exact of $[CoC_4N_2H_2]^-$ well (136.955 Da). Moreover, the peak at m/z = 111 shows a prominent intensity and its exact mass is shown in figure A.2 (b) which perfectly matches with the exact mass of $[CoC_3NH_2]^-$ (110.952 Da), meaning that it is also a reasonable fragment representing Co^{2+} coordinated by 2-mIm in the bimetallic ZIF thin film. Nevertheless, $[CoC_4N_2H_2]^-$ was used to represent the Co^{2+} containing nodes in the bimetallic ZIF thin film because it directly corresponded to a Co^{2+} coordinated by a 2-mIm and the similar fragment containing Zn^{2+} was also used to represent the Zn^{2+} containing nodes in the bimetallic ZIF thin film.

doi:10.6342/NTU202303887

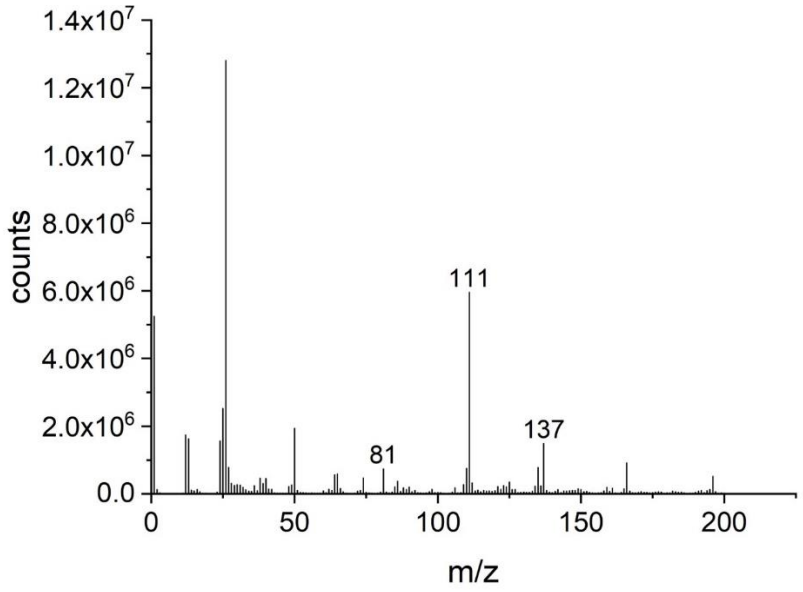

Figure A.1 Mass spectrum of the bimetallic ZIF thin film synthesized with a molar ratio of Zn^{2+} : Co^{2+} as 1 : 1.

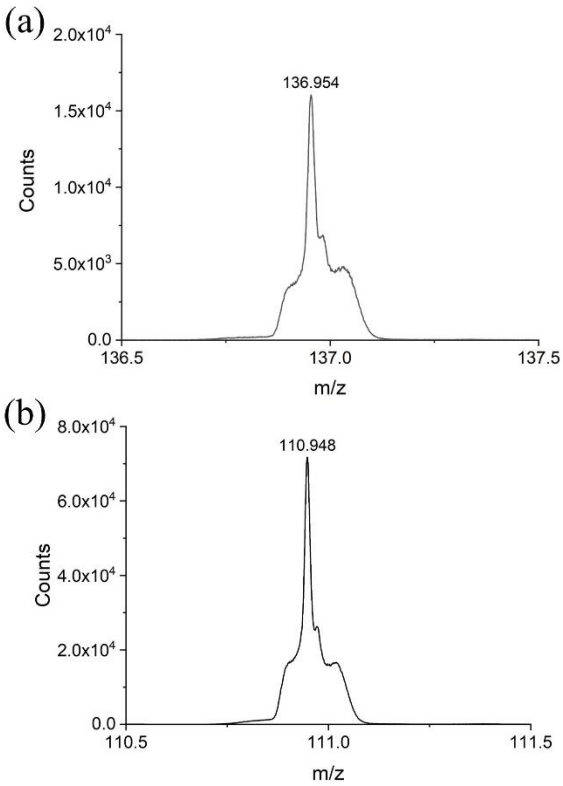

Figure A.2 Mass spectra of (a) the peak at m/z = 137 and (b) the peak at m/z = 111.

doi:10.6342/NTU202303887

Depth profile was also conducted for the bimetallic ZIF thin film prepared with Zn and Co using the same sputtering parameter determined for ZIF-8 in section 4.2.2. which is 10 kV Ar_{2500}. Figure A.3 shows the depth profile of a bimetallic ZIF thin film prepared with precursors where the molar ratio of Zn^{2+} : Co^{2+} is 1 : 1 in (a) and 9 : 1 in (b). Although $[CoC_4N_2H_2]^-$ shows much stronger relative intensities than $[ZnC_4N_2H_2]^-$ does in both figure A.3 (a) and (b), it does not mean the molar ratio of Co^{2+} is significantly higher in the bimetallic ZIF thin films. Ionization yields of different fragments are different so the quantitative analysis might not be intuitive in this manner for SIMS analysis. Nonetheless, by comparing the same peak in the same matrix, the data could be discussed quantitatively. Figure A.3 (a) shows a stronger relative intensity of $[CoC_4N_2H_2]^-$ than figure A.3 (b) does, suggesting that Co^{2+} has a higher molar ratio in figure A.3 (a) which is a reasonable result considering the molar concentration of Co^{2+} in the precursor used in figure A.3 (b) is only a fifth of the concentration in the precursor used in figure A.3 (a).

Moreover, the relative intensities of $[CoC_4N_2H_2]^-$ presents to be lower on the surface and increase through the thickness while $[ZnC_4N_2H_2]^-$ shows an inversed trend in both figure A.3 (a) and (b). It suggests that the molar ratio of Zn^{2+} : Co^{2+} is higher on the surface than in the bottom part of the bimetallic ZIF thin films in both cases. Furthermore, this gradient appears to be greater in figure A.3 (b) where the total amount of Co^{2+} in the precursor is only a fifth of the Co^{2+} appearing in the precursor used in figure A.3 (a). A theory is proposed to explain these two features of the metal ion gradient appearing in the bimetallic thin films: The gradient arose because 2-mIm tends to coordinate to Co^{2+} more than Zn^{2+}. Thus, a Co^{2+} rich layer of bimetallic ZIF was developed at the bottom first and the subsequent growth of ZIF contained less and less Co^{2+} because Co^{2+} in the precursor had been consumed more rapidly than Zn^{2+} throughout the process. The gradient is more

doi:10.6342/NTU202303887

significant in figure A.3 (b) because the Co^{2+} concentration in the precursor changes more significantly when a certain amount of Co^{2+} is consumed in a precursor which contains less Co^{2+}.

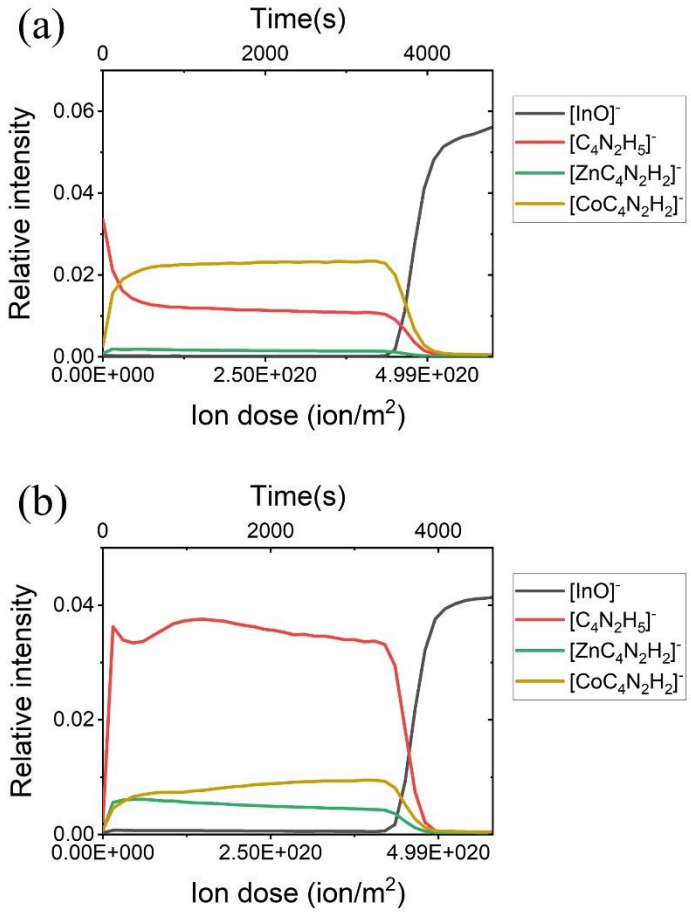

Figure A. 3 Depth profiles of bimetallic thin films prepared with precursors containing Zn^{2+} : Co^{2+} with molar ratios of (a) 1: 1 and (b) 9 : 1.

doi:10.6342/NTU202303887